Customer	**: ESRIN**	**Document Ref :**	**SST_CCI-ATBDV2-UOE-001**
		Issue Date :	**17 May 2013**
		Issue :	**1**

Project : **CCI Phase 1 (SST)**

Title : **SST CCI Algorithm Theoretical Basis Document v1**

Abstract : This is the Algorithm Theoretical Basis Document for the Sea Surface Temperature Climate Change Initiative project. This version covers the principles of algorithms selected within the project to obtain sea surface temperature (SST), in terms of retrieval of skin SST from satellite radiances, physically based estimation of SST depth, and analysis (interpolation) of SST to spatially complete products.

Author : C J Merchant, O Browne and SST CCI project team, The University of Edinburgh

Checked : P Spinks
Space Connexions Ltd

Accepted : Craig Donlon
ESA

Acceptance Date:

Distribution : SST_cci team members

ESA (Craig Donlon)

AMENDMENT RECORD

This document shall be amended by releasing a new edition of the document in its entirety. The Amendment Record Sheet below records the history and issue status of this document.

AMENDMENT RECORD SHEET

ISSUE	DATE	REASON FOR CHANGE
1	17 May 2013	Initial Issue

TABLE OF CONTENTS

This document is to be used with the ESA SST_cci Version 1 (v1) products.

CCI Phase 1 (SST)   *SST_CCI-ATBDV2-UOE-001*
SST CCI Algorithm Theoretical Basis Document v2   *Issue 1*

1. INTRODUCTION

1.1 Purpose and Scope

This Algorithm Theoretical Basis Document (ATBD) describes and justifies the algorithms used for obtaining sea surface temperature (SST) estimates within the ESA SST Climate Change Initiative project's prototype processor.

This version 2 ATBD covers the relevant SST CCI algorithms as implemented in the processing chain for generating products. This includes (1) identification of clear-sky pixels for valid retrieval, (2) the SST retrieval itself, (3) other algorithms for generating the SST estimate at standardised time of day and depth, and (4) analysis into spatio-temporally complete multi-sensor products. Compared to the previous version 1 ATBD, this version differs principally in having included the theoretical basis for step (1). The sections addressing (2) to (4) are updated for clarity. Note that uncertainty information is addressed in these processes, and the approaches to uncertainty are consistent with the principles laid out in the Uncertainty Characterisation Report v2 (RD.306).

1.2 Referenced Documents

The following is a list of documents with a direct bearing on the content of this report. Where referenced in the text, these are identified as RD.n, where 'n' is the number in the list below:

RD.38   Berrisford, P., et al (2009), The ERA-Interim archive, European Centre for Medium Range Weather Forecasts, Reading.

RD.43   Eastwood S., K. R. Larsen, T. Lavergne, E. Nielsen, and R. Tonboe (2010), Global Sea Ice Concentration Reprocessing Product User Manual, Met Norway/Danish Meteorological Institute, EUMETSAT Ocean and Sea Ice SAF.

RD.175   CCI Phase 1 (SST), Product Specification Document

RD.181   Merchant C J, C P Old, O Embury and S N MacCallum (2008), Generalized Bayesian Cloud Screening: Algorithm Theoretical Basis version 2.1, School of GeoSciences, University of Edinburgh. Available from: http://www.geos.ed.ac.uk/gbcs/ATBv2.1c.pdf and via http://www.esa-sst-cci.org

RD.184   Embury, O., C. J. Merchant and G. K. Corlett (2012), A Reprocessing for Climate of Sea Surface Temperature from the Along-Track Scanning Radiometers: Initial validation, accounting for skin and diurnal variability, Rem. Sens. Env., pp62 - 78. DOI:10.1016/j.rse.2011.02.028

RD.185   Embury, O. and C. J. Merchant (2012), A Reprocessing for Climate of Sea Surface Temperature from the Along-Track Scanning Radiometers: A New Retrieval Scheme, Rem. Sens. Env., pp 47 - 61, DOI: 10.1016/j.rse.2010.11.020

RD.186   Embury, O., C. J. Merchant and M. J. Filipiak (2012), A Reprocessing for Climate of Sea Surface Temperature from the Along-Track Scanning Radiometers: Basis in Radiative Transfer, Rem. Sens. Env., pp32 - 46, DOI: 10.1016/j.rse.2010.10.016

RD.213   Donlon, C.J., M. Martin, J. Stark, J. Roberts-Jones, E. Fiedler and W. Wimmer (2012). The Operational Sea Surface Temperature and Sea Ice Analysis (OSTIA) system, Remote Sensing of the Environment, 116, 140-158.

This document is to be used with the ESA SST_cci Version 1 (v1) products.

CCI Phase 1 (SST)   *SST_CCI-ATBDV2-UOE-001*
SST CCI Algorithm Theoretical Basis Document v2   *Issue 1*

RD.221   Merchant C J, P Le Borgne, A Marsouin and H Roquet (2008), Optimal estimation of sea surface temperature from split-window observations, Rem. Sens. Env., 112 (5), 2469-2484. doi:10.1016/j.rse.2007.11.011

RD.222   Gentemann, C. L., P. J. Minnett, and B. Ward (2009), Profiles of ocean surface heating (POSH): A new model of upper ocean diurnal warming, J. Geophys. Res., 114, C07017, doi:10.1029/2008JC004825.

RD.226   MacCallum and Merchant (2012), SST CCI Algorithm Selection Report, http://www.esa-sst-cci.org/

RD.227   Fairall, C., E. Bradley, J. Godfrey, G. Wick, J. Edson, and G. Young (1996), Cool-skin and warm-layer effects on sea surface temperature, J. Geophys. Res., 101(C1), 1295-1308.

RD.231   CLAVR-X installation instructions, https://groups.ssec.wisc.edu/users/wstraka/aix-clavr-x-code/installing-clavr-x-on-your-own-machine

RD.232   SST_CCI Multi-sensor Match-up Dataset Specification, SST_CCI-REP-UoL-001

RD.239   Roberts-Jones, J., Fiedler, E. K. and M. Martin (2012), Daily, global, high-resolution SST and sea-ice reanalysis for 1985-2007 using the OSTIA system, J. Climate, doi:10.1175/JCLI-D-11-00648.1, in press.

RD.253   Merchant, C. J., & Le Borgne, P. (2004). Retrieval of sea surface temperature from space based on modeling of infrared radiative transfer: Capabilities and limitations. *Journal of Atmospheric and Oceanic Technology*, 22(11), 1734−1746.

RD.262   Horrocks L. A., Candy B., Nightingale T. J., Saunders R. W., O'Carroll A., and Harris A. R., Parameterisations of the ocean skin effect and implications for satellite-based measurement of sea surface temperature. J. Geophys. Res., Vol. 108(C3), 3096, doi:10.1029/2002JC001503, 2003

RD.263   Kantha L.H., and Clayson C.A., An improved mixed layer model for geophysical applications. J. Geophys. Res. Vol. 99 (C12), 25235–25266, 1994.

RD.264   Lisa A. Horrocks, Andrew R. Harris, and Roger W. Saunders, Modelling the diurnal thermocline for daytime bulk SST from AATSR, NWP FRTR No. 418, UKMO, 2003.

RD.265   Gentemann, C. L., P. J. Minnett, P. Le Borgne, and C. J. Merchant (2008), Multi-satellite measurements of large diurnal warming events, Geophys. Res. Lett., 35, L22602, doi:10.1029/2008GL035730.

RD.266   Mark Filipiak, Diurnal Adjustment Model Selection, 2010

RD.273   Merchant C J, Algorithm Theoretical Basis Document 0, 2012, SST-CCI-ATBDv0-UOE-004-Issue 1 (Accept-Signed).pdf

RD.274   Killie, M. A., Ø. Godøy, S. Eastwood and T. Lavergne: ATBD for EUMETSAT OSI SAF Regional Ice Edge Product, v1.1, 2011. http://osisaf.met.no/docs/osisaf_ss2_atbd_ice-edge-reg_v1p1.pdf

RD.275   Roberts-Jones, J., Fiedler, E. K. and M. Martin (2011), Met Office Technical Report 561: Description and assessment of the OSTIA reanalysis, Met Office.

RD.276   Daley, R. (1991), Atmospheric data analysis. Cambridge University Press.

RD.278   Hollingsworth, A. and P. Lonnberg (1986). The statistical structure of short-range forecast errors as determined from radiosonde data. Part 1: The wind field. Tellus, 38A, 111-136.

RD.280   Bell, M.J., A. Hines and M.J. Martin (2003). Variational assimilation evolving individual observations and their error estimates. Met Office Ocean Applications technical note no. 32. Available from Met Office, Fitzroy Rd, Exeter, UK.

RD.294   Jonah Roberts-Jones, Emma Fiedler, Matthew Martin, Alison McLaren, Improvements to the Operational Sea Surface Temperature and Sea Ice Analysis (OSTIA) system, UKMO Tech Document SST_CCI_TN_UKMO_002

RD.295   Merchant, C. J., P. LeBorgne, H. Roquet and G. Legendre, Extended optimal estimation techniques for sea surface temperature from the Spinning Enhanced Visible and Infra--Red Imager (SEVIRI), in press Rem. Sens. Env.

RD.296   Merchant, C. J., O. Embury, N. A. Rayner, D. I. Berry, G. Corlett, K. Lean, K. L. Veal, E. C. Kent, D. Llewellyn-Jones, J. J. Remedios, and R. Saunders (2012), A twenty-year independent record of sea surface temperature for climate from Along Track Scanning Radiometers, J. Geophys. Res., 117, C12013, doi:10.1029/2012JC008400.

RD.297   Watts, PD; Allen, MR; Nightingale, TJ, (1996) Wind speed effects on sea surface emission and reflection for the Along Track Scanning Radiometer JOURNAL OF ATMOSPHERIC AND OCEANIC TECHNOLOGY Volume: 13 Issue: 1 Pages: 126-141 DOI: 10.1175/1520-0426(1996)013<0126:WSEOSS>2.0.CO;2

RD.298   Mittaz J and A Harris, A physical method for the calibration of the AVHRR/3 thermal IR channels Part II: in orbit comparison of the AVHRR longwave thermal IR channels on board MetOp-A with IASI, J Atmosph Oceanic Technol, 28, 1072, 10.1175/2011JTECHA1517.1

RD.300   Stamnes, K., SC. Tsay, W. Wiscombe and K. Jayaweera, Numerically stable algorithm for discrete-ordinate-method radiative transfer in multiple scattering and emitting layered media, Appl Opt 27 (1988) (12), pp. 2502–2509.

RD.301   Sea Surface Temperature (SLSTR) Algorithm Theoretical Basis Document, SLSTR-ATBD-L2SST-v2.4, August 2012

RD.302   Chevallier, F., Sampled databases of 60-level atmospheric profiles from the ECMWF analyses, SAF Programme: Research Report No. 4, EUMETSAT/ECMWF, 2001.

RD.303   Tobin, D. & L. L. Strow (1994) A Compilation of First-order Line-mixing Coefficients for CO2 Q-branches, J. Quant. Spectrosc. Radiat. Transfer, 52, 281.

RD.304   Deshler, T., Hervig, M.E., Hofmann, D.J., Rosen, J.M. and Liley, J.B. (2003). Thirty years of in situ stratospheric aerosol size distribution measurements from Laramie, Wyoming (41N), using balloon-borne instruments. Journal of Geophysical Research 108(D5): doi: 10.1029/2002JD002514. issn: 0148-0227

RD.306   SST CCI Uncertainty Characterisation Report v2, SST_CCI-UCR-UOE-002, 2013. Available from www.esa-sst-cci.org

This document is to be used with the ESA SST_cci Version 1 (v1) products.

CCI Phase 1 (SST)   *SST_CCI-ATBDV2-UOE-001*
SST CCI Algorithm Theoretical Basis Document v2   *Issue 1*

RD.307   Rodgers C D, Inverse Methods for Atmospheric Sounding, World Scientific, Singapore, ISBN 981-02-2740-X, 2000.

RD.308   Bulgin C E, Eastwood S, Embury O, Merchant C J, Donlon C. The Sea Surface Temperature Climate Change Initiative: Alternative Image Classification Algorithms for Sea-Ice Affected Oceans. Remote Sensing of Environment. Under review. Submitted Jan 2013.

RD.309   Hocking J, Rayer P, Saunders R, Matricardi M, Geer A and Brunel P. RTTOV v10 Users Guide. NWP SAF, The EUMETSAT Network of Satellite Application Facilities. NWPSAF-MO-UD-023. Version 1.5. Date 12/01/2011

RD.310   Thomas S M, Heidinger, A K, Pavolonis M J, Comparison of NOAA's Operational AVHRR-Derived Cloud Amount to Other Satellite-Derived Cloud Climatologies, Journal of Climate, American Meteorological Society, Volume 17, pages 4805-4822, 2004

RD.311   Heidinger A. K., Evan A. T., Foster, M. J. and Walther, A. A Naïve Bayesian Cloud-Detection Scheme Derived from CALIPSO and Applied within PATMOS-x, Journal of Applied Meteorology and Climatology, Volume 51, Pages 1129-1144, 2012.

RD.312   NOAA Satellite and Information Service, National Environmental Satellite, Data and Information Service (NESDIS), US Department of Commerce, Camp Springs, noaasis.noaa.gov/NOAASIS/ml/avhrr.html, last modified 03/07/2013.

RD.318   Hyvärinen, O., Karlsson, K-G. and Dybbroe, A. (1999), Investigations of NOAA AVHRR/3 1.6 imagery for snow, cloud and sunglint discrimination. Nowcasting SAF Visiting scientist report, SMHI, http://www.nwcsaf.org/HD/files/vsadoc/ottohyvarinen_vsa_report_full.pdf

RD.319   Saunders, P. M., (1967), The temperature at the ocean-air interface, Journal of Atmospheric Science, 24, 269-273.

RD.320   Fillipiak, M., (2008), Refractive indices (500-3500 cm^{-1}) and emissivity (600-3350 cm^{-1}) of pure water and seawater, Dataset, http://hdl.handle.net/10283717

RD.321   Závody, A. M., Mutlow, C. T., Llewellyn-Jones, D. T., (1995), A radiative transfer model for sea surface temperature retrieval for the along-track scanning radiometer, Journal of Geophysical Research: Oceans, 100, C1, 937-952.

1.3   Definitions of Terms

The following terms have been used in this report with the meanings shown.

Term	Definition
(A)ATSR	(Advanced) Along track scanning radiometer
AOD	Aerosol optical depth
ARC	ATSR Reprocessing for Climate
AVHRR	Advanced Very High Resolution Radiometer
ARGO	Global array of observational profiling floats

BT	Brightness Temperature
CCI	Climate Change Initiative
CLAVR-x	Clouds from AVHRR Extended
DJF	December, January, February
ECMWF	European Centre for Medium-range Weather Forecasting
EN3	Quality controlled subsurface temperature and salinity data set [RD.282]
ERA-40	ECMWF Re-analysis covering 40 years
FFM	Fast Forward Model
GAC	Global Area Coverage
GADS	Global Aerosol Data Set
GCOS	Global Climate Observing System
HadISST1	UKMO Hadley Centre Sea Ice and Sea Surface Temperature data set (version 1)
JJA	June, July, August
LSD	Local Standard Deviation
LUTS	Look-Up Tables
MAP	Maximum a posteriori
ML	Maximum Likelihood
NRT	Near Real Time
NSIDC	National Snow and Ice Data Center
NOAA	National Oceanic and Atmospheric Administration
NWP	Numerical Weather Prediction
O-B	Observation minus Background
OE	Optimal Interpolation
OPAC	the Optical Properties of Aerosols and Clouds dataset
OSI-SAF	Ocean and Sea Ice Satellite Application Facility (EUMETSAT)
OSTIA	Operational Sea Surface Temperature and Sea Ice Analysis
PDF	Probability distribution function
QC	Quality Control

This document is to be used with the ESA SST_cci Version 1 (v1) products.

CCI Phase 1 (SST) *SST_CCI-ATBDV2-UOE-001*
SST CCI Algorithm Theoretical Basis Document v2 *Issue 1*

RMSE	Root Mean Square Error
RTM	Radiative Transfer Model
RTTOV	Radiative Transfer for the Television and Infrared Orbiting Satellite Operational Vertical Sounder
SADIST	Synthesis of ATSR Data Into Sea-surface Temperature.
SMMR	Scanning multichannel microwave radiometer
S-O	Simulation minus Observation
SOAR	Second Order Auto-Regressive
SOZ	Solar Zenith Angle
SSM/I	Special Sensor Microwave/Imager
SST-CCI	Sea Surface Temperature Climate Change Initiative
TCWV	Total Column Water Vapour
TOA	Top Of Atmosphere
VisRTM	Visible Radiative Transfer Model

2. IDENTIFICATION OF OBSERVATIONS VALID FOR SEA SURFACE TEMPERATURE ESTIMATION

Cloud screening is a fundamental pre-processing step for sea surface temperature (SST) retrieval. Traditionally, threshold based techniques have been used to detect cloud but these often fail under difficult circumstances -- for example, in the detection of thin cirrus or low-level fog. Two Bayesian cloud detection algorithms are presented here, one for the ATSR instruments which is described in this section, and the CLAVR-x algorithm which is used with the AVHRR instruments, described in section 2.2. Both algorithms calculate the probability that an ocean pixel is clear-sky. For CLAVR-x sets of thresholds are placed on the probability to give a classification of clear, probably clear, probably cloud or cloud for each pixel. The probabilistic approach enables the user to tailor the cloud screening stringency appropriately to their application. For ATSR sea surface temperature (SST) retrievals within the CCI project a single threshold of 0.9 is set on the clear-sky probability to select cases for which SST is considered valid.

2.1 Clear-sky Detection for Along Track Scanning Radiometers

The Along Track Scanning Radiometer (ATSR) instruments make observations at infrared and visible wavelengths at two viewing angles: the nadir view between 0-22° and the forward view between 52-55°. Both views can be exploited to give additional information for cloud detection purposes. ATSR-1 made measurements in spectral bands centred at 1.6, 3.7, 10.8 and 12 μm, whilst ATSR-2 and AATSR instruments had additional visible wavelength channels centred at 0.55, 0.66 and 0.87 μm. The probability of clear sky is calculated by assessing the likelihood that the pixel is clear given the observations, background information, cloudy probability density function (PDF) look-up tables (LUTs) and simulations of clear-sky conditions.

2.1.1 Algorithm Overview - General Principles of Bayesian Classifier

The Bayesian classifier calculates a probability of clear-sky for any given pixel based on the satellite observations, prior information about the atmosphere and surface conditions and the respective errors in these variables. Figure 2.1 shows a high level overview of the classification process. The Bayesian classifier for the SST CCI processing takes European Centre for Medium-range Weather Forecasting (ECMWF) numerical weather prediction (NWP) reanalysis data as input to simulate clear sky brightness temperatures and top of the atmosphere reflectance. The other inputs are ATSR satellite observations and cloudy PDF LUTs. The Bayesian classifier provides the probability of clear-sky as output on a per pixel basis for use in conjunction with the SST data.
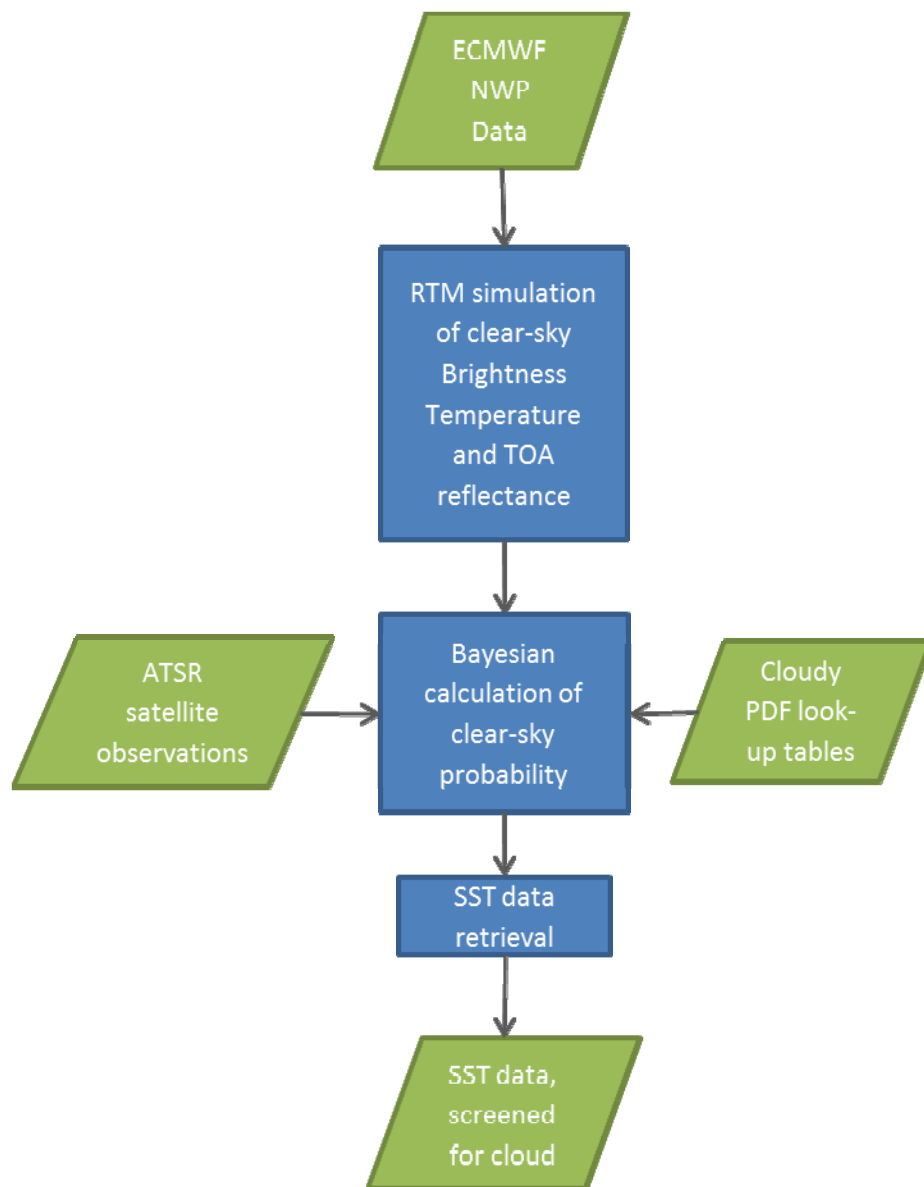
Figure 2.1. Flow chart showing overview of the classification process. Green parallelograms indicate input data, blue squares indicate processing steps.

Figure 2.2 gives a more detailed overview of the steps involved in the Bayesian classification. The inputs, auxiliary data, calculations and outputs are described in the following sections.

Pixel by pixel image processing

Select pixel, allocate and zero pixel structure

Get image pixel coordinates

Check whether correction for Mt. Pinatubo aerosol is required

Is pixel obviously cloud, land, space or limb? — Yes → Flag pixel

Get pixel's latitude, longitude, solar & viewing geometry → Navigate pixel

Load observation error / NEδT

Set day/night flag

Find nearest model indices ← Get coordinates of four neighbouring NWP tie-points

Check if high resolution background SST available

Calculate clear-sky simulated BTs and reflectances → Run RTM

Calculate volcanic aerosol contribution

Interpolate solar correction to IR channels

Test for ice (Flag pixel if ice is detected)

Calculate Saharan Dust Index

Interpolate simulated clear-sky values and H-matrix to pixel location

Empirical BT correction

Get B and R matrices

Calculate obs-model differences $(BT^o - BT^b)$

Calculate LSD of 11pm BT ← $LSD_i = \sqrt{\frac{1}{9} \sum_{9 \text{ pixel box}} \left(y_i^o - \langle y_i^o \rangle \right)^2}$

Look up $P(c)$

$P(y_s^o|x^b,c)P(y_t^o|x,c), P(y_t^o|x^b,c)$ → Get PDF values from LUTs. Cloud spectral and textural probabilities, clear-sky texture

Calculate $P(y_s^o|x^b,c)$ using RTM simulation

Calculate $P(c|y^o,x^b)$

Store results in product structure

Do SST retrieval

Is this the last pixel? — No

Finish

Figure 2.2. Bayesian classification steps for calculating clear-sky probability prior to SST retrieval. Blue rectangles denote processing steps, blue diamonds decision making steps and green parallelograms data storage.

This document is to be used with the ESA SST_cci Version 1 (v1) products.

CCI Phase 1 (SST)   SST_CCI-ATBDV2-UOE-001
SST CCI Algorithm Theoretical Basis Document v2   Issue 1

2.1.2 Inputs to Bayesian Classifier

The Bayesian classifier uses a number of inputs including sensor data, numerical weather prediction data, radiative transfer model output and cloud.

2.1.2.1   Sensor Data - Brightness Temperature, Reflectance

The ATSR observations used in the Bayesian classifier form the observation vector, y^o. The subset of channels used in the observation vector is dependent on time of day.

The channels used in the cloud detection algorithm are present on all ATSR sensors and give consistency over the dataset time series. The cloud detection algorithm is a dual view retrieval using data in the channels specified from both the nadir and forward views. The observation vector, y^o, is defined under day conditions as,

$$y^o = \begin{bmatrix} RE_{1.6} \\ BT_{10.8} \\ BT_{12.0} \\ LSD_{3x3}(BT_{10.8}) \end{bmatrix} \qquad (2.1)$$

and under night conditions as,

$$y^o = \begin{bmatrix} BT_{3.7} \\ BT_{10.8} \\ BT_{12.0} \\ LSD_{3x3}(BT_{10.8}) \end{bmatrix} \qquad (2.2)$$

where:

BT   denotes brightness temperature

LSD   is the local standard deviation over a 3x3 pixel box

RE   denotes reflectance
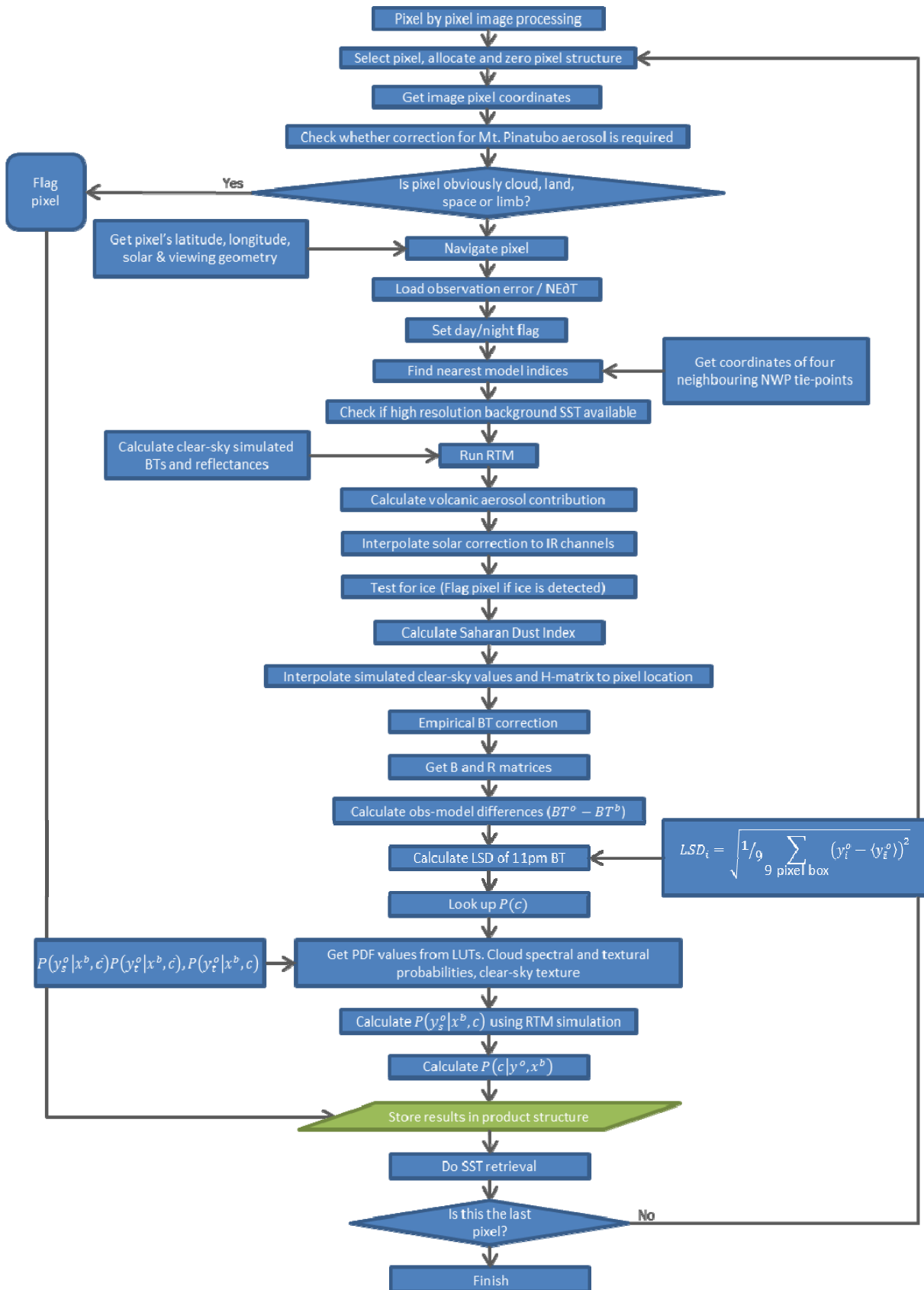
1.6, 3.7, 10.8, 12.0   subscripts define the ATSR channel.

The 10.8 and 12 μm brightness temperatures are used under all conditions and the 1.6 and 3.7 μm channels are alternated on the basis of the solar zenith angle. Daytime conditions are defined by a solar zenith angle less than 87.5 degrees, and nighttime conditions by solar zenith angles above 92.5 degrees. For the twilight period between 87.5-92.5 degrees no retrieval is made. In addition to the spectral information, the local standard deviation in the 10.8 μm brightness temperature is used as a textural measure in the observational data.

$$LSD_i = \sqrt{\frac{1}{9} \sum_{9 \text{ pixel box}} (y_i^o - \langle y_i^o \rangle)^2} \qquad (2.3)$$

where:

y_i^o is the 10.8 μm brightness temperature for a given observation.

$< y_i^o >$ is the mean 10.8 μm brightness temperature across the 3x3 pixel box.

2.1.2.2 Auxiliary Data and Look Up Tables

NWP data from the ECMWF are used in the radiative transfer forward modelling (section 2.1.2.3) to simulate clear sky brightness temperatures and top of the atmosphere (TOA) reflectance. The full background state vector contains all surface and atmospheric variables that can influence the calculated radiance. For the characterisation of the uncertainty in the clear-sky simulation results that is needed for the Bayesian calculation, only the dominant terms need be considered. These terms are shown in the reduced state vector, x^b, shown below. At nighttime (when only infra-red channels are used), the uncertainty with respect to windspeed and aerosol optical depth (AOD) is set to zero. For ATSR-1 during the period of elevated stratospheric aerosol from the eruption of Mt Pinatubo, a fifth element describing the stratospheric aerosol is included in the state vector. For the rest of the record, the reduced state vector is:

$$x^b = \begin{bmatrix} SST^b \\ TCWV^b \\ u_{10}^b \\ AOD^b \end{bmatrix} \tag{2.4}$$

where:

SST   is sea surface temperature

TCWV   is total column water vapour

u_{10} is the 10 m wind vector

AOD   is aerosol optical depth.

Reflectance/BT distributions given cloud probabilities are stored as empirical PDFs as these are difficult to model and cannot be assumed to be Gaussian. The PDFs are generated using the entire ATSR time series of observations initially bootstrapped using the operational SADIST cloud mask to identify cloudy pixels. Subsequently these were iterated once using the Bayesian cloud detection scheme as part of the ATSR Reprocessing for Climate (ARC) project. This iteration enabled the inclusion of dual view data and refinement of the PDF dimensions.

The probability density function (PDF) given the background state for each class of observation (clear or cloud) is expressed as a 'spectral' and 'textural' component (outlined in section 2.1.3), which are assumed to be independent. For both cloud and clear classes, the textural component is an empirical PDF (captured as a look up table, LUT) generated as explained above. This is also the case for the spectral component for the cloud class. The clear-sky spectral PDF is calculated using the forward models based on the uncertainty of the elements in x^b. The dimensions, range and binsize of the respective PDFs (LUTs) are shown in the tables below. These are chosen so that the resulting PDF is adequately smooth, for which we required that the numbers of observations used to build the LUTs was at least three orders of magnitude larger than the number of LUT bins. The satellite zenith angle dimension is used to separate the nadir and forward view PDFs. Observations that fall outside the PDF dimensions are fixed to the edge of the PDFs for the Bayesian cloud detection.

For the spectral probability under nighttime conditions a three channel brightness temperature PDF is used. This includes a day/night flag as it is also used in conjunction with a visible channel PDF during the day.

Table 2.1. Cloud Nighttime Spectral PDF

Dimension	Unit	Upper limit	Lower limit	Bin size	Number of bins
11µm BT – NWP SST	*K*	*10.00*	*-20.00*	*2.0*	*15*
11-12µm BT difference	*K*	*9.0*	*-1.00*	*0.2*	*50*
3.7-11µm BT difference	*K*	*10.00*	*-6.00*	*0.2*	*80*
NWP SST	*K*	*310.00*	*260.00*	*2.5*	*20*
Satellite zenith angle	*°*	*60.00*	*0.0*	*30.0*	*2*
Day/Night	*°*	*180.00*	*0.0*	*90.0*	*2*

Figure 2.3 shows some slices of the spectral PDF described in Table 2.1. The PDFs are three-dimensional in brightness temperature space (11 µm BT–NWP SST, 11–12 µm BT and 3.7–11 µm BT). For visualization purposes the PDFs have been collapsed along one of these dimensions and presented for nadir only data for two different NWP SST values. The 11–12 µm BT is plotted as a function of 11 µm BT–NWP SST in the top panel, and as a function of the 11-3.7 µm BT in the bottom panel. The PDF shape and orientation shifts significantly between the two NWP SSTs in the slices presented indicating the importance of constraining the PDF as a function of all the constituent dimensions.
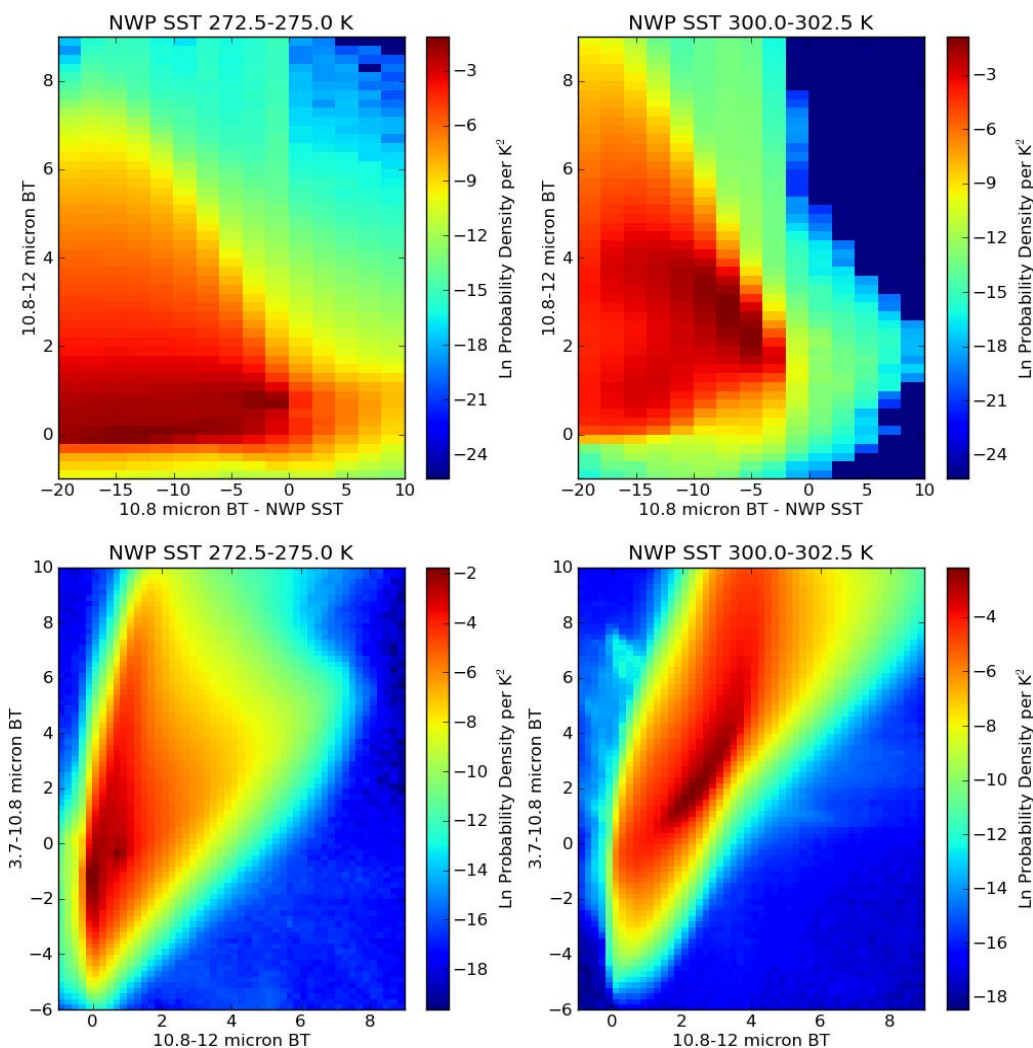

Figure 2.3. Example thermal spectral PDFs for two NWP SST values. The top panel shows the 10.8 micron BT minus the NWP SST against the 10.8 minus 12 micron BT. The lower panel shows the 3.7 minus 10.8 micron BT against the 10.8 minus 12 micron BT. PDF shapes show significant variation as a function of SST.

This document is to be used with the ESA SST_cci Version 1 (v1) products.

CCI Phase 1 (SST)   SST_CCI-ATBDV2-UOE-001
SST CCI Algorithm Theoretical Basis Document v2   Issue 1

During the day, the observation vector includes both infrared and visible channel data. The PDFs for the infrared and visible components are assumed to be independent which is justified by the different physical processes determining radiance in the reflectance compared to thermal bands. A reduced thermal spectral PDF based on the 10.8 and 12 μm channels only is used in conjunction with a visible PDF based on the 1.6 μm channel.

Table 2.2. Daytime two-channel thermal cloudy spectral PDF

Dimension	Unit	Upper limit	Lower limit	Bin size	Number of bins
11μm BT – NWP SST	K	10.00	-20.00	1.0	30
11-12μm BT difference	K	9.0	-1.00	0.2	50
NWP SST	K	310.00	260.00	1.0	20
Satellite zenith angle	°	60.00	0.0	30.0	2
Day/Night	°	180.00	0.0	90.0	2

Table 2.3. Daytime reflectance cloudy spectral PDF

Dimension	Unit	Upper limit	Lower limit	Bin size	Number of bins
1.6μm reflectance		1.00	0.0	0.01	100
Solar zenith angle	°	95.00	0.0	2.5	38
Satellite zenith angle	°	60.00	0.0	30.0	2

Figure 2.4 shows a graphical representation of the dual view PDF for the 1.6 μm channel. The two panels show the dual view data for different solar zenith angles. As the solar zenith angle increases the PDF becomes more spread out with a tendency towards higher reflectance in the nadir view. At lower solar zenith angles the 1.6 μm nadir versus forward view PDF is closer to the 1:1 line. The reflectance peak for relatively dark clouds may be the result of partially filled pixels flagged as cloud where some of the darker underlying ocean surface is also visible.
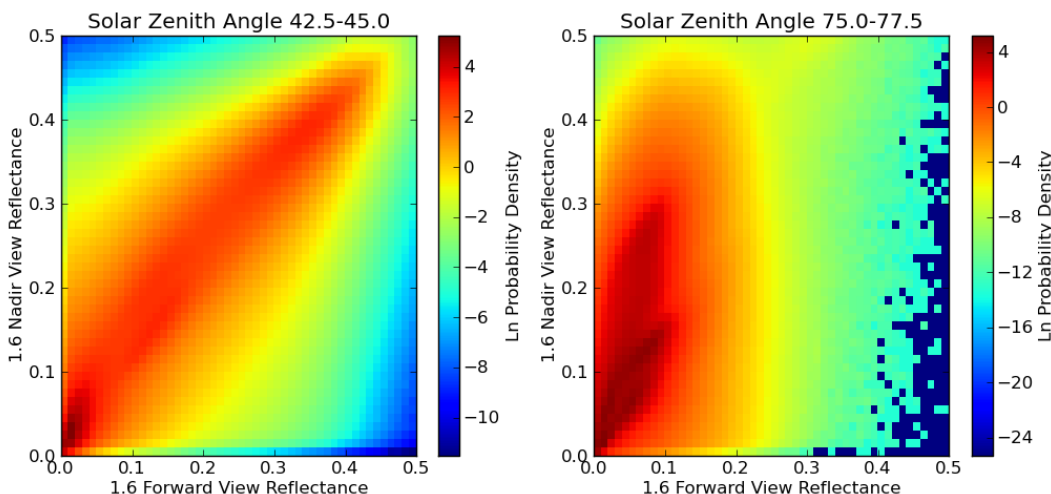
Figure 2.4. Visible spectral dual view PDFs showing the 1.6 micron nadir versus forward view reflectance given cloudy conditions.

A 10.8 μm textural PDF is a useful tool for cloud detection and is used alongside the spectral PDF for all classifications [Table 2.4]. Figure 2.5 shows the textural PDF under day and nighttime conditions for the nadir view data. The cloudy PDF is much broader than the clear-sky PDF as cloud surfaces are more heterogeneous than the underlying sea surface over a 3x3 pixel [3x3 km] surface area.

Table 2.4. Textural PDF construction. Separate PDFs are generated for clear-sky and cloudy conditions.

Dimension	Unit	Upper limit	Lower limit	Bin size	Number of bins
11 µm texture	K	2.0	0.0	0.005	400
Satellite zenith angle	°	60.0	0.0	30.0	2
Day/Night	°	180.0	0.0	90.0	2
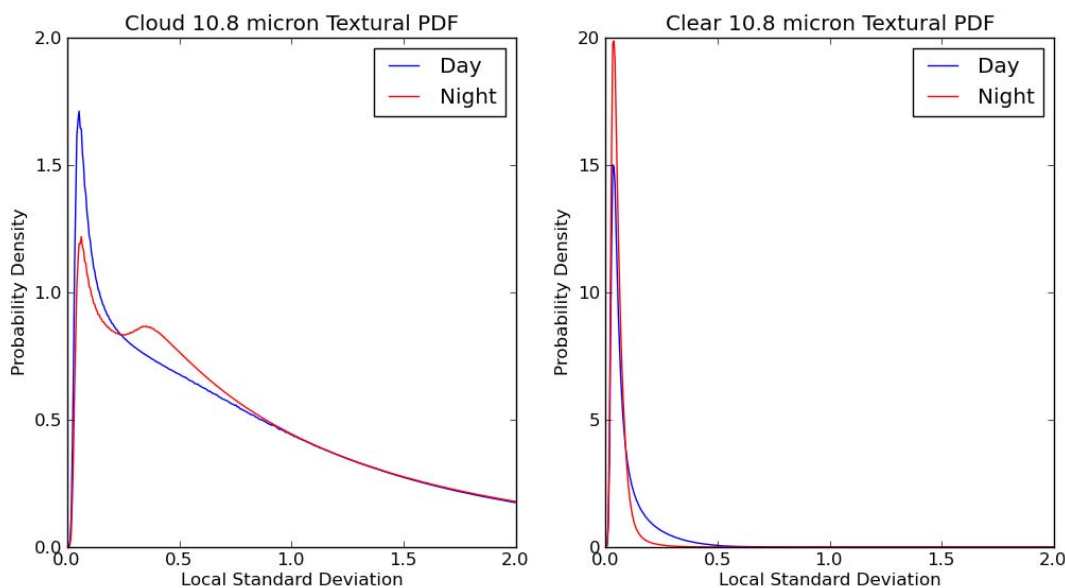
Figure 2.5. 11 micron textural PDFs dependent upon time of day for cloud and clear-sky observations (nadir view only)

A LUT is also developed for the prior clear-sky probability, which is a function of latitude and longitude. The prior clear-sky probability was calculated by counting the number of clear relative to total number of AATSR pixels for each location, i.e., using the following equation:

$$P(c) = \frac{\sum(c^o)}{\sum(c^o) + \sum(\bar{c}^o)} \tag{2.5}$$

where:

c denotes clear sky

$\bar{c}$ denotes cloud

$P(c)$ was calculated at 1x1 degree resolution and the global distribution is shown in Figure 2.6. The maximum prior probability of clear sky is 0.5, seen in the mid-Pacific and south-east Atlantic and Indian Oceans. The Pacific and Atlantic oceans off the west-coasts of South America and Africa are typically cloudier.
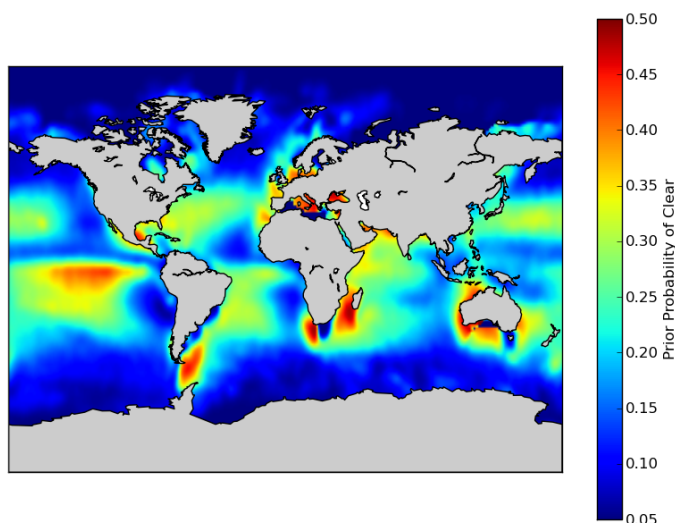
Figure 2.6. Global map of the prior probability of clear-sky generated from ARC processing of ATSR data.

2.1.2.3 Forward model

Two forward models are used in the cloud detection scheme. RTTOV 10.2 is used for channels at infrared wavelengths (3.7, 11 and 12 μm) and VisRTM for solar channels (1.6 μm) and solar corrections to the infrared channels. Both calculate the tangent linear with respect to the elements of the reduced state vector (x_b) for the calculated brightness temperature or reflectance.

RTTOV 10.2 is the most recent edition of a fast forward model (FFM) developed at the EUMETSAT NWP Satellite Application Facility to calculate atmospheric radiative transfer at infrared wavelengths [RD.309]. NWP atmospheric profile and surface conditions are used as input and the model is run at the ATSR geolocation tie-points at a resolution of 25 x 32 km. The outputs are then interpolated to the pixel location. VisRTM is a single-scattering model used to calculate TOA reflectance and to make solar corrections to the infrared channels [RD.181]. It is computationally faster than RTTOV 10.2 so is run at every pixel.

## 2.1.2.4 Auxiliary Data for Pinatubo Aerosol Period

The eruption of Mount Pinatubo (and Mount Hudson) in 1991 injected a significant amount of sulphate aerosol into the stratosphere that then decayed over a period of several years. The injected sulphate aerosol falls into two modes – a fine mode and a coarse mode fraction. The latter has a greater impact at infrared wavelengths and a correction is made to the simulated brightness temperatures to account for this [RD.186].

The correction works by first determining the aerosol 'mode', which is a standardised brightness temperature impact (dBT) averaged over many aerosol scattering simulations [RD.186, RD.304] for an arbitrary volcanic aerosol optical depth. dBT is dependent on the channel and the satellite zenith angle. Next, the scaling of the dBTs (reflecting the variable amount of volcanic aerosol optical depth) is estimated as a function of latitude and for 3 day intervals during the 'Pinatubo' period. This is done by inference from the differential impact of volcanic aerosol on SST estimates in nadir-only mode (which are sensitive to aerosol) and in dual-view mode (which are designed to be insensitive to aerosol). Using the standardised dBT, the expected nadir minus dual view SST difference is calculated as a function of latitude. Then the observed nadir minus dual difference is also calculated as a function of latitude using three-day averages. The observed difference is divided by the expected difference to give an aerosol index that appropriately reflects the impact of the aerosol on infra-red window channels. Adding the multiple of

This document is to be used with the ESA SST_cci Version 1 (v1) products.

CCI Phase 1 (SST)   SST_CCI-ATBDV2-UOE-001
SST CCI Algorithm Theoretical Basis Document v2   Issue 1

the aerosol mode and the aerosol index then modifies the modelled clear-sky brightness temperatures.

$$BT_{channel} = BT_{channel} + (\ aerosol\_mode_{channel} \times aerosol\_index_{channel})$$

(2.6)

where:

BT   is brightness temperature

aerosol_mode is the average brightness temperature impact from a standard amount of stratospheric aerosol (dBT, calculated as function of channel and satellite zenith angle)

aerosol_index observed nadir minus dual view SST, divided by expected nadir minus dual view SST for the standard amount of aerosol.

This brightness temperature adjustment is only made for ATSR-1 data. Having applied this adjustment, the cloud detection procedure is run as for non-aerosol periods.

2.1.3 Mathematical Description of Bayesian Classifier

In discussing Bayes' theorem, notation for conditional probability is used. Thus $P(A|B,C)$ is the probability density for condition or observation A given the assumption that conditions/observations B and C are the case. In this notation, cloud detection is the calculation of $P(c|\boldsymbol{y}^o, \boldsymbol{x}^b)$ -- i.e., the probability of the clear-sky condition, given the observations $\boldsymbol{y}^o$ and the prior information we have brought to the problem, $\boldsymbol{x}^b$. The Bayesian classifier calculates the likelihood that a pixel is a clear-sky ($P(c|\boldsymbol{y}^o, \boldsymbol{x}^b)$) based on the satellite observations and prior information. Formally Bayes theorem applied to the problem of cloud detection can be expressed as:

$$P(c|\boldsymbol{y}^o, \boldsymbol{x}^b) = \frac{P(\boldsymbol{y}^o|\boldsymbol{x}^b, c)P(\boldsymbol{x}^b|c)P(c)}{P(\boldsymbol{y}^o|\boldsymbol{x}^b)P(\boldsymbol{x}^b)}$$

(2.7)

where:

c denotes clear-sky

$\boldsymbol{y}^o$ is the observation vector

$\boldsymbol{x}^b$ is the state vector.

2.1.3.1 Physical Principles and Equations

The assumption can be made that the background state is independent of the clear-sky probability at the ATSR pixel scale (1x1 km). Assuming $P(\boldsymbol{x}^b|c) = P(\boldsymbol{x}^b)$, then equation 2.7 can be simplified to give:

$$P(c|\boldsymbol{y}^o, \boldsymbol{x}^b) = \frac{P(\boldsymbol{y}^o|\boldsymbol{x}^b, c)P(c)}{P(\boldsymbol{y}^o|\boldsymbol{x}^b)}$$

(2.8)

The probability of the observations given the background state, $P(\boldsymbol{y}^o|\boldsymbol{x}^b)$, can be expressed as the sum of the probabilities for each possible state (cloud $\bar{c}$ and clear c).

$$P(\boldsymbol{y}^o|\boldsymbol{x}^b) = P(c)P(\boldsymbol{y}^o|\boldsymbol{x}^b, c) + P(\bar{c})P(\boldsymbol{y}^o|\boldsymbol{x}^b, \bar{c})$$

(2.9)

This can be rearranged to give the form of the equation used in the clear-sky probability calculation.

$$P(c|\boldsymbol{y}^o, \boldsymbol{x}^b) = \left[1 + \frac{P(\bar{c})P(\boldsymbol{y}^o|\boldsymbol{x}^b, \bar{c})}{P(c)P(\boldsymbol{y}^o|\boldsymbol{x}^b, c)}\right]^{-1} \tag{2.10}$$

$P(\bar{c})$ is the prior probability of cloud and is equal to one minus the prior probability of clear-sky.

$$P(\bar{c}) = 1 - P(c) \tag{2.11}$$

2.1.3.2   Calculations

The probability of the observations given the background state for either class (cloud or clear) is split into a spectral and textural component denoted by subscripts 's' and 't'. These are assumed to be independent.

$$P(\boldsymbol{y}^o|\boldsymbol{x}^b, c) = P(\boldsymbol{y}_s^o|\boldsymbol{x}^b, c)P(\boldsymbol{y}_t^o|\boldsymbol{x}^b, c) \tag{2.12}$$

For the cloud class the spectral component of this equation is calculated from a probability density function (PDF) look up table as described in section 2.1.2.2. For clear-sky this is calculated using the radiative transfer model where the distribution is assumed to be Gaussian. The spectral probability for clear-sky is defined as follows:

$$P(\boldsymbol{y}_s^o|\boldsymbol{x}^b, c) = \frac{e^{\left(-\frac{1}{2}\Delta y^t(H^t BH + R)^{-1}\Delta y\right)}}{2\pi|H^t BH + R|^{0.5}} \tag{2.13}$$

$H^t BH$ is the error covariance in the background state vector propagated through the fast forward model. The H matrix contains the tangent linear of the forward model.

$$H = \frac{\partial y_s^b}{\partial x^b} \tag{2.14}$$

This is expressed as the sensitivity of the forward model to changes in the reduced state vector (x^b). For example, for the selection of channels used in the spectral calculation at nighttime, the H matrix is defined as follows.

$$H = \begin{bmatrix} \dfrac{\partial BT_{3.7}}{\partial SST^b} & \dfrac{\partial BT_{10.8}}{\partial SST^b} & \dfrac{\partial BT_{12.0}}{\partial SST^b} \\[2mm] \dfrac{\partial BT_{3.7}}{\partial TCWV^b} & \dfrac{\partial BT_{10.8}}{\partial TCWV^b} & \dfrac{\partial BT_{12.0}}{\partial TCWV^b} \\[2mm] \dfrac{\partial BT_{3.7}}{\partial \boldsymbol{u}_{10}^b} & \dfrac{\partial BT_{10.8}}{\partial \boldsymbol{u}_{10}^b} & \dfrac{\partial BT_{12.0}}{\partial \boldsymbol{u}_{10}^b} \\[2mm] \dfrac{\partial BT_{3.7}}{\partial AOD^b} & \dfrac{\partial BT_{10.8}}{\partial AOD^b} & \dfrac{\partial BT_{12.0}}{\partial AOD^b} \end{bmatrix} \tag{2.15}$$

Under nighttime conditions the tangent linears with respect to wind speed and aerosol optical depth are set to zero. B is the background error covariance matrix and contains the errors of the components in the reduced state vector. This can be specified as follows:

$$B = \begin{bmatrix} (\varepsilon_{SST}^b)^2 & 0.0 & 0.0 & 0.0 \\ 0.0 & (\varepsilon_{TCWV}^b)^2 & 0.0 & 0.0 \\ 0.0 & 0.0 & \left(\varepsilon_{u_{10}}^b\right)^2 & 0.0 \\ 0.0 & 0.0 & 0.0 & (\varepsilon_{AOD}^b)^2 \end{bmatrix} \tag{2.16}$$

Matrix $\boldsymbol{R}$ is the error covariance matrix of the differences between the model and observed values. The model component, $\boldsymbol{R}^m$, can be derived as:

$$\boldsymbol{R}^m = \begin{bmatrix} (\varepsilon_i^m)^2 & r^2(\varepsilon_i^m)(\varepsilon_j^m) \\ r^2(\varepsilon_i^m)(\varepsilon_j^m) & \left(\varepsilon_j^m\right)^2 \end{bmatrix} \tag{2.17}$$

where the diagonal terms describe the FFM error in the given channel and the off-diagonal terms the co-variance in that error. The observational component of this error is defined as the 'noise' in the observations or noise-equivalent delta brightness temperature (NEdT) in the thermal channels. This is assumed to be diagonal:

$$\boldsymbol{R}^o = \begin{bmatrix} (\varepsilon_i^o)^2 & 0.0 \\ 0.0 & \left(\varepsilon_j^o\right)^2 \end{bmatrix} \tag{2.18}$$

$\boldsymbol{R}^o$ and $\boldsymbol{R}^m$ are combined to define the **R** matrix. We assume that r^2 is equal to zero for the model error and therefore the off-diagonal terms of this matrix remain as zero.

$$\boldsymbol{R} = \boldsymbol{R}^m + \boldsymbol{R}^o = \begin{bmatrix} (\varepsilon_i^m)^2 + (\varepsilon_i^o)^2 & r^2(\varepsilon_i^m)(\varepsilon_j^m) \\ r^2(\varepsilon_i^m)(\varepsilon_j^m) & \left(\varepsilon_j^o\right)^2 + \left(\varepsilon_j^m\right)^2 \end{bmatrix} \tag{2.19}$$

For both clear and cloud classes the textural component is the local standard deviation of the 10.8 μm channel in the nine surrounding pixels (equation 2.3). All textural probabilities are stored in PDF LUTs.

2.1.3.3   Algorithm Output

The cloud detection algorithm outputs a probability of clear-sky for each pixel processed. SST retrieval is also done for each pixel so that the user on an application specific basis can determine the stringency of the cloud screening. Within the CCI project only pixels with a clear-sky probability greater than 0.9 are used for SST retrieval.

2.1.4 Assumptions and Limitations

This section describes the current performance of the Bayesian cloud detection, considers assumptions and limitations and future enhancements to the algorithm

2.1.4.1   Current Performance

Over the ocean the Bayesian cloud detection performs better than the threshold based operational cloud mask. This is evidenced in the reduction of the standard deviation of the AATSR satellite minus in-situ SST differences between July 2002 and December 2007 when using the Bayesian cloud detection compared to SADIST [RD.184].

There are known regions and particular cloud types where cloud detection is more difficult. The easiest cloud to detect is that which is 'bright' and 'white' providing a distinct signal at both visible and infrared wavelengths that differs from that of the dark underlying ocean surface. Low-level fog is often dark making it difficult to distinguish at visible wavelengths and has a temperature close to the SST. Thin or semi-transparent ice cirrus often has a sub-pixel extent and is also difficult to detect.

At high latitudes cloud detection is also more difficult in regions of sea-ice. Newly formed sea-ice is close in temperature to the neighbouring open-water pixel and the surface is dark. Over the sea-ice surface, melt ponds can also make it difficult to identify whether

This document is to be used with the ESA SST_cci Version 1 (v1) products.

CCI Phase 1 (SST)   *SST_CCI-ATBDV2-UOE-001*
SST CCI Algorithm Theoretical Basis Document v2   *Issue 1*

the surface is water or ice. Sea-ice pixels mistakenly classified as open water, will bias the SST retrieval.

2.1.4.2   Assumptions Made

Within the Bayesian cloud detection independence is assumed between the infrared and visible channel probabilities of clear and cloud observations. In the context of the reduced state vector, TOA reflectance is assumed independent of prior SST. This assumption is made to simplify the forward modelling. Spectral and textural probabilities are also assumed to be independent allowing the extraction of two pieces of information from the observations.

In the $\boldsymbol{R}^m$ matrix an r^2 value of zero is assumed in the off-diagonal term giving no covariance between channels. In reality there will be a strong error covariance between the 10.8 and 12 μm channels (and the 3.7 μm channel at night). Further research is needed to correctly determine the off-diagonal terms of this matrix.

In the cloud detection scheme the assumption is made that the pixel will either be 'clear over ocean' or 'cloud'. Sea-ice pixels are unlikely to be well represented in the cloudy PDFs and therefore are more likely to be misclassified.

2.1.5 Future Enhancements

Using a three-way image classifier could enhance cloud detection at high latitudes. Each pixel would be classified as 'clear-over-water', 'clear-over-ice' or cloud. The sea-ice surface could be modelled using the FFMs to help distinguish between open-water and ice pixels. Work was undertaken as part of SST CCI in parallel with the high latitude extension developed for the AVHRR instruments [RD.308]. This showed particular benefits for AATSR where visible channel information were always available during the day, but more development is required for a consistent application across all ATSR instruments so as not to introduce a bias in the retrieved SSTs.

2.2   Clear-sky Detection for Advanced Very High Resolution Radiometers – All Latitudes

The clear-sky detection for the Advanced Very High Resolution Radiometer (AVHRR) Global Area Coverage (GAC) products uses the operational extended Clouds from AVHRR (CLAVR-x) cloud detection algorithm [RD.310, RD.311]. A general overview of the cloud detection algorithm is provided in this document and for further information the reader is referred to section 2.2.1. This cloud detection algorithm is applied globally to AVHRR data. An additional classification is applied to high latitude regions described in section 2.3.

2.2.1 Algorithm Overview – CLAVR-x

The CLAVR-x algorithm is a Bayesian classification based on the product of six classifiers. It has been described as a "naive" Bayesian implementation, which refers to various simplifying assumptions that are made such as statistical independence for each classifying element of the Bayesian calculation. (In contrast, the ATSR method described in §2.1 does a multi-element calculation for all the thermal channels, for example). It calculates a probability of cloud, (PoCloud), which is then, sub-divided using thresholds into the four categories provided in the cloud mask.

PoCloud < 0.1 = clear

PoCloud < 0.5 = probably clear

This document is to be used with the ESA SST_cci Version 1 (v1) products.

CCI Phase 1 (SST)
SST CCI Algorithm Theoretical Basis Document v2

SST_CCI-ATBDV2-UOE-001
Issue 1

PoCloud > 0.5 = probably cloudy

PoCloud > 0.9 = cloudy

Figure 2.7 describes how the CLAVR-X cloud masking fits into the SST retrieval process for AVHRR instruments.
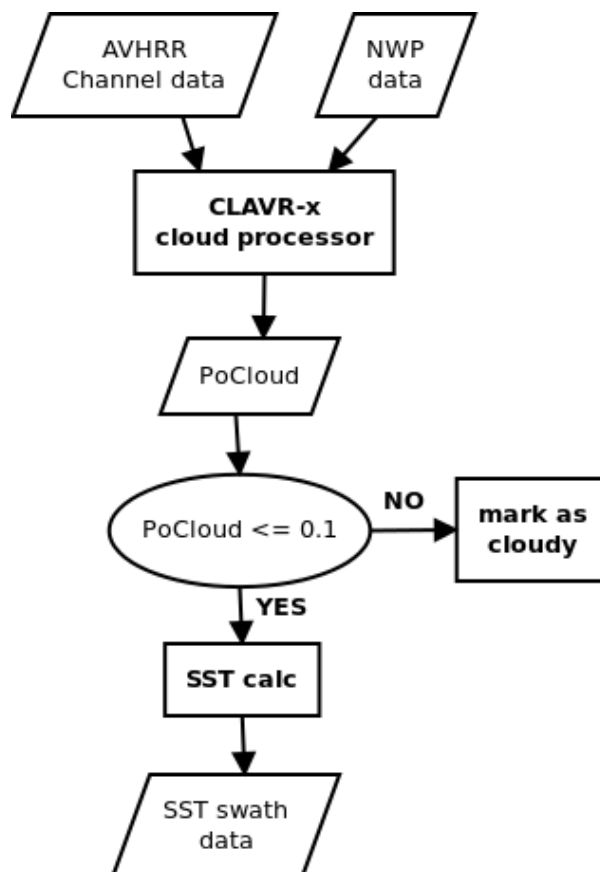
Figure 2.7. Flow chart for CLAVR-x cloud masking process.

2.2.2 Outline of Processing in CLAVR-x

The probability of clear-sky is defined using the following equation:

$$P(c|F) = \frac{P(c) \prod_{i=1}^{N} P(F_i|c)}{P(F)} \qquad (2.20)$$

where:

$P(c|F)$ is the probability of clear-sky

$P(c)$ is the prior probability of clear

F_i refers to each of the six classifiers

For each classifier the function $P(F)$ in the denominator is defined as:

$$P(F) = P(c) \prod_{i=1}^{N} P(F_i|c) + P(\bar{c}) \prod_{i=1}^{N} P(F_i|\bar{c}) \qquad (2.21)$$

This document is to be used with the ESA SST_cci Version 1 (v1) products.

CCI Phase 1 (SST)   *SST_CCI-ATBDV2-UOE-001*
SST CCI Algorithm Theoretical Basis Document v2   *Issue 1*

where:

c denotes clear sky

$\bar{c}$ denotes cloud

The six cloud mask classifiers used in the naïve Bayesian approach to calculate the probability of clear-sky and are individually described in Table 2.5.

Table 2.5. CLAVR-x cloud mask classifiers used in the naïve Bayesian calculation.

Cloud Mask Classifier	Description
Emissivity referenced to the tropopause (ETROP)	This classifier is based on the 11 μm channel emissivity calculated assuming that the cloud was located at the tropopause. This is based on the principle that clouds will be colder at 11 μm than clear-sky and the calculated emissivity assuming a blackbody at the cloud temperature will be lower than the equivalent blackbody emissivity assuming clear-sky.
Relative thermal contrast ($T_{max} - T$)	This is based on the difference in the 11 μm brightness temperature between the given pixel and the warmest pixel in the surrounding 5x5 pixel block. This classifier is designed to detect cloud edges and small-scale cloud features.
Four-minus-five (FMFT)	This is based on the 11-12 μm brightness temperature difference, which increases where semi-transparent cloud is present. This is compared to the estimated clear-sky equivalent for the given 11 μm brightness temperature.
Daytime 4-μm pseudoemissivity (day 4-μm)	This test is based on the calculation of a pseudoemissivity for the 3.75 μm channel in comparison with the emissivity calculated from the 11 μm observation. Where cloud is present the calculated pseudoemissivity value increases significantly. During the day the 4 μm pseudoemissivity is scaled according to solar zenith angle. This test is only used during the day.
Nighttime 4-μm pseudoemissivity (night 4-μm)	A similar 4 μm test is used at night without the solar zenith angle scaling. Opaque clouds will give pseudoemissivity values significantly below unity, whilst cold or semi-transparent clouds will give very large values. This test is only used at night.
Reflectance at 0.63 μm (ref 0.63 μm)	This classifier is based on the difference between the observed 0.6 μm reflectance and the expected clear-sky reflectance. It is based on the assumption that clouds are often brighter than the underlying ocean surface. This is only used during the day and not over regions of sunglint.

2.2.3 Inputs to CLAVR-x

The CLAVR-x cloud detection algorithm uses both satellite observations and auxiliary data as inputs described in the sections below.

2.2.3.1   Sensor Data - Brightness Temperature, Reflectance

The AVHRR instruments make observations at visible and infrared wavelengths and a subset of the available channels are used in the cloud detection algorithm depending on

This document is to be used with the ESA SST_cci Version 1 (v1) products.

CCI Phase 1 (SST)   SST_CCI-ATBDV2-UOE-001
SST CCI Algorithm Theoretical Basis Document v2   Issue 1

time of day. The wavelength bands and channel numbers for the AVHRR channels are provided below [RD.312].

Table 2.6. AVHRR Channel Wave Bands

Channel number	Wave Band (μm)
1	0.58 – 0.68
2	0.725 – 1.0
3A	1.58 – 1.64
3B	3.55 – 3.93
4	10.3 – 11.3
5	11.5 – 12.5

2.2.3.2   Auxiliary Data and Look-Up Tables

Auxiliary data is used in the CLAVR-x algorithm to determine which tests should be applied to a given scene. Only the auxiliary data relevant to cloud detection over ocean is described here. A full list of the auxiliary data used in the algorithm can be found in RD.311.

CLAVR-x uses a map of surface type to identify oceanic pixels. These can be classified either as deep-ocean or shallow-water and the surface map is constructed from the MODIS land cover data. Simulations of clear-sky conditions are made for the emissivity and reflectance comparison tests, which make use of external surface reflectance maps. Further details on these simulations are provided in RD.311.

2.2.4 Further Information on CLAVR-x

Further information with regard to the training dataset used to construct the six Bayesian classifiers can be found in RD.311. The reader is referred to this document for a more in depth description of each classifier and assessment of the algorithm performance.

2.3   Clear-sky Detection for Advanced Very High Resolution Radiometers – High Latitudes Extension

This subsection gives details of the SST-CCI cloud-clearing algorithm extension at high latitudes for AVHRR instruments. The cloud clearing step prior to SST calculation is based on the CLAVR-X method (section 2.2), which is a naive Bayesian cloud probability calculation. After the cloud clearing step an additional Bayesian ice and cloud masking step is applied under conditions where sea ice might be expected. For both these steps the user can apply an application specific threshold on the cloud and ice screening stringency.

At high latitudes it can be difficult to distinguish between open water that often contains strong thermal gradients and sea ice, especially where the surface temperature is close to the point of phase change between open water and ice. The additional clear-over-ice class improves the skill of the algorithm to identify open ocean cases required for SST retrieval purposes. It also enables identification of sea-ice surfaces for potential ice surface temperature retrieval.

2.3.1 Algorithm Description

2.3.1.1 Algorithm Overview

This chapter describes the AVHRR cloud and ice mask algorithm to be applied in the SST-CCI SST retrieval following the SST calculation. It describes an algorithm that classifies each AVHRR GAC swath pixel as clear-open-water, ice covered or cloudy. These three classes are represented using PDFs. These PDFs are used in a naive Bayesian approach to calculate the probability of these three classes, for each pixel.

2.3.1.2 Processing Outline

The cloud and ice masking for the AVHRR retrieval is split in two stages. CLAVR-x described in section 2.2, and the high-latitude extension described here. The high latitude step can be run either directly after the CLAVR-x step, or at a later stage, and is run on all pixels which have been classified as clear-open-water by the CLAVR-x step. A flow chart for the high latitude extensions is shown below (Figure 2.8).

This document is to be used with the ESA SST_cci Version 1 (v1) products.

CCI Phase 1 (SST)　　　　　　　　　　　　　　　　　*SST_CCI-ATBDV2-UOE-001*
SST CCI Algorithm Theoretical Basis Document v2　　　　　　　　　　　　*Issue 1*
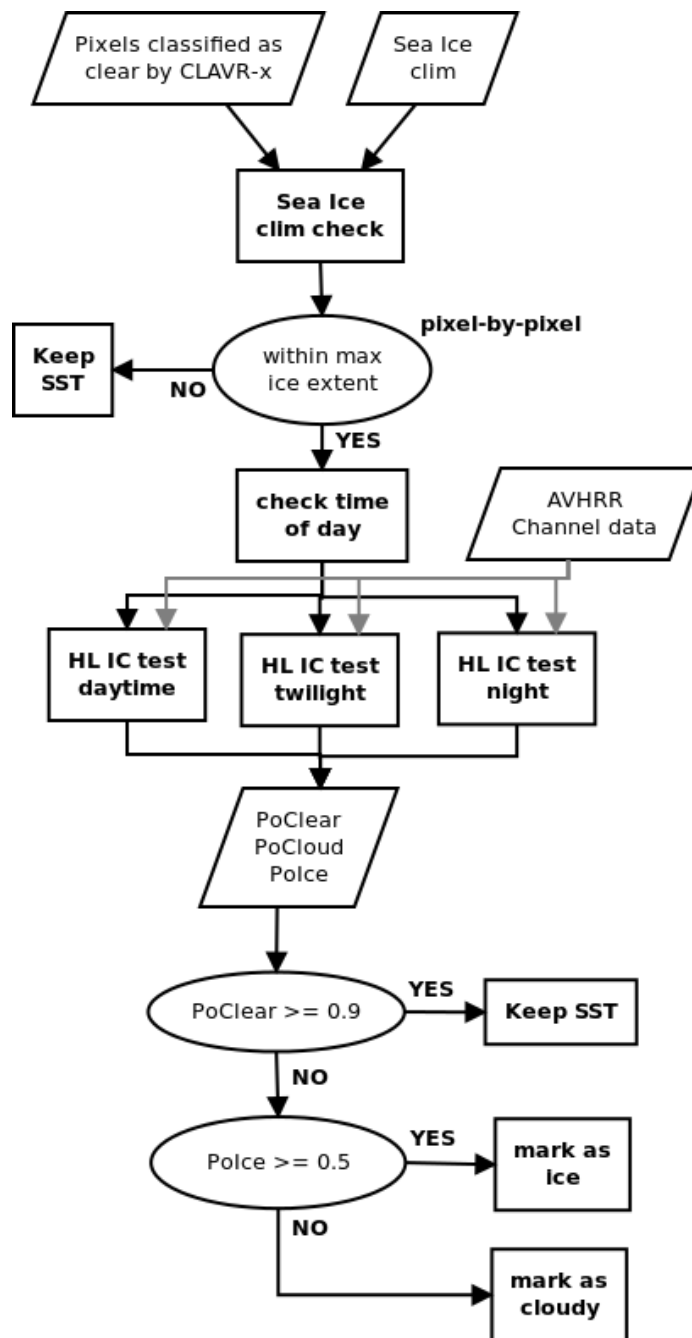
Figure 2.8. Flow chart for high latitude ice and cloud masking.

2.3.1.3　　High Latitude cloud and ice masking step

The High Latitude cloud and ice masking shown in the flow chart in Figure 2.8 has been developed in the SST-CCI project. It is described in full detail here.

The High Latitude step is run on all pixels classified as clear-open-water by CLAVR-x. The pixel is checked against a monthly maximum sea ice extent climatology, which is described in section 2.3.2.2. If the pixel is outside the area of maximum sea ice extent for the relevant month, no further tests are performed on that pixel and the estimated SST value is kept.

This document is to be used with the ESA SST_cci Version 1 (v1) products.

CCI Phase 1 (SST)   SST_CCI-ATBDV2-UOE-001
SST CCI Algorithm Theoretical Basis Document v2   Issue 1

For those pixels that fall within the maximum sea ice extent, the time of day is checked and a daytime, twilight or nighttime ice and cloud probability calculation test is run. The outputs from these tests are the same; the probability of pixel being clear-open-water, cloud covered and ice covered (Po_{Clear}, Po_{Cloud}, Po_{Ice}). These probabilities are calculated using a naive Bayesian approach, as described in more detail in RD.274 (section 2.3.2).

Finally, if Po_{Clear} is larger than 0.9, the pixel is regarded as clear of cloud and ice, and the SST estimate is kept. If not, it is regarded as cloud covered or ice covered. If Po_{Ice} is larger than 0.5 the pixel is classified as ice, otherwise it is classified as cloud.

2.3.2   Inputs to AVHRR High Latitude Extension

2.3.2.1   Primary Sensor Data

The satellite data used are AVHRR-GAC data from the satellites NOAA-12, 14, 15, 16, 17, 18, 19 and METOP-2, and include satellite and sun geometry data. The channel combinations used are as follows:

$re_{0.9}/re_{0.6}$ ratio between the reflectance in the 0.9 µm and 0.6 µm channels (AVHRR channel 2 and AVHRR channel 1)

$re_{1.6}/re_{0.6}$ ratio between the reflectance in the 1.6 µm and 0.6 µm channels (AVHRR channel 3A and AVHRR channel 1). [Not available for NOAA 12 and 12].

$bt_{3.7} - bt_{11}$ difference in brightness temperature of the 3.7 µm and 11 µm channels, (AVHRR channel 3/3B and channel 4)

$bt_{3.7} - bt_{12}$ difference in brightness temperature of the 3.7 µm and 12 µm channels, (AVHRR channel 3/3B and channel 5)

$LSD(bt_{3.7} - bt_{12})$ local standard deviation in the difference between the 3.7 µm and 11 µm channels.

The LSD operator is described in section 2.3.3.1.

In addition the following satellite geometry data are used:

- SOZ – solar zenith angle.

2.3.2.2   Ancillary Data

The cloud and ice masking algorithm takes as input monthly maximum sea ice extent climatology. This climatology is based on an ocean mask from the National Snow and Ice Data Centre (NSIDC), available here:

http://nsidc.org/data/smmr_ssmi_ancillary/ocean_masks.html.

This climatology has been produced by NSIDC using the Scanning Multichannel Microwave Radiometer (SMMR) and the Special Sensor Microwave/Imager (SSM/I) monthly averaged ice concentrations and finding the maximum extent for each month between 1979 and 2007. A zone of 350 km has been added to the maximum extent NSIDC maps to insure that the masks extend beyond the areas where sea ice is ever likely to occur. This climatology is provided at 12.5 km resolution, on a Lambert Azimuthal projection in NetCDF3 format. Examples are shown in Figure 2.9.
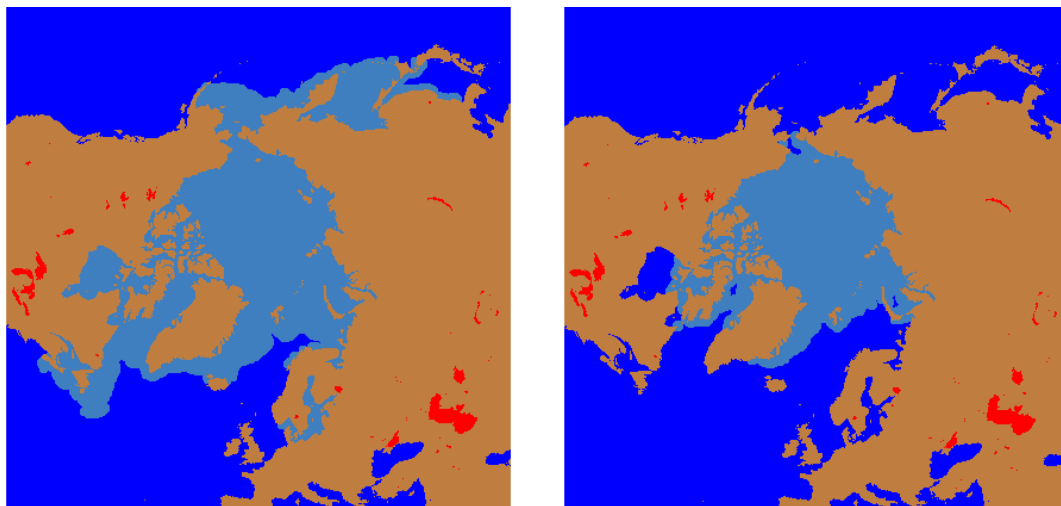
This document is to be used with the ESA SST_cci Version 1 (v1) products.

CCI Phase 1 (SST)   *SST_CCI-ATBDV2-UOE-001*
SST CCI Algorithm Theoretical Basis Document v2   *Issue 1*

Figure 2.9. Climatological maximum sea ice extent during March (left) and September (right). Lakes without climatology are marked in red.

2.3.2.3 Forward Models

Forward modeling is not used for the AVHRR high latitude cloud and ice mask extension.

2.3.3 Mathematical Description of AVHRR High Latitude Extension

This section describes the theoretical parts of the algorithm in more details.

2.3.3.1 Physical principals and equations

This section describes the physical and mathematical symbols and formulas used in the description of the algorithm.

Following is a summary of the symbols used to define the algorithm.

Po_{Clear}

The probability of a pixel being clear-open-water.

Po_{Cloud}

The probability of a pixel being cloud covered.

Po_{Ice}

The probability of a pixel being covered by ice.

$LSD(x)$

Local standard deviation, defined as the standard deviation of the variable x in a 3x3 pixel matrix around the data point in question, including the data point itself. In the case where the data point is on a swath line edge, LSD is defined as the standard deviation of the remaining closest neighbor points around the data point.

$dist_{\text{WTP}}(x), dist_{\text{WTP}}(x, y)$

Distance between observation x in a certain channel feature (channel value or channel combination) and a water tiepoint (WTP) of this channel feature. The water tiepoint is the mean value for this feature over clear-open-water. The mean value is found by selecting all pixels in the training data set that are classified as clear-open-water and then finding the average of those pixels in the given channel feature. This clear-open-water tiepoint might itself depend on another channel feature y (such as solar zenith angle or $bt_{11} - bt_{12}$).

$NormalDist(x, M, S)$

Probability distribution value of x in a normal distribution with mean M and standard deviation S, defined as

$$NormalDist(x, M, S) = S\sqrt{2\pi} * e^{\left(\frac{-pow((x-M),2.0)}{2*pow(S,2.0)}\right)}$$

$LogNormalDist(x, M, S)$

Probability distribution value of x in a log normal distribution. In this distribution the natural logarithm of the variable has a normal distribution with mean M and standard deviation S. The probability distribution function is defined as

$$LogNormalDist(x, M, S) = \frac{1}{C} e^{-0.5z^2}$$

where

$$z = \frac{(\log(x) - M)^2}{S^2}$$

$$C = x * S * \sqrt{2\pi}$$

$prob(\text{var|class, x})$

Probability of an observation x from the variable *var*, given that that surface observed is of a given surface class (clear-over-water, sea-ice, or cloud). This probability depends on the probability density function chosen for this variable and class. For the high latitude ice and cloud algorithm only normal and log-normal distributions are used, and hence this probability density function is one of these two functions:

$$prob_N(\text{var|class, x}) = NormalDist\big(\text{x}, \text{M(var, class)}, \text{S(var, class)}\big)$$

$$prob_{LN}(\text{var|class, x}) = LogNormalDist\big(x, M(var, class), S(var, class)\big)$$

Bayesian probabilities for Ice, Water and Cloud

The functions for calculating the Bayesian probabilities of ice, water and cloud depends on how many variables are used. The high latitude ice and cloud masking algorithm uses two variables, var1 and var2. These two variables are the selected AVHRR channel combinations that have been shown to be the best suited for separating ice, water and cloud (e.g. $RE_{1.6}$, $RE_{0.6}$) [RD.318]. As described in SST-CCI RD.274, the probabilities for the three classes given observation x in var_1 and y in var_2 can then be written as follows:

$$BayesProb_{\text{Ice}}(x,y) = prob(var_1|ice,x) * \frac{prob(var_2|ice,y)}{p_{sum}(x,y)}$$

$$BayesProb_{\text{Water}}(x,y) = prob(var_1|water,x) * \frac{prob(var_2|water,y)}{p_{sum}(x,y)}$$

$$BayesProb_{\text{Cloud}}(x,y) = prob(var_1|cloud,x) * \frac{prob(var_2|cloud,y)}{p_{sum}(x,y)}$$

where

$$
\begin{aligned}
p_{\text{sum}}(x,y) &= prob(var_1|ice,x) * prob(var_2|ice,y) + prob(var_1|water,x) \\
&\quad * prob(var_2|water,y) + prob(var_1|cloud,x) * prob(var_2|cloud,y)
\end{aligned}
$$

2.3.3.2 Calculations

This section describes the algorithm calculations in detail.

The high latitude ice and cloud masking extension has three main stages, as described in section 2.3.1.3. The first test (maximum ice climatology check) and the last stage (probability check) are clearly described in section 2.3.1.3, and no further details are provided here. The second test (calculation of probabilities) is more complex and further details are provided here.

The calculation of probabilities for each pixel being covered by ice, cloud or clear-open-water is split into three functions; one for daytime, one for twilight and one for night time conditions. Which function to use is decided by checking the pixel's solar zenith angle (SOZ),

Daytime: 0° <= SOZ <= 70°

Low sun: 70° < SOZ < 90°

Night time: SOZ >= 90°

Daytime probability calculation

The daytime probability calculation uses the naive Bayesian classifier (described in SST-CCI RD.274) with two channel combinations as input. The first channel combination is $RE_{0.9}/RE_{0.6}$. The second depends on which channels are available on the AVHRR instrument. If channel 3A ($RE_{1.6}$) is available, the channel combination $RE_{1.6}/RE_{0.6}$ is used. If $RE_{1.6}$ is not available, the channel combination $BT_{3.7} - BT_{11}$ is used.

The probability of ice, water and cloud is calculated using the functions described in section 0, with these two options of input channels:

$$BayesProb_{\text{Ice}}\left(\frac{RE_{0.9}}{RE_{0.6}}, \frac{RE_{1.6}}{RE_{0.6}}\right)$$

$$BayesProb_{\text{Water}}\left(\frac{RE_{0.9}}{RE_{0.6}}, \frac{RE_{1.6}}{RE_{0.6}}\right)$$

$$BayesProb_{\text{Cloud}}\left(\frac{RE_{0.9}}{RE_{0.6}}, \frac{RE_{1.6}}{RE_{0.6}}\right)$$

or

$$BayesProb_{\text{Ice}}\left(\frac{RE_{0.9}}{RE_{0.6}}, BT_{3.7} - BT_{11}\right)$$

$$BayesProb_{\text{Water}}\left(\frac{RE_{0.9}}{RE_{0.6}}, BT_{3.7} - BT_{11}\right)$$

$$BayesProb_{\text{Cloud}}\left(\frac{RE_{0.9}}{RE_{0.6}}, BT_{3.7} - BT_{11}\right)$$

These Bayesian probability functions depend on the probability density functions for each variable and class. The coefficients for these PDFs are provided in section 2.3.3.3. In these Bayesian functions the normal distribution is used for all the variables and classes. The PDF coefficients are constant for $RE_{0.9}/RE_{0.6}$ and $RE_{1.6}/RE_{0.6}$, and vary linearly as a function of solar zenith angle for $BT_{3.7} - BT_{11}$. The linear functions for the mean (M) and the standard deviation (S) are defined as:

$$M = MA * SOZ + MB$$

$$S = SA * SOZ + SB$$

All the coefficients are provided in Table 2.7.

Low sun probability calculation

For low sun cases (70<SOZ<90), the same Bayesian functions are used as for day. Only normal distributions are used. The only difference is that the PDF coefficients all vary linearly as a function of solar zenith angle. All coefficients are provided in Table 2.8.

Night time probability calculation

For night time cases (SOZ >= 90) the probability of ice, water and cloud depends on a different set of channel combinations:

$$BayesProb_{Ice}\left(dist_{WTP}(BT_{3.7} - BT_{12}, BT_{11} - BT_{12}), LSD(BT_{3.7} - BT_{12})\right)$$

$$BayesProb_{Water}\left(dist_{WTP}(BT_{3.7} - BT_{12}, BT_{11} - BT_{12}), LSD(BT_{3.7} - BT_{12})\right)$$

$$BayesProb_{Cloud}\left(dist_{WTP}(BT_{3.7} - BT_{12}, BT_{11} - BT_{12}), LSD(BT_{3.7} - BT_{12})\right)$$

The distance to water tiepoint, $dist_{WTP}$, uses the channel combination $BT_{3.7} - BT_{12}$. The water tiepoints in $BT_{3.7} - BT_{12}$ depend linearly on $BT_{11} - BT_{12}$ in this way:

$$tp_{water} = tp_{WAA} * (BT_{11} - BT_{12}) + tp_{WAB}$$

A normal distribution is used for the $dist_{WTP}$, variable. The local standard deviation, LSD, , in the channel combination $BT_{3.7} - BT_{12}$ uses normal distribution for water and ice, and log-normal distribution for clouds.

All coefficients are provided in Table 2.9.

2.3.3.3   Look-Up Table Description

This section describes the look-up tables used by the algorithm.

Daytime PDFs

Table 2.7. Coefficients for daytime cloud, water and ice PDFs, mean (M) and standard deviation (S) values. Coefficients A and B are for the linear function which depends on solar zenith angle.

Feature	Satellite	MA Cloud	MB Cloud	SA Cloud	SB Cloud	MA Water	MB Water	SA Water	SB Water	MA Ice	MB Ice	SA Ice	SB Ice
re09/re06	avhrr.12	0.00000	0.85281	0.00000	0.04682	0.00000	0.38893	0.00000	0.07425	0.00000	0.69591	0.00000	0.08343
re09/re06	avhrr.14	0.00000	0.96286	0.00000	0.05668	0.00000	0.46845	0.00000	0.07664	0.00000	0.83564	0.00000	0.10712
re09/re06	avhrr.15	0.00000	0.85934	0.00000	0.04591	0.00000	0.45613	0.00000	0.09711	0.00000	0.71348	0.00000	0.08896
re09/re06	avhrr.16	0.00000	1.00201	0.00000	0.08391	0.00000	0.49379	0.00000	0.05268	0.00000	0.78652	0.00000	0.09502
re09/re06	avhrr.17	0.00000	0.97274	0.00000	0.07145	0.00000	0.49986	0.00000	0.05124	0.00000	0.81967	0.00000	0.10337
re09/re06	avhrr.18	0.00000	0.97274	0.00000	0.07145	0.00000	0.49986	0.00000	0.05124	0.00000	0.81967	0.00000	0.10337
re09/re06	avhrr.19	0.00000	0.97274	0.00000	0.07145	0.00000	0.49986	0.00000	0.05124	0.00000	0.81967	0.00000	0.10337
re09/re06	avhrr.M2	0.00000	0.97274	0.00000	0.07145	0.00000	0.49986	0.00000	0.05124	0.00000	0.81967	0.00000	0.10337
re16/re06	avhrr.17	0.00000	0.72693	0.00000	0.23643	0.00000	0.11614	0.00000	0.06288	0.00000	0.09602	0.00000	0.05110
re16/re06	avhrr.M2	0.00000	0.72313	0.00000	0.23673	0.00000	0.10658	0.00000	0.06581	0.00000	0.08964	0.00000	0.05165
bt37-bt11	avhrr.12	-0.56348	69.35526	0.00000	13.63244	-0.00018	-0.22443	0.00000	0.40911	-0.13988	11.35302	0.00000	1.43857
bt37-bt11	avhrr.14	-0.34541	45.87440	-0.04061	12.95126	-0.00363	-0.00948	-0.00371	0.65188	-0.11360	10.27040	-0.05884	5.66529
bt37-bt11	avhrr.15	-0.25533	48.29366	0.00000	14.09327	-0.00130	0.53671	0.00000	0.58704	-0.09010	8.76945	0.00000	1.31814
bt37-bt11	avhrr.16	-0.38364	60.66684	0.00000	14.71542	0.00880	-0.19203	0.00000	0.56054	-0.09794	8.63588	0.00000	1.17303
bt37-bt11	avhrr.17	-0.31430	44.17989	-0.02694	12.65744	-0.00702	0.28810	-0.00607	0.80616	-0.05909	5.86810	-0.04862	4.85154
bt37-bt11	avhrr.18	-0.31430	44.17989	-0.02694	12.65744	-0.00702	0.28810	-0.00607	0.80616	-0.05909	5.86810	-0.04862	4.85154
bt37-bt11	avhrr.19	-0.31977	44.41623	-0.04062	13.43065	-0.00199	0.20798	-0.00434	0.68304	-0.02195	3.63142	-0.03212	3.76327
bt37-bt11	avhrr.M2	-0.31977	44.41623	-0.04062	13.43065	-0.00199	0.20798	-0.00434	0.68304	-0.02195	3.63142	-0.03212	3.763

Low sun PDFs

Table 2.8. Coefficients for low sun cloud, water and ice PDFs, mean (M) and standard deviation (S) values. Coefficients A and B are for the linear function which depends on solar zenith angle.

Feature	Satellite	MA Cloud	MB Cloud	SA Cloud	SB Cloud	MA Water	MB Water	SA Water	SB Water	MA Ice	MB Ice	SA Ice	SB Ice
re09/re06	avhrr.12	0.00583	0.45108	0.00453	-0.26367	0.00156	0.26167	0.00081	0.00522	0.00085	0.61656	0.00001	0.08067
re09/re06	avhrr.14	0.00249	0.81170	0.00322	-0.16418	0.00680	-0.02092	-0.00151	0.16632	-0.00176	0.96871	-0.00175	0.23960
re09/re06	avhrr.15	0.00742	0.37190	0.00461	-0.26915	-0.00460	0.78057	-0.00037	0.10901	-0.00215	0.93308	-0.00008	0.09755
re09/re06	avhrr.16	0.00352	0.79392	0.00212	-0.06511	0.00366	0.24588	-0.00193	0.18403	0.00316	0.55905	0.00220	-0.06487
re09/re06	avhrr.17	0.00432	0.69152	0.00261	-0.10628	0.00228	0.36877	-0.00128	0.12892	0.00025	0.78506	-0.00024	0.12318
re09/re06	avhrr.18	0.00554	0.61246	0.00259	-0.10782	0.00422	0.20235	-0.00123	0.13233	-0.00114	0.89733	0.00017	0.10009
re09/re06	avhrr.19	0.00641	0.53107	0.00241	-0.09328	0.00460	0.18173	-0.00189	0.17628	-0.00240	1.04805	0.00151	-0.01988
re09/re06	avhrr.M2	0.00441	0.68548	0.00265	-0.10751	0.00372	0.25285	-0.00213	0.19982	0.00117	0.71995	-0.00034	0.13009
re16/re06	avhrr.17	-0.00035	0.74791	0.00001	0.22789	0.00005	0.11209	-0.00111	0.13291	-0.00013	0.11627	-0.00014	0.05621
re16/re06	avhrr.M2	-0.00097	0.77669	-0.00056	0.27837	0.00121	0.02402	-0.00116	0.13967	0.00013	0.09111	-0.00020	0.06397
bt37-bt11	avhrr.12	-1.00387	100.18210	-0.15530	24.50319	0.00534	-0.61087	0.00872	-0.20153	-0.06709	6.25776	-0.00693	1.92355
bt37-bt11	avhrr.14	-0.81486	78.73564	-0.14252	20.08538	0.01219	-1.11710	0.00240	0.22361	-0.09941	9.27680	-0.02231	3.10805
bt37-bt11	avhrr.15	-1.00285	100.62026	-0.17166	26.10963	-0.02880	2.46204	-0.01085	1.34667	-0.11211	10.30992	-0.01966	2.69413
bt37-bt11	avhrr.16	-1.46363	136.26590	-0.32002	37.11670	-0.02121	1.90920	-0.01203	1.40245	-0.07151	6.78563	-0.01865	2.47865
bt37-bt11	avhrr.17	-0.86394	82.65454	-0.25658	28.73197	-0.01483	0.83486	-0.00069	0.42907	-0.09409	8.31815	-0.04490	4.59092
bt37-bt11	avhrr.18	-0.86394	82.65454	-0.25658	28.73197	-0.01483	0.83486	-0.00069	0.42907	-0.09409	8.31815	-0.04490	4.59092
bt37-bt11	avhrr.19	-0.83436	80.43717	-0.20255	24.76542	-0.02043	1.49843	-0.00797	0.93716	-0.10423	9.39069	-0.04826	4.89320
bt37-bt11	avhrr.M2	-0.83436	80.43717	-0.20255	24.76542	-0.02043	1.49843	-0.00797	0.93716	-0.10423	9.39069	-0.04826	4.89320

Night time PDFs

Table 2.9. Coefficients for night time cloud, water and ice PDFs, mean (M) and standard deviation (S) values. The water tiepoint coefficients are given in TA Water and TB Water. Empty cells mean that the coefficients are not used. Normal distribution mean and standard deviation coefficients are provided under LSD(bt37-bt12) and log-normal under ln(LSD(bt37-bt12)).

Satellite	M Cloud	S Cloud	M Water	S Water	M Ice	S Ice	TA Water	TB Water
avhrr.12	0.000	2.078	0.000	0.323	0.000	0.968	0.874	0.076
avhrr.14	0.000	2.187	0.000	0.295	0.000	0.884	1.067	-0.040
avhrr.15	0.000	2.094	0.000	0.258	0.000	0.774	0.906	0.037
avhrr.16	0.000	2.061	0.000	0.261	0.000	0.783	0.835	-0.018
avhrr.17	0.300	2.066	0.000	0.183	0.000	0.548	0.703	-0.152
avhrr.18	0.100	2.009	0.000	0.164	0.000	0.492	0.904	-0.433
avhrr.19	0.500	2.103	0.000	0.153	0.000	0.460	0.996	-0.397
avhrr.M2	0.100	2.057	0.000	0.144	0.000	0.433	0.767	-0.307
avhrr.12			0.310	0.118	0.920	0.236		
avhrr.14			0.190	0.074	0.539	0.148		
avhrr.15			0.130	0.054	0.385	0.108		
avhrr.16			0.140	0.054	0.375	0.109		
avhrr.17			0.130	0.056	0.357	0.113		
avhrr.18			0.100	0.056	0.336	0.113		
avhrr.19			0.100	0.055	0.316	0.111		
avhrr.M2			0.100	0.058	0.340	0.116		
avhrr.12	-0.392	0.425						
avhrr.14	-0.622	0.588						
avhrr.15	-0.711	0.688						
avhrr.16	-0.721	0.690						
avhrr.17	-0.767	0.716						
avhrr.18	-0.795	0.752						
avhrr.19	-0.817	0.773						
avhrr.M2	-0.817	0.751						

2.3.3.4   Algorithm Output

The output of the AVHRR cloud and ice mask algorithm is the probability of each pixel being clear-open-water, ice covered and cloud covered. Each of these numbers is non-dimensional, is between 0.0 and 1.0 and together they sum up to 1.0. The three numbers are used to mark the respective pixels as clear-open-water, cloud covered or ice covered.

2.3.4 Assumptions and Limitations

2.3.4.1   Algorithm Performance

During the development and tuning of the high latitude ice and cloud masking algorithm, some assumptions that might influence the algorithm have been made. These assumptions are listed in this section.

For the PDFs that have been developed, it has been assumed that they are Gaussian normal distributions. This is a simplification that holds for a large part of the range of observations for the chosen channel combinations, but not for all. Under very low sun conditions or at very high satellite zenith angles the observed distributions might deviate from Gaussian distributions. Still, in most cases the Gaussian distribution holds and this assumption is a good one.

In some cases, the defined PDFs have shorter overlaps between the classes in one variable than is observed. This sometimes happens in the range of observations where it is very difficult to separate the classes with the variable in question. This might lead to a more certain classification than it should.

It is assumed that the PDFs do not change with satellite zenith angle. The PDFs have been developed using data covering all satellite zenith angles. This will have a small impact on textural features such as local standard deviation (LSD), which is smoother at higher satellite zenith angles.

For this algorithm it is assumed that there is no difference in prior probability between ice, water and cloud.

Under twilight conditions, the ability to separate the different classes decreases with increasing solar zenith angle, mainly for solar zenith angles between 80° and 90°. So the algorithm performance is worse with increasing solar zenith angle during twilight.

Under night time conditions it is very difficult to discriminate between clouds and ice, due to the spectral characteristics of ice and clouds being very similar in the three available AVHRR channels. Therefore the night time algorithm cannot be expected to perform well in separating clouds and ice, but should work reasonably well in separating clear-open-water from clouds or ice.

2.3.4.2   Sensor Performance

Some assumptions have been made concerning the sensor performance during the algorithm development. The assumptions are listed in this section.

It is assumed that the radiometric data are consistently calibrated over time. It is also assumed that the radiometric data do not degrade over time and that the radiometric noise is constant. This is necessary for using PDFs that do not vary with time. The check

on the calibration of the radiometric data must be handled elsewhere in the processing chain.

2.3.5 Future Enhancements

One possible enhancement is to introduce different prior probabilities to the three classes: ice, water and cloud. The ice and water prior probabilities could for example depend on a sea ice concentration product.

3. RETRIEVAL OF SKIN SEA SURFACE TEMPERATURE FROM THERMAL INFRARED SENSORS

3.1 Optimal Estimator for AATSR and ATSR-2

3.1.1 General formulation for reduced-state vector optimal estimation for SST

Optimal estimation (OE) was first discussed in reference to SST retrieval in Merchant et al., 2008 [RD.221]; this is the method that has been used to retrieve the SST from ATSR-2 and AATSR data. In the OE methodology described, *a priori* expectations, x_a, about the state of the atmosphere and ocean are used as inputs to a forward model, F, to simulate prior observations, y_a, which represent the expected brightness temperatures (BT), i.e. $y_a = F(x_a)$. The state variables x_a are from numerical weather prediction (NWP) data and the forward model F is the radiative transfer model RTTOV10.2. The sea surface emissivity is taken from the ATSR Reprocessing for Climate (ARC) emissivity model and a reflectivity correction based on the method of Watts et al. [RD.297] has been applied. The sensitivity of the simulated BTs to variations in the state variables, K, is defined using the tangent linears to the forward model. These sensitivities are combined with the difference between the observed and simulated BTs $(y_o - F(x_a))$, to optimally modify the prior estimate of the state, which includes the SST. The retrieved state variables, $\hat{x}$, are estimated using:

$$\hat{x} = x_a + G(y_o - F(x_a)) = x_a + (K^T S_\varepsilon^{-1} K + S_a^{-1})^{-1} K^T S_\varepsilon^{-1}(y_o + F(x_a)) \quad (3.1)$$

G is the gain matrix that operates on the observed minus simulated BT difference (this is described in detail in RD.307). $.S_\varepsilon$ is the error covariance of the model and satellite observations of the BTs. These are a combination of the radiometric noise in the observations and estimated uncertainty of the forward model. It is assumed that the radiometric noise and the forward model errors are uncorrelated between channels. The impact of this assumption is discussed in RD.221. S_a is the error covariance matrix for the prior state variables. Using 3.1, the retrieved state is optimal in the sense that it will give an unbiased, minimum standard deviation estimate of the state if (i) the prior information are unbiased and (ii) the forward model is unbiased [RD.221].

It was shown in RD.221 that a reduced state vector based on the leading modes of variability can be used in the optimal estimation of the state. The SST and TCWV variability are associated with the first two dominant modes of variability in the BTs, so these two state variables are used to define the reduced state vector ($z(x) = \begin{bmatrix} x \\ w \end{bmatrix}$), where x represents the SST and w represents the TCWV. It should be noted that the full state vector x_a is still used to calculate the simulated BTs. Use of the reduced state vector in the OE reduces the size of the S_a error covariance matrix to 2×2. In this case it can be assumed that the errors in the state variables are uncorrelated.

Merchant et al. [RD.295] demonstrate that the uncertainty in the OE retrieved SST is reduced if the prior TCWV error variance is constructed so as to account for the limitations in the NWP fields used to define the prior state. The prior TCWV error variance used in generating the SST CCI data is detailed in Table 3.1, There is a trade-off between the SST error variance (the dispersion of uncertainty in the retrieval) and both the SST bias and SST sensitivity. Specifying a large prior SST error variance (larger than the true uncertainty of the prior SST) ensures that the retrieved SST is minimally biased by the prior SST and has SST sensitivity close to 100% [RD.295]. The set of formulations used in the reduced state-vector OE is listed in Table 3.1.

Table 3.1. Parameters in the SST CCI optimal estimator for AATSR and ATSR-2

Aspect of optimal estimator	Assumption/configuration
Prior SST, x_a	'ERA Interim' skin sea surface temperature
Error SD in prior, e_{xa}	5 K
Prior full state vector, $\boldsymbol{x}_a$	'ERA Interim' surface pressure plus atmospheric profiles of temperature and humidity on ECMWF model pressure levels
Prior TCWV, $\boldsymbol{w}_a$	The vertical integral of the water vapour absolute humidity from the full state vector $\boldsymbol{x}_a$
Error in prior TCWV, e_{wa}	$w(ae^{-bw} + c)$ [w in kg m^{-2}] where $a = 0.42$; $b = 0.05$; $c = 0.042$
Prior error covariance matrix, $\boldsymbol{S}_a$	$\begin{pmatrix} e_{xa}^2 & 0 \\ 0 & e_{wa}^2 \end{pmatrix}$
Forward model for simulated BTs	RTTOV10.2
Forward model error, $\boldsymbol{\varepsilon}_{RT}$	$e_{RT} \sec\theta$, where θ is the satellite zenith angle and $e_{RT} = 0.15$ K for 3.7 µm; 0.16 for 11 µm; 0.17 for 12 µm
Pixel-level BT noise equivalent differential temperature / K	Linear interpolation with respect to pixel BT of the NEDTs measured viewing the hot and cold on-board black bodies, using the following data:

	ATSR-2		AATSR	
	Cold BB	Hot BB	Cold BB	Hot BB
BB temp. / K	256.2	299.9	262.0	300.9
3.7 µm NEDT	0.1064	0.0364	0.0745	0.0310
11 µm NEDT	0.0586	0.0524	0.0651	0.0695
12 µm NEDT	0.0651	0.0695	0.0337	0.0316

Aspect of optimal estimator	Assumption/configuration
Prior BT covariance matrix, $\mathbf{S}_\varepsilon$.[1]	$\begin{bmatrix} \varepsilon_{3.7n}{}^2 + \varepsilon_{RT}{}^2 & 0 & 0 & 0 & 0 & 0 \\ 0 & \varepsilon_{11n}{}^2 + \varepsilon_{RT}{}^2 & 0 & 0 & 0 & 0 \\ 0 & 0 & \varepsilon_{12n}{}^2 + \varepsilon_{RT}{}^2 & 0 & 0 & 0 \\ 0 & 0 & 0 & \varepsilon_{3.7f}{}^2 + \varepsilon_{RT}{}^2 & 0 & 0 \\ 0 & 0 & 0 & 0 & \varepsilon_{11f}{}^2 + \varepsilon_{RT}{}^2 & 0 \\ 0 & 0 & 0 & 0 & 0 & \varepsilon_{12f}{}^2 + \varepsilon_{RT}{}^2 \end{bmatrix}$
Tangent linear matrix [2], $\mathbf{K}$	$\begin{bmatrix} \dfrac{\partial y_{3.7n}}{\partial x} & \dfrac{\partial y_{11n}}{\partial x} & \dfrac{\partial y_{12n}}{\partial x} & \dfrac{\partial y_{3.7f}}{\partial x} & \dfrac{\partial y_{11f}}{\partial x} & \dfrac{\partial y_{12f}}{\partial x} \\ \dfrac{\partial y_{3.7n}}{\partial w} & \dfrac{\partial y_{11n}}{\partial w} & \dfrac{\partial y_{12n}}{\partial w} & \dfrac{\partial y_{3.7f}}{\partial w} & \dfrac{\partial y_{11f}}{\partial w} & \dfrac{\partial y_{12f}}{\partial w} \end{bmatrix}$

[1] Here ε_{Xv} indicates the channel at wavelength X µm in the view V (nadir, n, or forward, f). When using fewer channels, the corresponding rows and columns are omitted. $\boldsymbol{\varepsilon}_{RT}$ depends on channel wavelength and satellite zenith angle.

[2] y_{Xv} indicates the channel at wavelength X µm in the view V (nadir, n, or forward, f). The partial derivatives with respect to w require an assumption about how water vapour changes at different altitudes are related. The assumption made is that the fractional change in absolute humidity is the same for all altitudes. When a particular channel/view is not included in the retrieval, the corresponding column of $\mathbf{K}$ is omitted.

The optimal estimator formulated in this way approximates a hybrid *maximum a posteriori /maximum likelihood* (MAP/ML) solution. Since the prior TCWV error variance is chosen to be approximately representative of the uncertainty in prior *w*, the estimator is a MAP solution in that respect. Since the prior SST error standard deviation, at 5K, is an order of magnitude greater than the true prior SST uncertainty (of order 0.6 K), the bias towards the prior SST is minimised, sensitivity is maximised and the estimator is an approximate ML solution with respect to SST.

3.1.2 Forward model adjustments for bias minimisation

OE formulated as ML with respect to SST should give an unbiased estimate provided that the forward model is unbiased relative to the observations. Since the target is for the retrieved SST to be unbiased to within 0.1 K, the forward model needs to be unbiased relative to the observations in each channel to within << 0.1 K. Both the channel-integrating nature of the fast radiative transfer model and the calibration accuracy of the AATSR and ATSR-2 BTs mean that an uncertainty of << 0.1 K cannot be assumed for every channel on these sensors. Therefore, an adjustment to the forward modelled BTs is required before the retrieval of the SSTs using the OE method.

An unbiased prior SST is required to accurately determine the forward model bias. The SST product developed in the ARC project [RD.296] has sufficiently low bias to be suitable for correcting for forward model bias. A set of quality controlled observations from a Multi-sensor Match-up Database (MMD) are used to construct the forward model bias correction. The process is summarised in Figure 3.1. Suitable observations are selected from the MMD and SSTs are simulated using the ARC retrieval coefficients applied to the observed BTs. These simulated SSTs are then combined with NWP fields and the BTs are calculated using the forward model. The bias adjustment is calculated by fitting a function to the simulated minus observed (S-O) BTs that depends on parameters identified as a source of forward model bias.
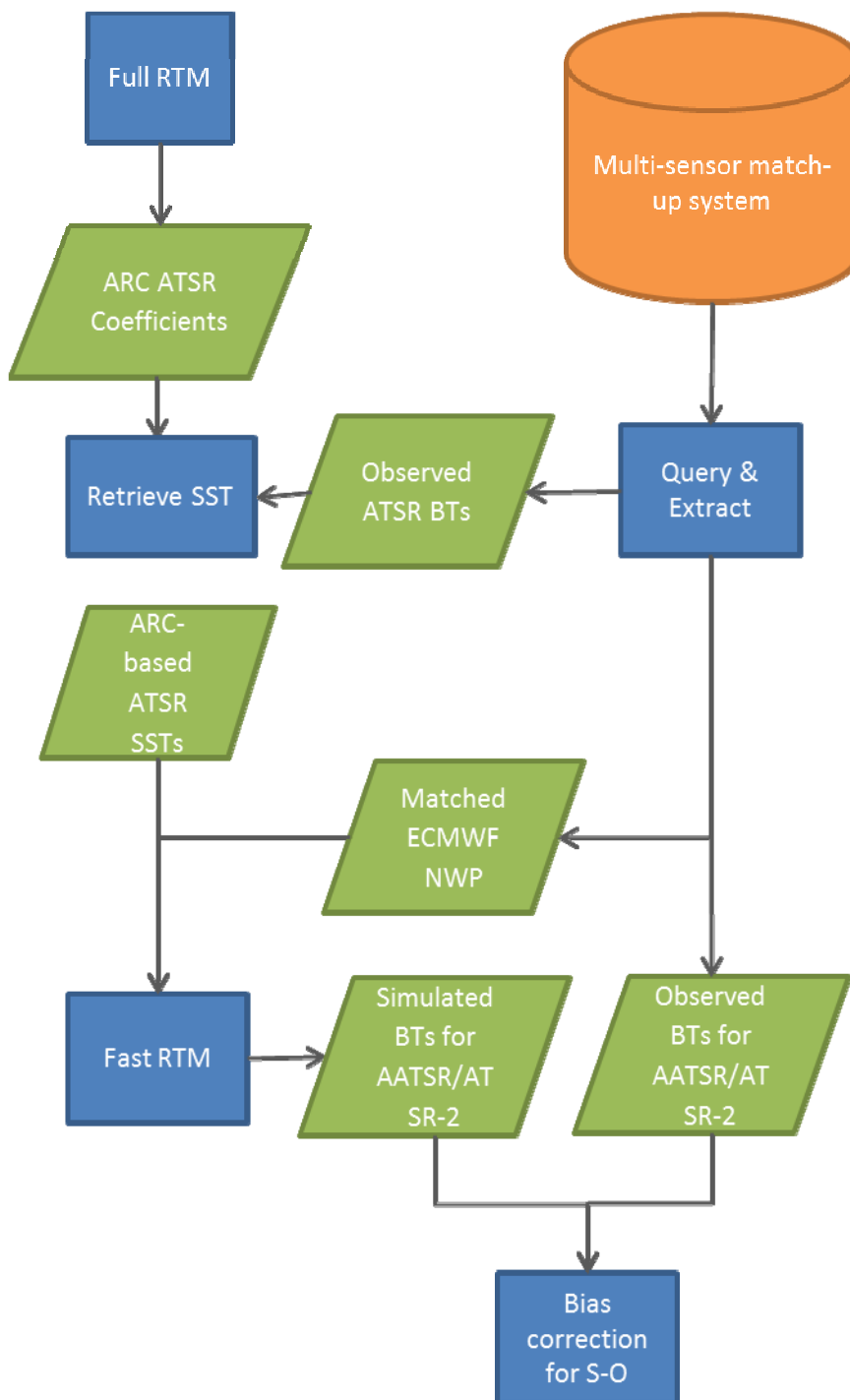
Figure 3.1. Flow diagram showing the simulation minus observation (S-O) bias correction process. 'ATSR' here is either AATSR or ATSR-2. The fast radiative transfer model (RTM) is RTTOV 10.2. The full RTM is a line-by-line model.

For the ATSR sensors, the bias adjustment for the MMD S-O difference is parameterised using the formula:

$$y_a^{\text{adjusted}} = y_a - (a + bJ) - \left(c + dw + \frac{ew}{\cos(\theta)} + f\ln(w) + gT_{\text{diff}}\right) \qquad (3.2)$$

where

J is the number of days since 00:00 UTC 1 Jan 2000 (J is negative for earlier dates)

w is the prior total column water vapour, kg m^{-2}

θ is the satellite view zenith angle

T_{diff} is the prior skin SST minus the minimum (tropopause) temperature in the NWP profile

These predictors are justified by the nature of the likely errors in forward modelling and calibration, respectively:

bJ drift in calibration over time

$\partial w + \frac{ew}{\cos\theta} + f\ln(w)$ errors from spectral approximation in radiative transfer and/or spectral response uncertainty that have different behaviours with respect to the TCWV

T_{diff} errors from spectral approximation in radiative transfer and/or spectral response uncertainty depending on the temperature contrast across the troposphere

The coefficients *a … g* were obtained by ordinary least squares regression against S-O values extracted with NWP information from the SST CCI multi-sensor matchup database [RD.232].

The bias adjustment coefficients are defined for each channel, view and sensor in Table 3.2. It may be noticed that the term *bw* is much larger for the AATSR 12 μm channel than for other channels. This reflects a systematic error in this channel, suspected to be linked to uncertainty in the spectral response function of this channel in flight, which is discussed in RD.186.

Table 3.2. Bias adjustment coefficients applied to RTTOV BT simulations

	a	*b*	*c*	*d*	*e*	*F*	*g*
AATSR							
12n	0.05295756	0.00338215	-0.79032085	-0.040807702	0.027067579	0.16586370	0.007654017
11n	0.094677947	-9.3149603E-06	-0.42181691	-0.034205357	0.026009239	0.099363880	0.004157997
3.7n	-0.057381770	-4.9043523E-06	-0.27717829	-0.029821493	0.021352979	0.075355428	0.002787283
12f	0.14189303	0.00397353	-0.74354480	0.031034069	-0.028438285	0.20199601	0.007462564
11f	0.10780302	-1.4868328E-05	-0.56740023	0.044941997	-0.033358798	0.19245244	0.004233160
3.7f	-0.014928819	-6.1923075E-06	-0.43715274	0.024626578	-0.021525511	0.13907145	0.003601326
ATSR-2							
12n	0.19487751	3.5315173e-05	-0.90643508	-0.043672887	0.028476719	0.18702661	0.007550045
11n	0.11590252	2.3662987e-05	-0.49421170	-0.044683273	0.034695967	0.10992667	0.004169421
3.7n	-0.11389527	5.8083874e-06	-0.33416882	-0.030353188	0.019632113	0.091340954	0.003316309
12f	0.27668353	3.3933909e-05	-0.88119003	0.040174393	-0.035010815	0.22670855	0.007328980
11f	0.13832849	2.4887296e-05	-0.67738481	0.055810016	-0.041553816	0.21919086	0.004178803
3.7f	-0.084070699	8.5364835e-06	-0.54631403	0.020146209	-0.021095221	0.16718704	0.004631343

3.1.3 Channel combinations

The SSTs used in the ATSR L3U products in the CCI [RD.175] are always dual-view SSTs, which are least likely to be biased by anomalous atmospheric conditions and aerosol loadings. If the solar zenith angle exceeds 92.5° for a given nadir pixel, then the dual-view three-channel retrieval is used, and the K and S_ε matrices are defined as in Table 3.1. If the solar zenith angle is less than 87.5 the 3.7 μm channel is not used to avoid possible biasing from solar reflection and scattering. In this case, only the rows and columns relevant to the 11n, 11f, 12n and 12f channels are retained in K and S_ε. When the solar zenith angle is between 87.5° and 92.5° the pixel is considered to be in twilight and no SST retrieval is made.

3.2 Optimal estimator for AVHRRs

3.2.1 General formulation for reduced-state vector optimal estimation for SST

The principles of the optimal estimator for the AVHRRs are identical to those described in section 3.1.1. Essentially, the same retrieval algorithm is applied to the AVHRRs:

$$\hat{x} = x_a + \mathrm{G}\big(y_o - \mathrm{F}(x_a)\big) = x_a + (K^T S_\varepsilon^{-1} K + S_a^{-1})^{-1} K^T S_\varepsilon^{-1}(y_o + \mathrm{F}(x_a)) \qquad (3.3)$$

The retrieved state $\hat{x}$ is the prior state plus an increment of $\mathrm{G}\big(y_o - \mathrm{F}(x_a)\big)$. The matrix K expresses how the observations change for departures from the prior state x_a, i.e., it is a matrix where a given row contains the partial derivatives of the BT in a particular channel with respect to each element of the state vector in turn. The partial derivatives are the tangent linears output from the forward model F. S_ε is the error covariance of the prior and satellite observations of the BTs. These include the radiometric noise in the observations and estimated uncertainty of the forward model. S_a is the error covariance matrix for the prior state variables.

The OE formulation operates on a reduced state vector $z(x) = \begin{bmatrix} x \\ w \end{bmatrix}$, which includes only SST (x) and TCWV (w). The formulations used in the reduced state-vector OE for AVHRRs are listed in Table 3.3.

This document is to be used with the ESA SST_cci Version 1 (v1) products.

CCI Phase 1 (SST)   SST_CCI-ATBDV2-UOE-001
SST CCI Algorithm Theoretical Basis Document v2   Issue 1

Table 3.3. Parameters in the SST CCI optimal estimator for AVHRRs

Aspect of optimal estimator	Assumption/configuration
Prior SST, x_a	'ERA Interim' skin sea surface temperature
Error SD in prior, e_{xa}	5 K
Prior full state vector, x_a	'ERA Interim' surface pressure plus atmospheric profiles of temperature and humidity on ECMWF model pressure levels
Prior TCWV, w_a	The vertical integral of the water vapour absolute humidity from the full state vector x_a
Error in prior TCWV, e_{wa}	$w(ae^{-bw} + c)$ [w in kg m^{-2}] $a = 0.42;\ b = 0.05;\ c = 0.042$
Prior error covariance matrix,	$\begin{pmatrix} e_{xa}^2 & 0 \\ 0 & e_{wa}^2 \end{pmatrix}$
Forward model for simulated BTs	RTTOV10.2
Forward model error, ε_{RT}	$e_{RT}\sec(\theta)$, where θ is the satellite zenith angle and $e_{RT} = 0.15$ K for 3.7 μm; 0.16 for 11 μm; 0.17 for 12 μm
Pixel-level BT noise equivalent differential temperature / K	0.06 K at 300 K Scaled by Planck function at other temperatures (i.e., assumes constant radiance error standard deviation).
Prior BT covariance matrix. [1]	$\begin{bmatrix} \varepsilon_{3.7}^2 + \varepsilon_{RT}^2 & 0 & 0 \\ 0 & \varepsilon_{11}^2 + \varepsilon_{RT}^2 & 0 \\ 0 & 0 & \varepsilon_{12}^2 + \varepsilon_{RT}^2 \end{bmatrix}$
Tangent linear matrix [2], K	$\begin{bmatrix} \dfrac{\partial y_{3.7}}{dx} & \dfrac{\partial y_{11}}{dx} & \dfrac{\partial y_{12}}{dx} \\ \dfrac{\partial y_{3.7}}{dw} & \dfrac{\partial y_{11}}{dw} & \dfrac{\partial y_{12}}{dw} \end{bmatrix}$

[1] Here ε_x indicates the channel at wavelength x μm. When using fewer channels, the corresponding rows and columns are omitted. $\mathcal{E}_{RT}$ depends on channel wavelength and satellite zenith angle.

[2] y_x indicates the channel at wavelength x μm. The partial derivatives with respect to w require an assumption about how water vapour changes at different altitudes are related. The assumption made is that the fractional change in absolute humidity is the same for all altitudes. When a particular channel/view is not included in the retrieval, the corresponding column of K is omitted.

The optimal estimator formulated in this way approximates a hybrid *maximum a posteriori / maximum likelihood* (MAP/ML) solution.

3.2.2 Forward model adjustments for bias minimisation

As with the ATSR-2 and AATSR sensors, a bias correction to the forward model is required to ensure that the OE delivers SSTs within the required target bias. SSTs based on the ARC retrieval are used as the prior SST for the forward model. The bias adjustment for AVHRRs relies on multi-sensor matches in the MMD between AVHRR and either ATSR-2 or AATSR so that the ARC based SST can be retrieved for the prior state. The ARC SSTs are assumed to be an unbiased reference for skin SST. The process for constructing the forward model bias adjustments is described by Figure 3.2.

The AVHRR and ATSR observations in the MMD will not necessarily be coincident in time, so in order to provide an estimate for skin SST at the time of the AVHRR observation (t_{AVHRR}) any change in SST since the ARC SST observation time (t_{ATSR}) associated with heating or cooling of the upper ocean must be accounted for. This is done using the time series of the matched drifting buoy data, which is assumed to capture any change in the sub-skin SST. The drifting buoy time series is interpolated to the ARC and AHVRR SST times, and the difference in sub-skin SST, $dSST = SST_{buoy}(t_{AVHRR}) -$

This document is to be used with the ESA SST_cci Version 1 (v1) products.

CCI Phase 1 (SST)   *SST_CCI-ATBDV2-UOE-001*
SST CCI Algorithm Theoretical Basis Document v2   *Issue 1*

$SST_{\mathrm{buoy}}(t_{\mathrm{ATSR}})$ is found. The skin temperature at the time of the AVHRR is then assumed to be:

$$SST_{\mathrm{skin}}(t_{\mathrm{AVHRR}}) = SST_{\mathrm{skin}}(t_{\mathrm{ATSR}}) + dSST \tag{3.4}$$

$SST_{\mathrm{skin}}(t_{\mathrm{AVHRR}})$ is then used together with the atmospheric state defined by NWP data as input to the forward model to calculate the simulated BTs. The bias adjustment is calculated by fitting a function to the simulated minus observed (S-O) BTs that depends on parameters identified as a source of forward model bias.
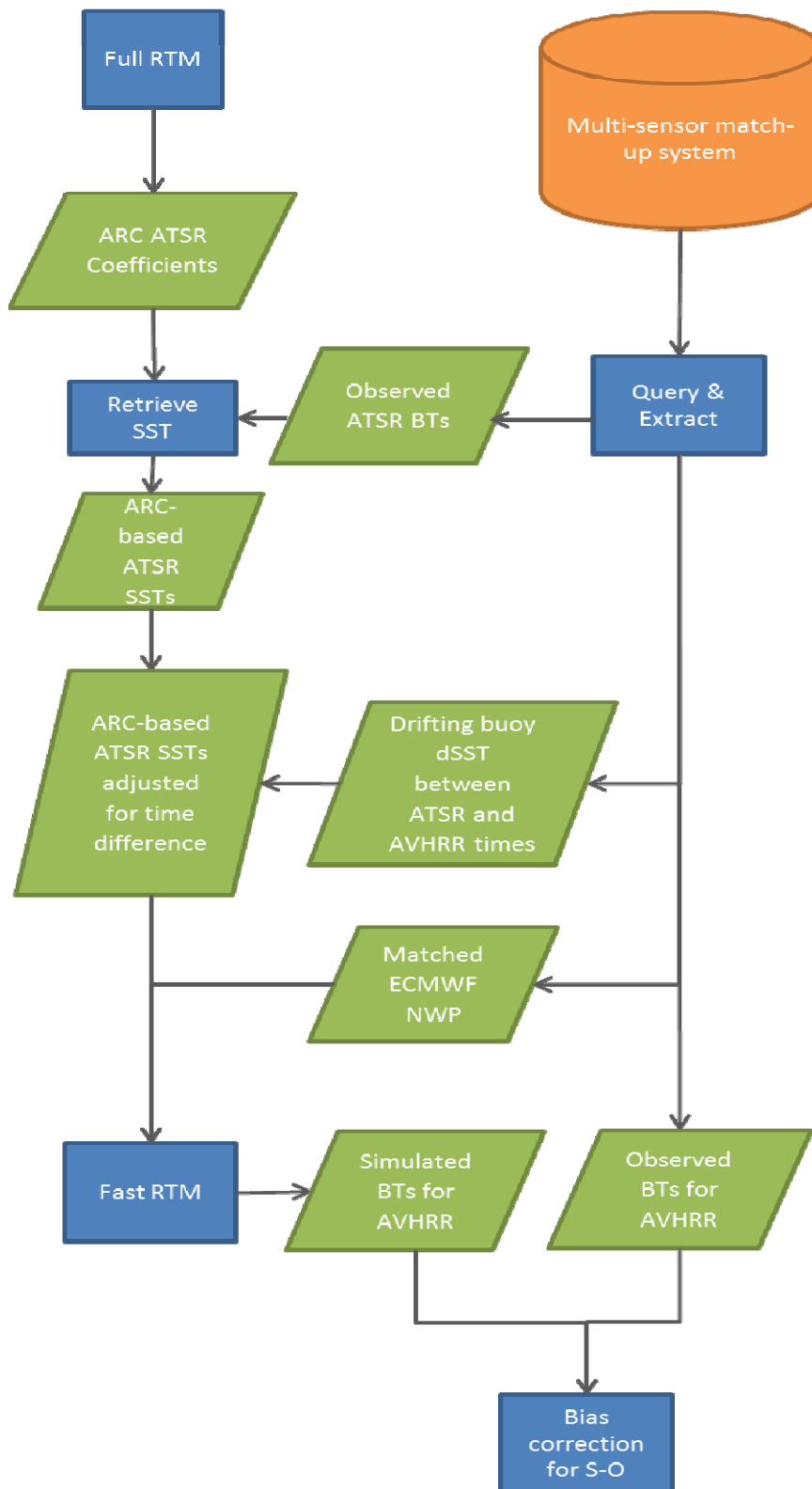
Figure 3.2. Flow diagram showing the simulation minus observation (S-O) bias correction process. 'ATSR' here is either AATSR or ATSR-2, and AVHRR is any of the AVHRR series. The fast radiative transfer model (RTM) is RTTOV 10.2. The full RTM is a line-by-line model.

This document is to be used with the ESA SST_cci Version 1 (v1) products.

CCI Phase 1 (SST)
SST CCI Algorithm Theoretical Basis Document v2

SST_CCI-ATBDV2-UOE-001
Issue 1

For the AVHRRs, the bias adjustment for the S-O difference is parameterised using the formula:

$$y_a^{\text{adjusted}} = y_a - (a + bT_{\text{inst}}) - \left(c + dw + e\,\frac{w}{\cos\theta} + f\ln(w) + gT_{\text{diff}} + h\,\frac{1}{T_{\text{diff}}} + i\,\frac{1}{w} + j\,\frac{1}{\cos\theta} \right)$$

(3.5)

where

T_{inst} is the AVHRR instrument temperature in K

w is the prior total column water vapour, kg m^{-2}

θ is the satellite view zenith angle

T_{diff} is the prior skin SST minus the minimum (tropopause) temperature in the NWP profile

These predictors for AVHRR extend the set described previously for ATSR (terms with coefficients *h, i and j*) as systematic differences in S-O remained when using the ATSR set defined in Section 3.1.2. The secular trend term for the ATSR (*bJ*) is replaced with a term using the AVHRR instrument temperature *bT$_{inst}$* since it is temporal changes in instrument temperature that dominate secular changes in calibration for AVHRR [RD.298].

The coefficients *a … j* were obtained by ordinary least squares regression against S-O values extracted with NWP information from the SST CCI MMD [RD.232]. The AVHRR bias adjustment coefficients are defined for each channel, view and sensor in Table 3.4.

3.2.3 Channel combinations

The SSTs used in the AVHRR L2P products in the CCI [RD.175] are two or three channel, depending on the zenith angle. If the solar zenith angle exceeds 92.5° for a given nadir pixel, then the nighttime channel combination of the 3.7, 11 and 12 μm channels is used. If the angle is less than 87.5° the daytime channel combination of the 11 and 12 μm channels is used. When the solar zenith angle is between 87.5° and 92.5° twilight conditions are assumed and no SST retrieval is made.

Table 3.4. Bias adjustment coefficients applied to RTTOV BT simulations for AVHRRs

Instrument	Channel	*a*	*b*	*c*	*d*	*e*
avhrr12	3.7	-1.03061	0.077237	-3.70636	-0.03775	0.006652
avhrr12	11	-0.80425	0.054159	-3.62532	-0.05081	0.005569
avhrr12	12	-0.438	0.054002	-3.86683	-0.05197	0.006259
avhrr14	3.7	-1.56519	0.103146	-5.9979	-0.03369	0.004536
avhrr14	11	-1.25922	0.089544	-7.45862	-0.05767	0.00495
avhrr14	12	-1.30708	0.113816	-9.47586	-0.07386	0.0055
avhrr15	3.7	-0.45629	0.020175	-2.08524	-0.02735	0.007016
avhrr15	11	-0.46203	0.020167	-1.66913	-0.03818	0.012122
avhrr15	12	-0.1661	0.008715	-3.92234	-0.04931	0.013497
avhrr16	3.7	-0.26174	0.015522	-3.08428	-0.02621	0.005479
avhrr16	11	-0.38161	0.040191	-3.62038	-0.04197	0.006465
avhrr16	12	-0.15195	0.034111	-5.16817	-0.04233	0.004744
avhrr17	3.7	-0.36679	0.015311	-2.84477	-0.02306	0.001323
avhrr17	11	-0.72575	0.041975	-2.97294	-0.03736	0.003977
avhrr17	12	-0.24191	0.020228	-4.6363	-0.04635	0.003929
Avhrr18	3.7	-0.01902	-3.4E-05	-3.75325	-0.02813	0.00584
Avhrr18	11	0.180827	-7.2E-05	-4.5128	-0.05002	0.006281
Avhrr18	12	0.35517	-8.5E-05	-6.10092	-0.05897	0.007411
METOP	3.7	0.045147	2.51E-05	-2.88074	-0.02561	0.002296
METOP	11	0.244829	8.89E-07	-3.56358	-0.04184	0.003466
METOP	12	0.32171	-1.7E-05	-5.27331	-0.05008	0.004427
avhrr12	3.7	0.896	0.009679	61.4904	4.53109	-0.13791
avhrr12	11	1.16359	0.007681	53.9317	6.3168	-0.38073
avhrr12	12	1.17069	0.009603	50.6755	6.09757	-0.32723
avhrr14	3.7	0.796622	0.026348	163.481	3.01015	-0.16712
avhrr14	11	1.41212	0.026807	173.988	6.26934	-0.29316
avhrr14	12	1.82222	0.032955	206.417	7.87981	-0.22626
avhrr15	3.7	0.333638	0.010501	59.1744	1.17352	-0.15591
avhrr15	11	0.454843	0.009632	46.5326	2.28835	-0.53748
avhrr15	12	0.760821	0.020532	95.6446	2.99385	-0.5675
avhrr16	3.7	0.434046	0.01413	76.9577	1.47884	-0.03366
avhrr16	11	0.771271	0.015453	70.5886	2.73357	-0.23495
avhrr16	12	0.854712	0.02552	99.5349	2.5106	-0.1554
avhrr17	3.7	0.506768	0.010097	59.6432	2.26119	0.062472
avhrr17	11	0.808006	0.007742	47.231	4.09093	-0.14516
avhrr17	12	1.08598	0.015624	70.183	4.94242	-0.14976
Avhrr18	3.7	0.538535	0.015978	95.4981	2.31826	-0.06211
Avhrr18	11	1.0595	0.015836	75.1678	4.81396	-0.22542
Avhrr18	12	1.22955	0.024756	115.412	5.15026	-0.26487
METOP	3.7	0.540084	0.00969	60.2711	2.56414	0.044283
METOP	11	0.888782	0.011344	58.5913	4.21618	-0.1422
METOP	12	1.11008	0.020242	94.9059	4.92797	-0.19408

3.3 Estimator for ATSR-1 SSTs

In order to use the same optimal estimator for ATSR-1, the following extensions would be necessary:

- extend the state vector to include stratospheric aerosol
- extend the forward model to model stratospheric aerosol
- provide a prior estimate and error variance for stratospheric aerosol
- extend the forward model to accommodate the changing spectral response function of the 12 μm channel associated with the trend in ATSR-1 detector temperature over the mission
- develop a model of ATSR-1 noise accounting for noise pick-up from the Stirling cycle cooler

In the absence of these developments, the algorithm selection exercise [RD.226] concluded that ARC SST retrieval coefficients would be used for ATSR-1 within the SST CCI. Note that this choice remains consistent with the optimal estimators used for all other IR SST retrievals as these are bias-corrected using ARC coefficient-based SSTs (sections 3.1.2 and 3.2.2).

The full description of ARC SST retrieval process is given in RD.184, RD.185 and RD.186. The following sections present key points on the calculation of the retrieval coefficients.

3.3.1 Basis in radiative transfer

With improvements in the spectroscopic data describing water vapour continuum absorption, the coefficients used for SST retrieval are routinely calculated using radiative transfer modelling of TOA radiances. Compared with empirical regression methods, this approach has the advantage that the retrieval coefficients are independent of in situ observations which is beneficial for climate research. Figure 3.3 provides a schematic illustration of the process used to generate SST retrieval coefficients using simulated data. The calculation of the retrieval coefficients requires the simulation of the clear-sky TOA radiances that would be measured by infrared sensors. The forward model used to simulate the TOA clear-sky radiance values consists of a radiative transfer model (RTM), spectroscopic data, sensor spectral response functions, and a representative set of states describing the atmosphere and sea surface on which to perform the simulations. The simulated TOA radiance values are compared with observed radiance for clear-sky conditions to determine uncertainties and bias. The simulated TOA radiance values and the corresponding state SSTs are used to calculate the SST retrieval coefficients. The SST retrieval is then applied to the observed TOA radiance values and the retrieved SSTs are validated against in situ observations of the SST.
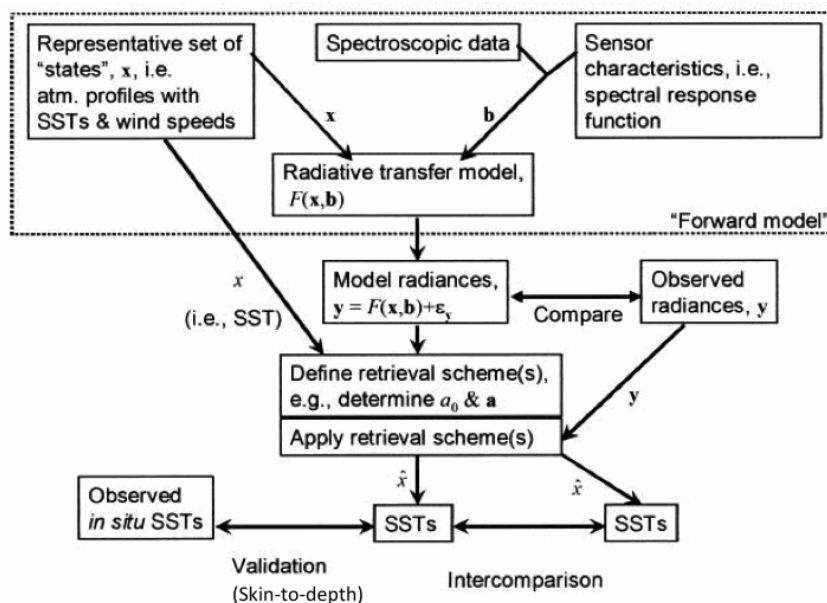
Figure 3.3. Schematic of the process for defining and validating coefficients for sea surface temperature retrieval using radiative transfer modelling [RD.253].

3.3.1.1   Clear-sky radiative transfer model

To achieve the required accuracy in the TOA radiance values, - the line-by-line Reference Forward Model (RFM; www.atm.ox.ac.uk/**RFM**/) was used. The effects of tropospheric and stratospheric aerosols and gases interacting with radiation must be simulated. For the ARC reprocessing, the scattering by aerosol particles with radii comparable to the wavelengths of thermal infrared radiation measured by the sensors, was calculated using the DISORT scattering model [RD.300]. This was applied to channel integrated clear-sky transmittances derived from the line-by-line RFM calculations.

RFM was used as it meets the following criteria [RD.301] for simulation of brightness temperatures suitable for determining SST coefficients:

- It is capable of simulating radiances at a spectral resolution of 0.01 cm^{-1} or better.
- It includes CO_2 line mixing.
- It is capable of modelling continuum features for water vapour and nitrogen.
- It can calculate radiance with the assumption that the Planck function varies linearly with altitude and that optical depth varies linearly with path within each layer.
- It can enable linear interpolation for profiles of absorber quantities.
- Voigt line shapes are used for all molecules as default (Lorentz and Doppler line shapes can be selected individually).
- It includes all trace gases that have an impact of >0.001 K on TOA BTs, for any channel eg. H_2O, CO_2, O_3, N_2O, CH_4, NH_3, HNO_3, OCS, H_2CO, N_2, C_2H_6, F11, F12, F22, F113, F114, CCl_4, HNO_4.
- IT uses the HITRAN spectroscopic database.

3.3.1.2   Spectral Emissivity Model

The spectral emissivity model described in RD.186 was adopted for the calculation of the ARC coefficients. The emissivity model uses an isotropic wave facet model to include the wavelength dependence on the refractive index of seawater, temperature, wind

This document is to be used with the ESA SST_cci Version 1 (v1) products.

CCI Phase 1 (SST)
SST CCI Algorithm Theoretical Basis Document v2

SST_CCI-ATBDV2-UOE-001
Issue 1

roughening of the sea surface and incident and emission angles of radiation relative to the ocean surface.

The salinity effect on refractive index was found to be negligible so is not included in this model. The model results have been tabulated and are available in RD.320. The emissivity data are presented as a function of wavenumber (600-3350 cm^{-1}), view angle (0-85°), temperature (270-310 K), and wind speed (0-25 m s^{-1} at 12.5m).

3.3.1.3 Atmospheric Meteorological Profiles for Radiative Transfer

A representative distribution of simulated TOA BTs is required to calculate the SST retrieval coefficients. This requires a representative distribution of atmospheric states – i.e. profiles of atmospheric temperature, water vapour and associated surface variables. There are two distinct sources of suitable data: (i) measurements in the form of radiosondes, and (ii) simulated data from numerical weather prediction (NWP) models. For the calculation of the ARC retrieval coefficients, NWP data from the ECMWF 40-year reanalysis (ERA-40) were used as these give a more representative global sample compared with radiosonde data. ERA-40 consists of 6-hourly surface and profile data (on 60 pressure levels) covering the years 1957 to 2001, on a 2.5° horizontal grid. Due to resource restrictions such a large data set could not be processed, so basic temporal sampling was applied leaving a subset of data covering all times of day for all seasons. These were extracted from the "60L-SD" data set [RD.302], used as the starting point for the ARC project database. This subset of the data was then filtered to remove:
- All land or mixed land/ocean profiles
- All profiles with >95% sea ice
- All profiles outside RTTOV's validity range for water vapour
- All profiles with >95% relative humidity for any layer (such profiles are indicative of near-total cloud cover conditions, not representative of clear skies under which SST retrievals are possible).

3.3.1.4 Trace gas profiles

Trace gases that affect simulated BTs by 1 mK or more were included in the simulations for ARC. Some gases have geographic or temporal variations that have a significant impact on BTs, whereas for less influential/variable trace gases, global profiles may be used. The trace gases used in ARC along with whether annual or latitudinal variations were represented are listed in Table 3.5. All the trace gases have secular trends that were accounted for. Details of the trends, annual and latitudinal variations used are given in RD.301 and RD.186.

Table 3.5. Trace gases included in simulations for coefficients and the aspects of variability accounted for in each case.

Gas	Long Term Trend	Annual Cycle	Latitudinal Variation
NH_4	Y	N	N
HNO_3	Y	Y	Y
N_2O	Y	N	Y
CH_4	Y	N	Y
CFC 11	Y	N	Y
CFC 12	Y	N	Y
CO_2	Y	N	N

This document is to be used with the ESA SST_cci Version 1 (v1) products.

CCI Phase 1 (SST)   SST_CCI-ATBDV2-UOE-001
SST CCI Algorithm Theoretical Basis Document v2   Issue 1

3.3.1.5   Aerosol simulations

Tropospheric aerosol number density was assumed to follow an exponential height distribution

$$N(z) = N(0)e^{(-z/h)} \tag{3.6}$$

where $N(0)$ is the aerosol concentration at the surface, h is the scale height in kilometres, and z is the altitude. The OPAC dataset contains a set of aerosol profiles of this form. These aerosol profiles are associated with a range of different geographical locations, and differ in terms of the components present and surface concentrations. The Global Aerosol Data Set (GADS) was used alongside the optical property dataset (OPAC) to give a good representation of the tropospheric aerosol profiles.

Major volcanic eruptions (Mt. Pinatubo and Mt. Hudson, both in 1991) significantly changed the stratospheric aerosol throughout the ATSR-1 mission. Stratospheric aerosols produced by major volcanic eruptions need to be simulated in order to ensure aerosol robustness of coefficients. In situ measurements of stratospheric aerosol size distribution are available for a 30 year period at Laramie, Wyoming [RD.304]. These data provided vertical profiles of both the number density and size distribution fitted using a bimodal lognormal function. The primary mode represents the more numerous small particles, the secondary mode the larger particles which have a greater impact on infra-red scattering. These data were used to define a background number density and the change associated with volcanic aerosols. The primary mode showed negligible variation with time so a single number distribution was derived from the data using equation 3.6, where the coefficients based on height are:

z = 12 – 24 km, $N(0)$ = 2146.9 cm^{-3}, h = 2.85921 km
z = 24 – 32 km, $N(z)$ = 4 cm^{-3}
z < 12km or > 32 km, $N(z)$ = 0 cm^{-3}.

The particle radius was fixed at 0.025 µm.

The secondary mode was found to vary from year to year, however it was sufficient to define a single number density profile which was scaled by year for the background.

z = 12 – 24 km, $N(z)$ = 0.173 cm^{-3}
z = 24 – 32 km, $N(0)$ = 4.04370×10^{6} cm^{-3}, h = 1.41467 km
z < 12km or > 32 km, $N(z)$ = 0 cm^{-3}.

The scale factors for the stratospheric number density profile by year are [RD.186]:

Table 3.6: Scale factors for the stratospheric aerosol number density profile as a function of year.

Year	1991	1992	1993	1994	1995	1996	1997+
Scale	1.0	20.0	9.0	4.0	1.5	0.5	0.3

The particle radius for the secondary mode was constant at 0.35 µm for the background level, but during the years affected by volcanic aerosol (1992-1994) the lower level aerosol distribution increased linearly with decreasing height. During 1992/1993 the particle size increased from 0.35 µm at 24 km to 0.75 µm at 12 km, while during 1994 the size increased from 0.35 µm at 24 km to 0.55 µm at 12 km.

This document is to be used with the ESA SST_cci Version 1 (v1) products.

CCI Phase 1 (SST)   *SST_CCI-ATBDV2-UOE-001*
SST CCI Algorithm Theoretical Basis Document v2   *Issue 1*

3.3.2 Calculation of retrieval coefficients

The ARC SST estimate, $\hat{x}$, is formed from a weighted combination of BTs.

$$\hat{x} = a_0 + \boldsymbol{a}^T \boldsymbol{y} \tag{3.7}$$

Here a_0 is the offset coefficient, and $\boldsymbol{a}^T = [a_1, \dots, a_n]$ is a vector of n weighting coefficients for the n BTs in the observation vector ($\boldsymbol{y}$). These observations may consist of infrared observations at different wavelengths and/or view angles. The superscript ^{T} indicates the transpose of the vector.

The offset and weighting coefficients are found using least squares minimization techniques. These minimize the mean square difference between the "true" SST input to the RTM and the "retrieved" SST, for the population of atmospheric and surface states and associated RTM BTs outlined in section 3.3.1. The weights and offset term are given by the formulas:

$$\boldsymbol{a} = \boldsymbol{S}'^{-1}_{yy} \left[\boldsymbol{S}_{xy} - \boldsymbol{K} \left(\boldsymbol{K}^T \boldsymbol{S}'^{-1}_{yy} \boldsymbol{K} \right)^{-1} \left(\boldsymbol{K}^T \boldsymbol{S}'^{-1}_{yy} \boldsymbol{s}_{xy} \right) \right] \tag{3.8}$$

$$a_0 = \bar{x} - \boldsymbol{a}^T \overline{\boldsymbol{y}} \tag{3.9}$$

where

$$\boldsymbol{S}'^{-1}_{yy} = \boldsymbol{S}_{yy} + \boldsymbol{S}_{\varepsilon}$$

x is the "true" SST associated with a given set of simulated BTs ($\boldsymbol{y}$)

$\boldsymbol{S}_{yy}$ is the covariance matrix of observations

$\boldsymbol{S}_{\varepsilon}$ is the covariance matrix for the noise equivalent differential temperature [RD.321]

$\boldsymbol{s}_{xy}$ is the covariance vector of SST and observations.

$\boldsymbol{K}$ is a matrix containing the impacts on BTs of the presence of stratospheric aerosol, $\partial y / \partial \sigma$, where σ is the stratospheric aerosol optical depth. The over-bars indicate mean values are used. The covariance matrix of the observations $\boldsymbol{S}_{yy}$ is defined as:

$$\boldsymbol{S}_{yy} = \overline{\boldsymbol{y}\boldsymbol{y}^T} - \overline{\boldsymbol{y}}\,\overline{\boldsymbol{y}}^T \tag{3.10}$$

and the covariance vector of SST and the observations, $\boldsymbol{s}_{xy}$, is given by:

$$\boldsymbol{s}_{xy} = \overline{x\boldsymbol{y}^T} - \overline{x}\,\overline{\boldsymbol{y}}^T \tag{3.11}$$

Use of the $\boldsymbol{K}$ matrix to represent the effects of aerosol ensures the retrieval coefficients are robust to the presence of stratospheric aerosol since this formulation forces the coefficients to be orthogonal to the effects of the aerosols.

The coefficients are calculated at predefined values of the following parameters:
- satellite zenith angle in the nadir view
- satellite zenith angle in the forward view
- prior TCWV
- instrument detector temperature
- year

The coefficients applied for a given SST retrieval are found by interpolating the tabulated values based on these parameters. Bilinear interpolation is used to interpolate the satellite zenith angles, and linear interpolation used for the other parameters.

3.4   Estimates of Uncertainty

Estimates are generated for four sources of uncertainty [RD.306]: (i) uncertainty due to radiometric noise, (ii) uncertainty in retrieval (e.g. insufficient information in the channel to derive an SST estimate), (iii) uncertainty due to large scale effects, and (iv) the uncertainty in the adjustment for diurnal variability (method described in section 6).

For OE2, the uncertainty due to radiometric noise and uncertainty in retrieval are defined respectively as [RD.307]:

$$\sqrt{G \begin{bmatrix} \varepsilon_{3.7}{}^2 & 0 & \cdots \\ 0 & \varepsilon_{11}{}^2 & \cdots \\ \vdots & \vdots & \ddots \end{bmatrix} G^T} \tag{3.12}$$

and

$$\sqrt{G \left(\begin{bmatrix} \varepsilon_{RT}{}^2 & 0 & \cdots \\ 0 & \varepsilon_{RT}{}^2 & \cdots \\ \vdots & \vdots & \ddots \end{bmatrix} + \boldsymbol{K}\boldsymbol{S}_a\boldsymbol{K}^T \right) G^T} \tag{3.13}$$

where $\mathbf{G}$ is the gain matrix described in section 3.1.1. (Note: ε_{RT} depends on the channel wavelength and the satellite zenith angle).

The radiometric noise is assumed to be independent between pixels in an image; 3.12 estimates the SST uncertainty associated with uncorrelated effects. The remainder of the retrieval uncertainty is assumed to be partly correlated between pixels with length scales that are, at present, not well quantified, and are assumed to reflect the length scales of the atmosphere (synoptic length scales), with magnitude obtained from 3.13.

For the ATSR1 coefficient-based SST, uncertainty due to radiometric noise is estimated by the propagation of the noise through the retrieval equation. The uncertainty is given by the equation

$$\sqrt{\sum_i a_i^2 \varepsilon_i^2} \tag{3.14}$$

where

i   is the channel

εi   is the radiometric noise in channel i

a_i are the corresponding channel retrieval coefficients for channel i

For the uncertainty in the retrieval from algorithm effects, the magnitude is estimated from the residuals in representative simulations of the retrieval process. It is presently assumed that the same correlation length scales apply for the partly correlated effects in both coefficient-based and OE retrievals.

The uncertainty due to large-scale effects is set to be constant (0.1 K) representative of regional, seasonally persistent mean differences against validation values [RD.184].

This document is to be used with the ESA SST_cci Version 1 (v1) products.

CCI Phase 1 (SST)   SST_CCI-ATBDV2-UOE-001
SST CCI Algorithm Theoretical Basis Document v2   Issue 1

4.   GENERATION OF L2P AND L3U PRODUCTS AND PROPOGATION OF UNCERTAINTIES

This section describes the processing chain used to generate L2P and L3U outputs from the L1B satellite observations. The individual steps referred to are described in detail in other sections of the document as follows; cloud clearing (section 2), SST retrieval (section 3) and SST depth and time adjustments (sections 5 and 6).

4.1   Generating L2P Data from L1B Data

The first step in the processing chain is to cloud screen the input data (section 2). This is done using a Bayesian methodology for both the ATSR and AVHRR instruments, taking L1B observations and NWP data as input. For cloud free scenes the skin SST is retrieved using optimal estimation for ATSR-2, AATSR and the AVHRRs and coefficient based retrieval for ATSR-1 (section 3). Skin SST is then adjusted for both time and depth to provide a bulk SST at one of the two reference times, 10.30 or 22.30 local times (sections 5 and 6). For AVHRR instruments this per pixel data along with the associated uncertainties is output in L2P product format. Uncertainties associated with the SST retrieval are broken down into large scale correlated uncertainty, synoptically correlated uncertainty, uncorrelated uncertainty and time and depth adjustment uncertainty components, as well as providing a total value.

4.2   Generating L3U Data from L2P Data

For the ATSR instruments the data are averaged across 0.05° grid cells and provided as L3U products as the data resolution is much higher. Skin and depth SSTs are calculated within each grid cell using data classified as clear-sky during the cloud screening process. Uncertainties are also propagated onto the reduced resolution grid with the addition of a sampling error (section 4.3) and provided with same components as those described in section 4.1.

4.3   Computing estimates of uncertainty on the L3U grid Propagating Uncertainties from L2P Pixel Output to the L3U Grid

The SST variance for an L3U grid cell is calculated using all available clear-sky pixels

$$\sigma_{Skin\ SST} = \left(\overline{SST_{Clear\ Pixels}^2} - \left(\overline{SST_{Clear\ Pixels}} \right)^2 \right) * \frac{n_{clear}}{n_{clear}-1} \qquad (4.1)$$

where

$\sigma_{Skin\ SST}$ total error covariance

$SST_{Clear\ Pixels}$ skin SST for all clear sky pixels in the L3U grid cell

n_{clear} total number of clear-sky pixels in the in the L3U grid cell

If less than five clear-sky pixels are available in a given cell then a minimum error covariance of 0.04 K^2 is assumed.

The sample error variance is given by:

$$\varepsilon_{sample} = \sigma_{Skin\ SST} * \frac{n_{cloud}}{n_{total}-1} \tag{4.2}$$

where

ε_{sample} sample error covariance

n_{cloud} total number of cloudy pixels

n_{total} total number of pixels in L3U grid cell

The total error variance is assumed to be uncorrelated and increases with the number of cloudy pixels in the L3U grid cell

$$\varepsilon_{total} = \frac{\sum \varepsilon_{clear}}{\sqrt{n_{clear}}} + \varepsilon_{sample} \tag{4.3}$$

where

ε_{total} L3U SST error variance

ε_{clear} error variance for clear-sky pixels in L3U grid cell

4.4 Other Data Provided in the L2P and L3U Files

The L2P and L3U files also contain flags to assign each pixel or grid cell as land/ocean or sea ice and to record how many channels were used in the SST retrieval. If a pixel or grid cell crosses a boundary then both of the applicable conditions will be flagged.

5. MODEL OF SKIN-SUBSKIN DIFFERENCE IN SEA SURFACE TEMPERATURE

5.1 Background

The upper few millimetres of the ocean is referred to as the skin layer. This is cooler than the sub-skin layer immediately below due to latent and sensible heat exchanges with the atmosphere and surface emission of infrared radiation. The sub-skin layer exhibits a diurnal variation in temperature and depth, governed by absorption of solar radiation and wind driven mixing. The deeper mixed layer of the ocean lies below this and is largely unaffected by surface processes. The temperature of this layer is often referred to as the bulk sea surface temperature.

Space-borne infrared instruments measure the temperature of the upper few microns of the sea surface whilst in-situ data from buoys or ships are typically a measure of the bulk SST. Depth adjustment of the retrieved SST is necessary to meet user requirements of consistency between satellite and in-situ data records. The bulk SST is calculated from the skin SST in a two-step process, first correcting for the cooler skin layer and then for the warm sub-skin layer. This section describes the algorithm used to calculate the sub-skin SST from the skin SST and section 6 details the correction from the sub-skin temperature to the bulk SST.

5.2 Model Setup

The temperature difference (ΔT) between the skin and sub-skin SST is described by the following relationship [RD.319].

$$\Delta T = \frac{\lambda Q \upsilon}{k u_*} \qquad (5.1)$$

where

ΔT_c temperature difference across the skin to sub-skin layer (K)

Q total cooling at the ocean-atmosphere interface (W m^{-2})

δ thickness of the cool skin layer (m)

k thermal conductivity of water (Wm^{-1} K^{-1})

This can be parameterised under shear and buoyancy driven conditions denoted by subscripts (s) and (b) respectively [RD.227].

$$\Delta T_{cs} = \frac{\lambda Q \upsilon}{k u_{*w}} \qquad (5.2)$$

$$\Delta T_{cb} = \left(\frac{\upsilon}{A^3 g \alpha \rho c_p k^2}\right)^{1/4} Q / Q_b^{1/4} \qquad (5.3)$$

where

λ empirical coefficient

υ kinematic viscosity of water (m^2 s^{-1})

This document is to be used with the ESA SST_cci Version 1 (v1) products.

CCI Phase 1 (SST)   *SST_CCI-ATBDV2-UOE-001*
SST CCI Algorithm Theoretical Basis Document v2   *Issue 1*

ρ   density of sea water (kg m^{-2})

u_{*w} friction velocity in the ocean for turbulence generated by convection (m s^{-1})

A   empirical constant

g   gravitational acceleration (m s^{-2})

α   thermal expansion coefficient for water (K^{-1})

c_p specific heat capacity of water (J kg^{-1} K^{-1})

The Fairall model combines the shear and convective effects to define λ used in the calculation of the thickness of the cool skin layer (δ). This gives an expression for the skin depth that is valid both at low-wind speeds (when convective effects dominate) and at higher wind speeds (when shear dominates). In the Fairall model, λ is given by equation 5.4 where λ_0 and *A* are pre-determined coefficients, set to 6.0 and 0.23 respectively [RD.227].

$$\lambda = \lambda_0 \left[1 + \left(\frac{\lambda_0^4 A^3 Q g \alpha \rho c_p v^b}{u_{*a}^4 \left(\rho a / \rho \right)^2 k^2} \right)^{3/4} \right]^{-1/3} \tag{5.4}$$

We drive the Fairall model with ERA-Interim numerical weather prediction (NWP) data, available globally at 6 hour time intervals from 1979 [RD.38]. Over a wind speed range of 0-10 m s^{-1} this model has been shown to give the best estimate of the skin to sub-skin temperature difference [RD.262]. In RD.266 the optimal parameterisations of *A* and λ were considered. Figure 5.1 shows the temperature difference between the skin minus sub-skin ΔT at two different times (the observation and reference times). The reference time (t_0) is the time to which the SST measurements are adjusted, either 10.30 or 22.30 depending on the observation time. The black curve shows the model results using the Fairall coefficients (*A* = 0.23, λ = 6) and the grey curve the model results with an alternative proposed set of coefficients (*A* = 0.15, λ = 4.1) [RD.266]. The comparison is constructed using data from the SST CCI Multi-sensor Matchup Database (MMD) which contains both satellite observations and coincident in situ data. There is a maximum 0.03 K reduction in the mean SST difference between the cool skin and sub-skin layer between the model results using and the Fairall coefficients those using the new coefficients. The modelled sub-skin to bulk (0.2 m) temperature difference (shown in pale grey) indicates that the warm layer has a negligible contribution to this difference.
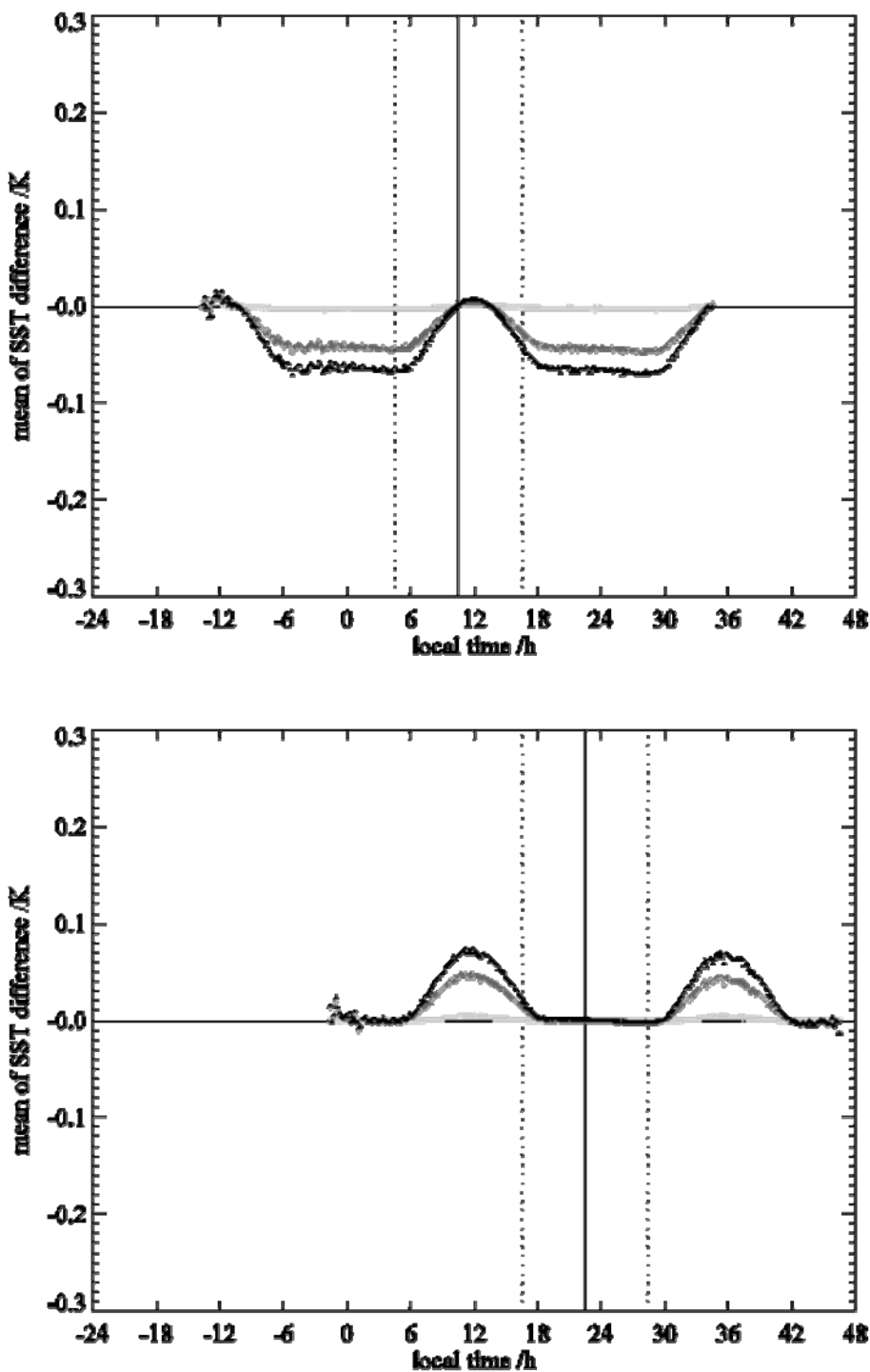
Figure 5.1. Plots show the mean SST difference with hours from the reference time (10.30 for the top panel, 22.30 for the bottom panel). Specifically, we plot Tskin–0.2m(t) − Tskin–0.2m(adjusted-time). Black + shows the results using λ=6, *A*=0.23; grey ◊ is using λ=4.1, *A*=0.15. For comparison pale grey x shows the same difference but for warm layer rather than the cool skin, i.e. $T_{sub-skin–0.2m}(t) − T_{sub-skin–0.2m}$(adjusted-time). Dotted lines are ±6h from the adjusted time (i.e. 10.30 or 22.30).

This document is to be used with the ESA SST_cci Version 1 (v1) products.

CCI Phase 1 (SST)   *SST_CCI-ATBDV2-UOE-001*
SST CCI Algorithm Theoretical Basis Document v2   *Issue 1*

To choose between the alternative parameters in SST CCI processing, the skin minus sub-skin difference between the day and nighttime model results were compared with the equivalent AATSR minus drifting buoy differences between 2003 and 2010 (Figure 5.2). The cases were separated into three groups, depending on the number of clear pixels in the 9x9 box centred on each matchup location. The cases with fewer clear pixels (2-40) are more likely to be cloud contaminated. The upper panel shows the performance of the previously suggested coefficients ($A = 6$, $\lambda = 0.23$) and the lower panel the new coefficients ($A = 4.1$, $\lambda = 0.15$). For the two groups with the largest number of clear pixels, the existing coefficients give the best performance with a very close match between the model results and drifting buoy observations. The pale grey diamonds show the sub-skin minus bulk SST differences which are comparatively small. This is taken to justify our use of Fairall's original parameters ($A = 6$, $\lambda = 0.23$) rather than the alternative.
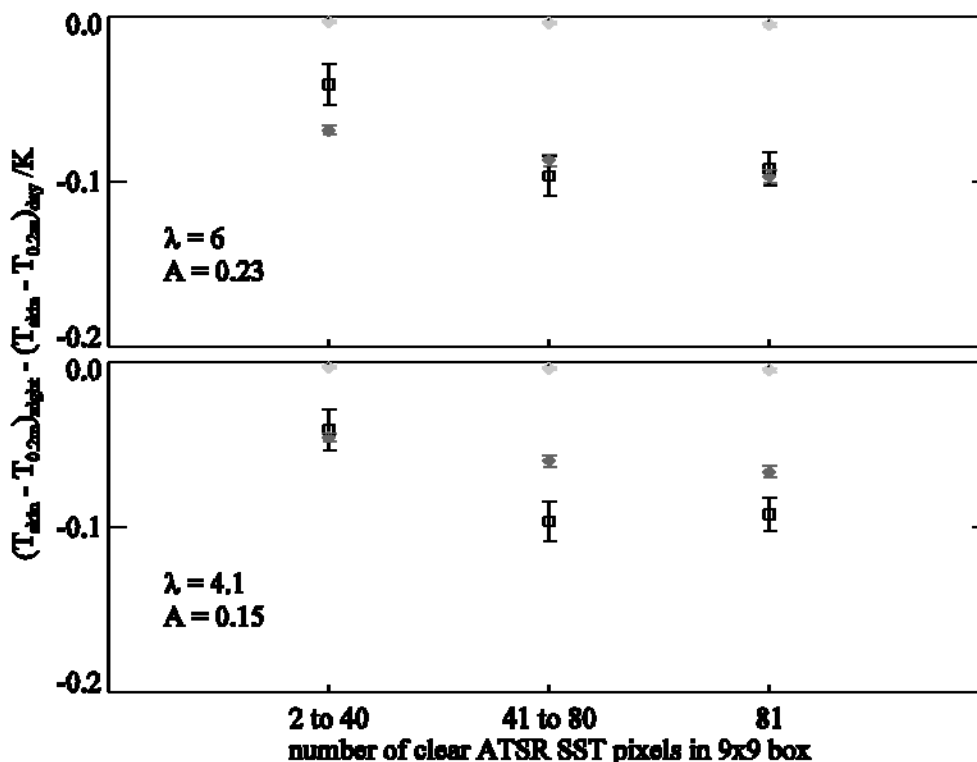

Figure 5.2. Mean of Tskin–0.2m(night) − Tskin–0.2m(day), night defined as 22:00–24:00, day as 08:00–12:00. Black □, AATSR skin – drifter buoy 0.2 m; grey ◊, Fairall-Kantha-Clayson model, pale grey ◊, Tsub-skin–0.2m(night)−Tsub-skin–0.2m(day). Upper panel, λ=6, A=0.23; lower panel, λ=4.1, A=0.15. Error bars are 1 standard error. Data period is 2003–2010.

5.3   Forcing Data for the Skin to Sub-Skin Model

The NWP data used is ERA-Interim, which has a resolution of 0.75° latitude and longitude. The model implementation follows that of the UK Met Office [RD.262] and is designed to use 6-hourly fields, using 3-hourly forecast fields coincident with the 6-hourly analysis fields. Table 5.1 lists the fields used to force the skin-to-sub-skin SST model.

This document is to be used with the ESA SST_cci Version 1 (v1) products.

CCI Phase 1 (SST)
SST CCI Algorithm Theoretical Basis Document v2

SST_CCI-ATBDV2-UOE-001
Issue 1

Table 5.1. NWP inputs to the Fairall-Kantha-Clayson model. ERA-Interim codes are provided in brackets, acronyms 'an' and 'fc' refer to analysis and forecast fields respectively.

ERA-Interim Field and Code	Fairall Kantha-Clayson Field
SST (34, an)	SST (Fairall, and to initialise KC)
10m E wind (165, an)	10m wind speed (to initialise KC)
10m N wind (166, an)	10m wind speed (to initialise KC)
Sensible heat flux (146, fc)	Non-solar heat flux
Latent heat flux (147, fc)	Non-solar heat flux and latent heat flux
Net surface thermal radiation (177, fc)	Non-solar heat flux
Net surface solar radiation (176, fc)	Solar heat flux
E turbulent stress (180, fc)	Wind mixing energy (friction velocity)
N turbulent stress (181, fc)	Wind mixing energy (friction velocity)

5.4 Uncertainty estimate

It is necessary to estimate the uncertainty in the skin model when forced by the ERA-interim NWP. The data used above (fig. 5.2) consist of a double difference between day and night, skin minus sub-skin SSTs; in each case, this double difference removes the satellite SST minus buoy bias (which is the same for the day and night). The uncertainty estimate therefore includes variance in both the satellite and buoy measurements and variance in the cool skin temperature. The random uncertainty in the buoy measurements is estimated as 0.04 K [RD.266]. For group three, defined in section 5.2, where all 81 pixels in the matchup were classified as clear–sky, the model minus observation variance is defined below [RD.266]. The time window was reduced to ±1 h to reduce the variation due to changes in the slope of the mean difference.

$$\sigma^2_{\text{model-obs,day-night}} \approx 0.045 \ K^2 \qquad (5.5)$$

The estimated variance due to instrument and buoy noise and is

$$\sigma^2_{\text{AATSR+buoy,day-night}} \approx 0.014 \ K^2 \qquad (5.6)$$

implying a total uncertainty of

$$\sigma^2_{\text{skin-0.2m,day-night}} \approx 0.031 \ K^2 \qquad (5.7)$$

which is approximately 4 times larger than the model variance [RD.266].

5.4.1 Model for Residual Bias and Uncertainty

The skin minus sub-skin SST differences between day and nighttime observations in Figure 5.2 indicate that the residual bias can be assumed to be zero. The residual variance (σ^2) within ±6 h of the adjustment time can be approximated using a linear fit

$$\sigma^2 = b \ [t - t_0] \qquad (5.8)$$

where

This document is to be used with the ESA SST_cci Version 1 (v1) products.

CCI Phase 1 (SST)   *SST_CCI-ATBDV2-UOE-001*
SST CCI Algorithm Theoretical Basis Document v2   *Issue 1*

t   observation time

t_0 adjustment time

b   constant

b is defined with respect to the adjustment and observation times:

b = 0.0040 for: t_0 = 10:30,   04:30 < t < 10:30

b = 0.0012 for: t_0 = 10:30,   10:30 < t < 16:30

b = 0.0012 for: t_0 = 22:30,   16:30 < t < 22:30

b = 0.0009 for: t_0 = 22:30,   22:30 < t < 04:30

5.4.2 Temporal and spatial correlations

The temporal and spatial correlation of the skin SSTs will be dependent on the meteorological situation. The cool skin is an instantaneous effect of solar insolation and wind speed, independent of their history, and therefore the correlation scales are likely to be smaller than those for the sub-skin layer (section 6.4.1). The correlation time is in the region of 6 hours with a correlation distance compatible with the NWP grid resolution of 0.75° [RD.266].

This document is to be used with the ESA SST_cci Version 1 (v1) products.

CCI Phase 1 (SST)   SST_CCI-ATBDV2-UOE-001
SST CCI Algorithm Theoretical Basis Document v2   Issue 1

6. MODEL OF SUBSKIN-DEPTH DIFFERENCE AND TIME-ADJUSTMENT DIFFERENCE

6.1 Background

As described in Section 5.1, to derive bulk SST from satellite observations of skin SST two corrections have to be applied: first an adjustment from the cool skin to the warmer sub-skin layer and second an adjustment from the sub-skin layer to the bulk SST. This second step requires an estimation of the stratification of the near-surface ocean between the sub-skin and the target depth, as the sub-skin layer exhibits a depth dependent diurnal cycle in SST. The CCI project generates SST retrievals from a number of satellite instruments, making observations at different local times. In order to compare these observations with one another and with historical in-situ observations of SST a time adjustment is also applied. Both depth and time adjustments will be described in this section.

6.2 The Model

6.2.1 Model Choice

The Kantha-Clayson model is used to make the sub-skin to bulk SST correction. This is coupled with the Fairall model for skin to sub-skin temperature conversion described in Section 5. The Kantha-Clayson model describes turbulence in geophysical boundary layers on the basis of second order closure models. It includes shear instability mixing in the stratified ocean, below the sub-skin layer, and diffusive heat transfer [RD.263, RD.262]. As with the Fairall model, it uses NWP data to describe local ocean-atmosphere conditions.

6.2.2 Model Setup for Sub-Skin to Bulk SST Adjustment

The Kantha-Clayson warm layer model is implemented using code provided by the UK Met Office. The model vertical resolution decreases with depth: from two centimetres at the surface to sixty centimetres at a depth of ten metres, and is run at a temporal resolution of ten minutes. In the UK Met Office implementation, the evolution of temperature (T) over time (t) for a single layer is defined as

$$\frac{T}{t} = \frac{1}{z}\ \frac{v}{\sigma_p} + K_H\ \frac{T}{z} + \frac{Q}{\rho C_p} \tag{6.1}$$

where

z   layer depth

v   molecular viscosity

σ_p molecular Prandtl number

K_H turbulent diffusion

Q   heat source

ρ   layer density

C_p specific heat capacity of seawater

The molecular mixing terms defined in the model (K_{HB} and K_{MB}) were modified to represent the diurnal thermocline rather than the entire oceanic mixed layer [RD.262]. Background salinity is set at 35 PSU and modified by evaporation although no precipitation is included in the model [RD.262, RD.266]. ERA-Interim NWP fields are used as input at a 6 hourly temporal resolution. At each time step, the sub-skin to bulk temperature differences are output for depths of 0.2, 1.0 and 1.5 metres.

6.2.3 Model Setup for Time Adjustment

As the Kantha-Clayson model needs a few hours to stabilise, it is initialised from a start time 17 hours earlier than the first dawn prior to the reference time: 12 hours for the adjustment period and a further 5 hours for the model initialisation. This gives a maximum lead time of 24 plus 17 hours prior to the SST adjustment time as the model has to be initialised just before dawn.   The first stage of the implementation is to produce the fields in the second column of Table 5.1 at a six hour temporal resolution.

The input fluxes are then interpolated to the model temporal resolution of ten minutes. Non-solar fluxes and fields are interpolated using Lanczos re-sampling, over a period of 12 hours (i.e. two 6-hour NWP model time-steps). The UK Met Office method [RD.264] is used to interpolate the solar flux. The equivalent peak insolation is calculated from the six hourly fluxes, linearly interpolated in time, and used to derive the solar flux.

6.2.4 Model Parameter values

The parameters recommended for the Kantha-Clayson model set-up are described in detail in RD.266.

6.3 Model Performance and Criteria for Time Adjustment

Model performance is assessed using data from the Multi-Matchup Database (MMD) [RD.266]. For each matchup a time series of buoy measurements is available. Assuming two or more measurements, a dataset of temperature differences between the reference and adjustment times is constructed, using each measurement in turn as the reference time. Similarly, the same set of differences is calculated from the model time series and using the model minus measurement differences. The results are binned into ten minute time steps corresponding with the model output. For each matchup the time range for inclusion of satellite observations or in-situ measurements is ±12 h around the reference time.

The mean diurnal cycle of temperature differences are shown in Figure 6.1, compared against buoy data. The model follows the measured diurnal cycle very closely with a lead of approximately 1.5 h, giving a residual difference of about 1/5 of the observed diurnal cycle. The phase shift may be due to errors with the NWP fields of their interpolation; it is not clear what physical effect would give a phase lead in the Kantha-Clayson model [RD.266].
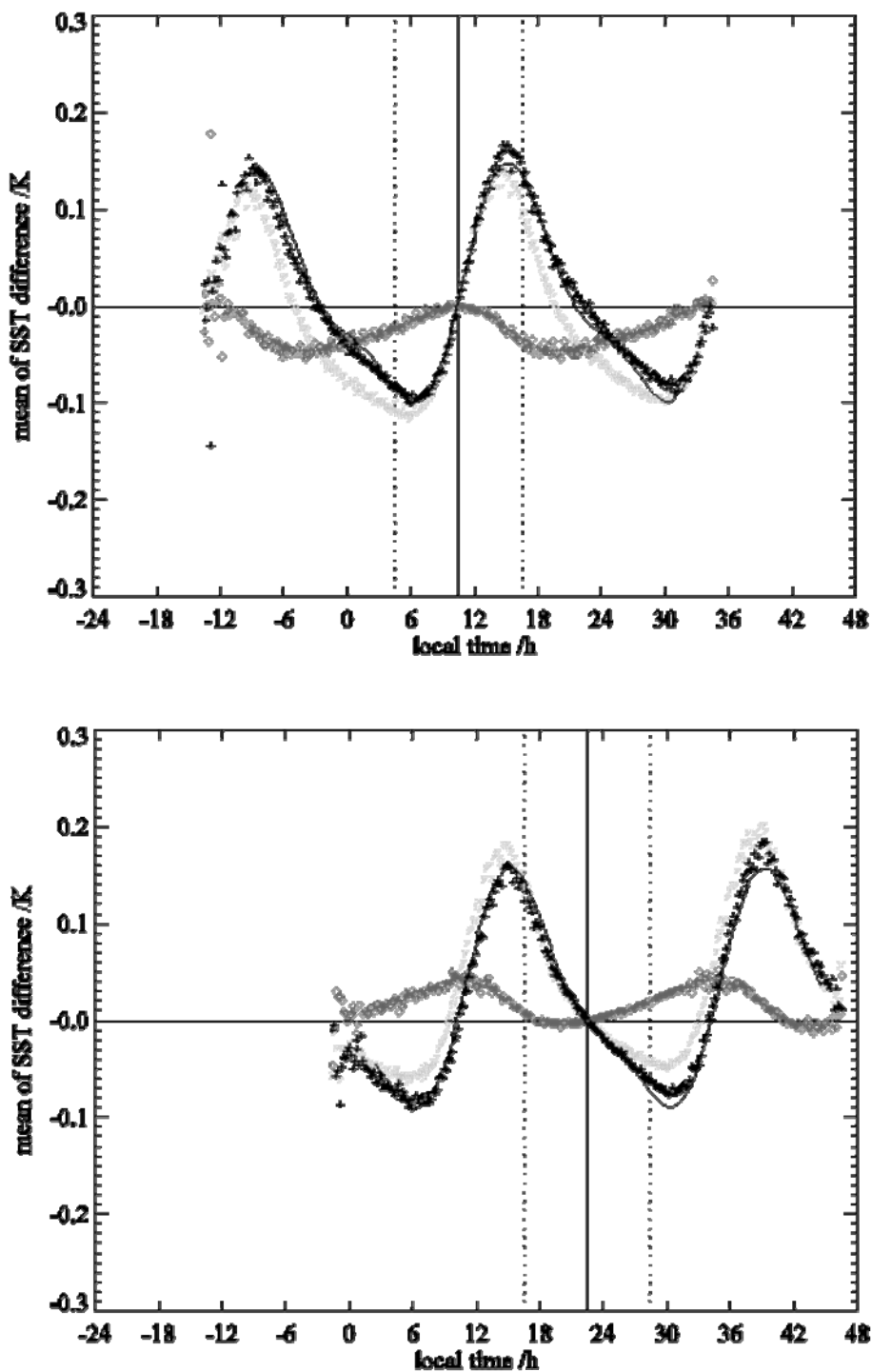
Figure 6.1. Plots show the mean change in SST difference away from the adjusted times (10.30 for the top panel, 22.30 for the bottom panel). Specifically, we plot T0.2m(reference time) − T0.2m(adjustment-time). Black +, drifting buoy measurements; pale grey x, Kantha-Clayson model; grey ◊, model−buoy. The lines through the points show the fit to diurnal and semi-diurnal harmonics (section 6.4). Dotted lines are ±6h from the adjustment time.

This document is to be used with the ESA SST_cci Version 1 (v1) products.

CCI Phase 1 (SST)   *SST_CCI-ATBDV2-UOE-001*
SST CCI Algorithm Theoretical Basis Document v2   *Issue 1*

Satellite observations are adjusted to the standard observation times of 10.30 and 22.30 when the sub-skin temperature is closest to the mean daily temperature. The ATSR instruments most closely match these observation times and currently provide the most accurate SST retrievals. Figure 6.2 shows the variance between the time-adjusted SST and reference SST for buoy and model measurements at both 10.30 and 22.30, using data from the MMD. One option for choosing the reference time against which to adjust the observation is to pick the condition under which the variances are approximately equal. Figure 6.2 shows that this would result in more observations being corrected to 22.30 than 10.30. The observations are therefore adjusted by choosing the closest reference time. This has the advantage over assigning 'day' and 'night' conditions of achieving a maximum time difference between the observation and reference time of six hours.
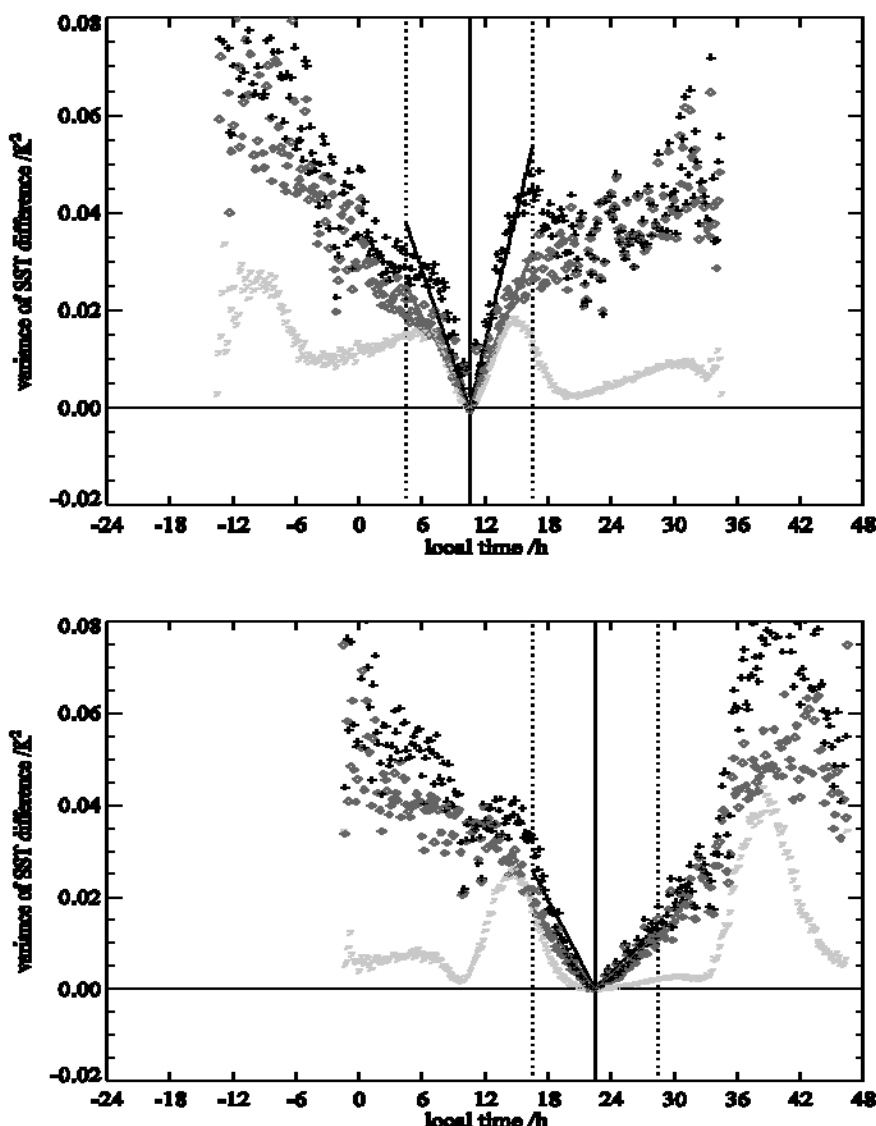
Figure 6.2. Variance of $T_{0.2m}$(reference time) − $T_{0.2m}$(adjusted-time). Black +, drifting buoy measurements; pale grey x, Kantha-Clayson model; grey ◊, model−buoy. The lines through the points are linear fits constrained to zero at 10.30 (top panel) and 22:30 (bottom panel). Dotted lines are ±6h from 10.30 and 22:30. Buoy and model−buoy have the estimated combined buoy random noise and discretisation error (variance=0.04^2) subtracted. The curves for the measurements and the difference have been reduced by the estimated variance for the buoy temperature differences of 0.0016 K^2.

6.4 Quantification of Uncertainty

The residual bias shown in Figure 6.1**Error! Reference source not found.** can be fitted to a combination of diurnal and semi-diurnal harmonics:

$$e = a_0(t_0) + a_1 \cos\left(\frac{2\pi(t-\varphi_1)}{24}\right) + a_2 \cos\left(\frac{2\pi(t-\varphi_2)}{24}\right) \tag{6.2}$$

where

$a_1 = 0.022$

$a_2 = 0.0043$

$\varphi_1 = 9.5$

$\varphi_2 = 11.6$

$a_0(10.30) = -0.025$

$a_0(22.30) = 0.017$

These functions are plotted in Figure 6.1 and the fit is excellent within ±6 h of the reference times. The residual variance can be approximated within ±6 h of the reference time by a linear fit:

$$\sigma^2 = b\,[t - t_0] \tag{6.3}$$

where

t   observation time

t_0 adjustment time

b   constant

b is defined with respect to the adjustment and observation times:

b = 0.0042 for: t_0 = 10:30,   04:30 < t < 10:30

b = 0.0054 for: t_0 = 10:30,   10:30 < t < 16:30

b = 0.0030 for: t_0 = 22:30,   16:30 < t < 22:30

b = 0.0020 for: t_0 = 22:30,   22:30 < t < 04:30

6.4.1 Temporal and spatial correlations

The temporal and spatial correlation of time and depth adjusted SSTs are dependent on the meteorological situation. At small scales, correlation times can be less than an hour [RD.222] and correlation distances can be less than 25 km [RD.265].

An estimate of the correlation time for the residual error can be made from the variance curves (Figure 6.2). The errors appear to be correlated to about 6 h for the 10:30 adjustments and 8 h for 22:30 adjustments. Variance curves calculated for other reference times have a similar shape and scale with a correlation time near 6 h.

The in-situ information in a matchup is at a single point, so there is no information from which to estimate the spatial correlation. This is assumed to be similar to NWP grid scale at 0.75°.

7. IMPROVEMENTS IN SEA SURFACE TEMPERATURE ANALYSIS IN OSTIA (LEVEL 4 SSTS DEVELOPMENTS)

The Operational Sea Surface Temperature and Sea Ice Analysis (OSTIA) system was developed at the UKMO where it is run in near-real time (NRT) daily [RD.213].   OSTIA uses satellite and in-situ SST data, together with sea ice concentration data, to produce a global gridded SST and sea ice analysis on a 0.05° grid with no data gaps (known as a 'Level 4' data product).   An OSTIA reanalysis system has been developed largely based on the near real time (NRT) system and has been used to produce a SST reanalysis for the period 1985 to 2007 (OSTIA reanalysis v1.0) [RD.239].   This reanalysis system is used in the first phase of the CCI SST project to produce the Level 4 product using satellite data only [RD.175].   The analysis process in OSTIA is not described in detail here; instead the reader is referred to recent OSTIA publications [RD.213, RD.239].

This section details and justifies the improvements made to the SST analysis in the OSTIA reanalysis system for the CCI SST project.   OSTIA uses a background error covariance matrix to determine how observation increments are spread on to the background field. Previously, these error estimates were calculated from model results as described in [RD.213].   Development work has been carried out to improve the parameterisation of this covariance matrix by estimating the background error covariance parameters using observation-minus-background differences from the Along Track Scanning Radiometer (ATSR) and drifter data obtained from the OSTIA reanalysis v1.0. This development work is described here together with results from experiments used to assess the impact on the accuracy of the SST analysis.

7.1 Background

The OSTIA system assimilates SST observations onto a background field based on persistence of the previous day's SST analysis with a slight relaxation to climatology. The weight and degree to which an observation is spread in this assimilation is dependent on both the observation error covariance matrix and the background error covariance matrix in the Optimal Interpolation (O.I.) equation [RD.213]. Within the OSTIA SST assimilation, the observation errors are assumed to be spatially uncorrelated so the spatial spreading of an observation is wholly determined by the background error covariance matrix. See [RD.213] for a full description of the OSTIA SST assimilation scheme.

The background error covariance matrix is too large to specify explicitly. It is parameterised into a diagonal matrix of background error variances with the off-diagonal elements specified using a second-order auto-regressive (SOAR) function which spatially correlates the background errors. The background error variance and background error correlation length scale parameters are estimated using the Hollingsworth and Lonnberg technique [RD.278].

A more realistic representation of the background errors than those obtained from model results is achieved by using observation minus background differences from ATSR and drifter data. These are decomposed into small scale errors associated with mesoscale ocean variability, hereafter referred to as mesoscale background errors, and larger scale background errors that occur over the scale of atmospheric synoptic systems, hereafter referred to as synoptic scale background errors [RD.280]. Each component of the background error will have an associated error variance and error correlation length scale, these will combine to give the total background error variance and an effective correlation length scale.

The Hollingsworth and Lonnberg method uses observation-minus-background (O-B) differences to estimate the background error covariance parameters. Observation-minus-

background differences from the OSTIA reanalysis v1.0 [RD.239] for drifting buoy and ATSR observations were used in the estimates presented here.

7.2 Description of method to derive covariance parameters

7.2.1 Theoretical Description

The Hollingsworth and Lonnberg technique [RD.278] estimates the background error covariances from the spatial covariances in the observation-minus-background (O-B) differences. The method assumes that observation errors are spatially uncorrelated so correlations in the O-B differences can be attributed to correlations in the background errors. The background error variance within a grid box is estimated by extrapolating the O-B covariances back to zero separation distance.

The Hollingsworth and Lonnberg technique requires the observations used in the estimation to be unbiased. To this end observations from the OSTIA reanalysis v1.0 from drifting buoy and the AATSR satellite, which have both been shown to be of high quality, were used in the calculations presented here. Another requirement for the technique to give meaningful results is that the spatial coverage of the observations is good. This is the case for the satellite observations and the drifter network is deemed sufficiently mature to provide global coverage by 2002.

7.2.2 Processing Outline

The background error covariance parameters are estimated using the Hollingsworth and Lonnberg technique. Output from the OSTIA reanalysis v1.0 [RD.213] was used in the estimates presented here.

O-B differences were calculated by bi-linearly interpolating the OSTIA reanalysis v1.0 background field to the observation location. To reduce the resources required in the estimation of the covariances, the AATSR observation-minus-background differences (which are at the 1km observational resolution) were super-obbed using a median method with a radius of 6km.

The covariance estimation described below is carried out on a 1° regular grid. The following steps are carried out:

- 19 bins of separation distance are defined (in km) as follows: [10, 15, 20, 50, 100, 150, 200, 250, 300, 350, 400, 450, 500, 600, 700, 800, 900, 1000].
- Within each grid square the covariance of each O-B difference with all other O-B differences within each of the predefined separation distance bins is calculated. These covariances are combined to give a covariance for observations in each grid square with all observations within each of the separation distances of it.
- For the anisotropic calculation (section 6.4) only observations within an angle of $\pi/2$ in the North or South direction are used in the calculation of the North-South (NS) covariances. Similarly for the East-West (EW) covariances.
- For each grid square the number of values, the mean and root mean square error of observations is output together with the covariances and number of observations contributing to the covariance for each of the separation bins. This is done for each day.
- Daily files are then combined into a single file which allows seasonal, monthly or annual covariances to be calculated as well as correlations for the whole run.
- These files then undergo a further level of processing (detailed below) which estimates the background error variances and the correlation length scales for each of the two components of the background error covariances for each of the 1° grid boxes.

The O-B covariances are regressed against separation distance for each of the 1° grid boxes and two Second Order Auto-Regressive (SOAR) function (equation 7.1) are combined to fit the data for each grid box. One SOAR function represents the error covariance due to mesoscale ocean features whilst the other represents the error covariances due to larger scale atmospheric synoptic conditions.

$$f(x) = V_m \left(1 + \frac{X}{L_m}\right) e^{\left(\frac{-X}{L_m}\right)} + V_s \left(1 + \frac{X}{L_s}\right) e^{\left(\frac{-X}{L_s}\right)} \qquad (7.1)$$

where V_m and V_s are the mesoscale and synoptic scale background error variances, L_m and L_s are the mesoscale and synoptic background error correlation length scales.

The fitting routine fits both the background error variances and the correlation length scales for both components of the background error. These are output to a file, along with the total background error variance (which is a combination of both the mesoscale and the synoptic scale components), the observation error variance and the chi-squared fit of the function to the data for each grid. See Figure 7.1 for an example of the fit for a specific grid box.
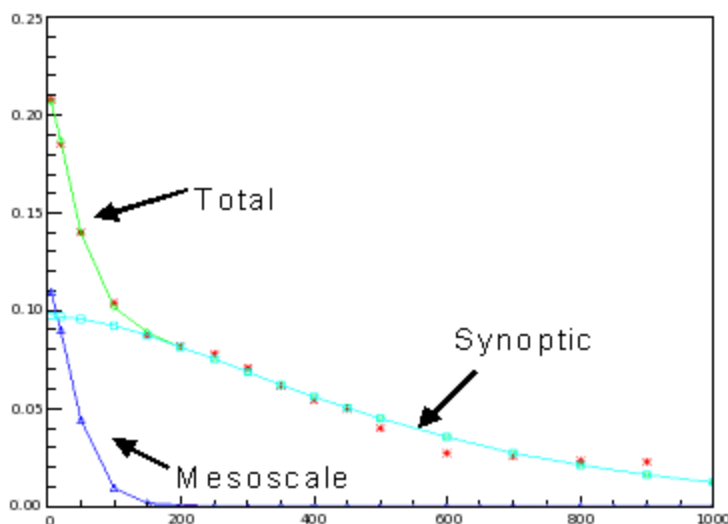

Figure 7.1. Example of the partitioning into mesoscale and synoptic scale error components of the SOAR function fitting code to the correlations regressed against separation distance. Adapted from RD.294.

7.3   Summary of analysis of O-B error estimates

The development of O-B error properties is described fully in RD.294, wherein error properties are separated into mesoscale and synoptic scale characterised by the variance of error estimate and the correlation length scale. In summary:

- Almost full global coverage of the O-B field is achieved using AATSR data, with good coverage at high latitudes in the marginal ice zone, and the resolution of the error variances is adequate to represent small ocean scale features.
- Ocean regions with high SST gradients have increased error variance compared to previous, less realistic estimates. Mesoscale and synoptic scale variance occurs in roughly the same places, although the magnitude of the synoptic component is reduced compared to the mesoscale component.
- Correlation length scales increase toward the equator; the mesoscale (synoptic) correlation length scales increase from around 20km (240km) at mid-latitudes toward 40km (350km) at the equator; see Figure 6.2 for an example of the mesoscale component.

This document is to be used with the ESA SST_cci Version 1 (v1) products.

CCI Phase 1 (SST)
SST CCI Algorithm Theoretical Basis Document v2

SST_CCI-ATBDV2-UOE-001
Issue 1

- Using a drifter observation-minus-background field as an additional check, it was shown in RD.294 that the spatial patterns of the mesoscale and synoptic variance are similar for estimates made using both observation types and that this makes it unlikely that correlations in the observation error are contaminating the AATSR synoptic background error estimate.
- The better observational coverage of the AATSR estimates mean that seasonal estimates of the covariance parameters can now be made. The improved spatial coverage at high latitudes mainly contributes in the Summer Hemisphere. The synoptic variances show a distinct seasonal cycle, although this could be a due to contamination of the diurnal warming signal during the summer.
- The EW and NS estimates of the background error variances were similar. Anisotropy was observed in the error correlation length scales but the patterns of zonal lengthening towards the equator were common to both the EW and NS estimates.

7.4   Implementation

The estimated background error covariance parameters described in section 7.2 were implemented in the OSTIA system to test the impact of the updates on the OSTIA SST analysis. Global spatial maps of seasonally varying mesoscale and synoptic scale background error variances estimated using the AATSR O-B data were implemented.

The global zonal averages of the correlation length scales were found to be relatively robust across different ocean basins. Anisotropic length scales are parameterised to be globally latitudinally varying using the following functional form,

$$L = L_c + Ae^{(-T^2)} \text{ (for } |Latitude| \leq 20° \text{)} \qquad (7.2)$$

$$T = \frac{\text{Latitude}}{S}$$

$$L = L_c \text{ (for } |Latitude| \geq 20° \text{)}$$

Where *L* is the final length scale (used for L_c and L_s in equation 7.1), L_c is constant length scale, *A* and *S* are amplitude and scale parameters respectively.

Table 7.1. Parameter values for the latitudinally varying correlation length scales.

Scale	Direction	L_c	A	S
Mesoscale	EW	15 km	20 km	10
Mesoscale	NS	20 km	20 km	10
Synoptic scale	EW	200 km	100 km	10
Synoptic scale	NS	250 km	200 km	10

Parameter values differ between the E-W and N-S length scales as well as between the mesoscale and synoptic length scale. The parameter values used are shown in Table 7.1. The mesoscale parameterisations are shown as the red lines in Figure 7.2.
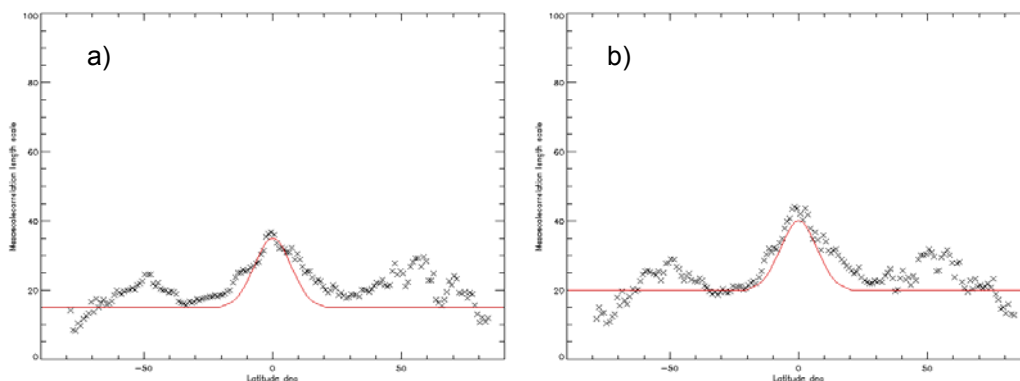
Figure 7.2. Zonal averages of the mesoscale correlation length scales (km) in the (a) East-West and (b) North-South direction estimated from the AATSR O-B output.

7.4.1 Impact of increased Iterations & variable error parameters

Experiments were conducted to test the impact of using the newly calculated background error parameters on the accuracy of the SST analysis in the OSTIA system. These experiments also investigated the impact of increasing the number of analysis iterations from 10 to 100 together with the new background errors. This follows on from recent experiments for a different project, which showed that increasing the number of assimilation iterations resulted in improvements in the feature resolution of the analysis without introducing observational noise through overfitting the data. The results from these experiments were compared to those from the previous OSTIA reanalysis system which used background error variances estimated from a model, static length scales of 10 km (100 km) for the mesoscale (synoptic) components and 10 analysis iterations. RD.294 fully describes these experiments and the individual effects of increasing the analysis iterations to 100 and allowing the error parameters to vary.

The accuracy of the OSTIA SST analysis is normally assessed using the O-B differences to drifting buoy data; which with the new parameters and 100 assimilation iterations reduced from 0.52K to 0.37K. Thus the updates to the background error covariances are within the GCOS breakthrough target for analysis accuracy of 0.4K [RD.285]. The breakthrough target is the accuracy level, if achieved, that would result in a significant improvement for climate applications. Statistics of the new system relative to ARGO and AATSR are shown in RD.294.

The impact of the updates on the ability of the SST analysis to resolve small scale ocean features was studied using the SST gradients. Figure 7.3 (adapted from RD.294) shows the impact on the gradient fields in the Gulf Stream region for 31st March 2012, a representative day of a month long trial; it is clear that using the updates along with 100 iterations increases the magnitude of the SST gradients. Analysis of animations shows it is more temporally consistent with realistic ocean features and that the updates do not create any obvious temporal observational noise in the fields.
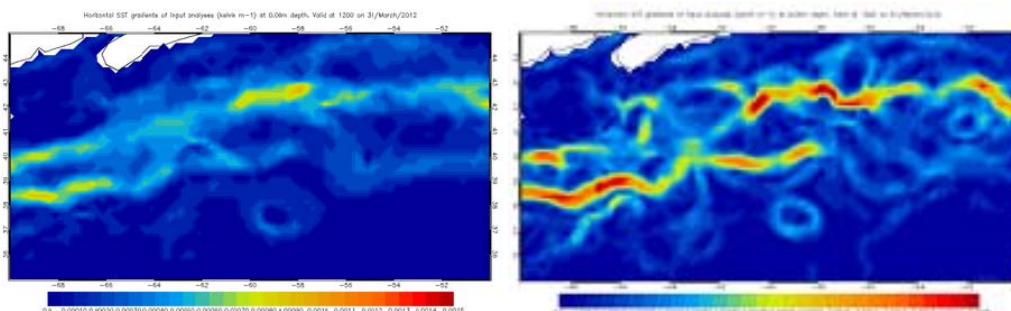
Figure 7.3. SST gradients in the Gulf Stream (10*K/m) for (left) a simulation using 10 iterations and 'old' variances, and (right) a simulation using 100 iterations and 'new' variances and length scales. Scale ranges from 0 to 0.0015. Adapted from RD.294.

7.5 Assumptions and limitations

7.5.1 Performance of method of deriving covariances

The Hollingsworth and Lonnberg estimation technique employed here makes a number of assumptions on the error characteristics of the input data. An assumption is made that the observation and the background field used in the calculations are independent. In this work, the OSTIA reanalysis v1.0 was used, which had an assimilation window of 72 hours, so observations used in the O-B differences are those within ± 36 hours of 1200 UTC on the analysis day. Therefore, the OSTIA background field and the observations used in the O-B calculation are not independent; furthermore the O-B field on any given day will not be independent of those on previous or subsequent days. However, during the validation of the OSTIA analysis v1.0, the lack of independence between the observations and the background field was deemed to have minimal impact on the validity of the validation results, see [RD.239] for this discussion.

It is also assumed that the observations used in the parameter estimation technique are unbiased and are not spatially correlated. The drifter and AATSR observations used here have been shown to be unbiased, [RD.239]. It might still be expected though that observational errors may contain spatial correlations. For the AATSR observations a major component of the observation error may be due to errors in the atmospheric correction of the satellite retrieval which would be on the scales of atmospheric synoptic systems. Smaller scale correlations in the observational errors may also exist due to correlations along the satellite swath. The drifting buoy observation correlations would be expected between different observations from the same platform over the course of the assimilation window. It is expected that these spatial correlations for the different observation types occur at different spatial scales. RD.294 showed that estimates calculated using both observation types were similar and thus validate each other. Without knowing the spatial correlations in the observations explicitly, using different observations gives us greater confidence that the impact of violating this assumption is minimal.

The validity of partitioning the background error into those associated with mesoscale and synoptic scale variability was considered in RD.294. However the impact of the updates presented here on the SST assimilation will be through the total background error variances and the effective correlation length scale, i.e. the combination of the two components. This means that the possibility of erroneous assignment of O-B variability to

This document is to be used with the ESA SST_cci Version 1 (v1) products.

CCI Phase 1 (SST)   *SST_CCI-ATBDV2-UOE-001*
SST CCI Algorithm Theoretical Basis Document v2   *Issue 1*

one or the other of the components through the function fitting will have minimal impact on the assimilation.

7.6   Conclusions

The new background error covariance parameters were derived using the Hollingsworth and Lonnberg method on O-B output from the OSTIA reanalysis v1.0. Parameters were estimated from the AATSR O-B differences for both the mesoscale and synoptic scale background error variances and background error correlation length scales. Seasonal calculations of the covariance parameters were made and seasonal variability was found in the spatial patterns of both components of the error variance.

The correlation length scales showed less seasonal variability but the length scales were found to be latitudinally variable with an increase in the length scale at the equator and at mid-latitudes in both mesoscale and synoptic scale components. Anisotropy was also found in the correlation length scales with different scales found in the East-West and the North-South directions.

The accuracy of the OSTIA SST analysis was validated using both assimilated drifting buoy and AATSR O-B differences globally and in ocean regions. The global RMSE was 0.37 K for the drifter O-B stats and for the AATSR O-B stats. Using independent ARGO data to validate the analysis the global standard deviation error was 0.44 K. The accuracy of the OSTIA SST analysis is normally assessed using the O-B differences to drifting buoy data; taking this value as 0.37 K, the updates to the background error covariances are within the GCOS breakthrough target for analysis accuracy of 0.4 K [RD.285]. The breakthrough target is the accuracy level, if achieved, that would result in a significant improvement for climate applications. Note that the independent ARGO comparisons are also close to the breakthrough accuracy level.

8. IMPROVEMENTS IN PRE-PROCESSING SEA ICE DATA IN OSTIA (LEVEL 4 DEVELOPMENTS)

8.1 Introduction

The OSI-SAF global sea ice concentration reprocessing dataset [RD.43] will be used for the OSTIA CCI reanalysis. However, there are a number of data gaps, ranging in length from one day to several weeks, resulting from either lack of available data, missing data within the ice field or rejection of an unrealistic looking ice field through our own quality control. For the previous version of the OSTIA reanalysis (v1.0), ice concentration from the previous available day was persisted in the event of a data gap. For gaps of 7 days or longer, the ice concentration file at the end of the data gap was copied to the centre and persisted to the end of the gap [RD.275]. The aim of this work is to improve upon this persistence method, using a simple linear interpolation method based on data assimilation theory to fill the sea ice timeseries gaps.

8.2 Method

For each location on the ice concentration grid, we require an ice concentration estimate for each day of the gap. This estimated ice concentration is weighted by the error estimates of the data at either end of the gap, as well as its relative temporal position in the gap. This is achieved using the following method.

A linear model is used for the interpolation of data into the time gap, of the form y = mt + c, where y are the observations of ice concentration at a particular grid point at different times t, in days. The linear model for the interpolation (y = mt + c) is put into matrices to give the model value at observation times.

Using dataassimilation theory, e.g. [RD.276], a cost function J can be derived:

$$J = (y - Hx)^T R^{-1} (y - Hx) \tag{8.1}$$

Minimising equation (8.1) with respect to x, and rearranging for x gives

$$x = (H^T R^{-1} H)^{-1} H^T R^{-1} y \tag{8.2}$$

where

$$H = \begin{bmatrix} t_1 & 1 \\ t_n & 1 \end{bmatrix}, \ x = \begin{bmatrix} m \\ c \end{bmatrix}, \ y = \begin{bmatrix} y(t_1) \\ y(t_n) \end{bmatrix}, \ R = \begin{bmatrix} V_1 & 0 \\ 0 & V_n \end{bmatrix}$$

t_1 is day 1, the day available at the start of the gap, and t_n is the day at the end of the gap of length n days. x are the parameters in the linear model which determine the best estimate of ice concentration. R is the observation error, where $V_{1,n}$ is the variance of the observation errors at $t_{1,n}$ (provided with the data).

Then we can use $x(0) = m$ and $x(1) = c$ in the model equation for any t_n in the gap, to find the ice concentration (y) at this point. It is assumed errors at the start and end of the period are uncorrelated.

8.3   Results

Tests were run using OSI-SAF sea ice reprocessing data [RD.43] between 26 May 2002 and 31 May 2002, for both the Northern and Southern Hemispheres. These dates were chosen at random. The method described above was used to generate ice concentration fields for four days where complete fields were already available, for comparison.

Figure 8.1 shows the difference between a sample interpolated field and the actual field for both hemispheres. The low ice concentration data outside of the ice edge seen on figure 8.1 are erroneous and are filtered out in the OSTIA reanalysis according to guidance in the OSI-SAF user manual [RD.43]. The differences between the real and interpolated fields are largest around the ice edge (figure 8.1), which is the region where the largest day-to-day (and potentially non-linear) changes would be expected, and is hence the most difficult to capture using a linear interpolation method. Figure 8.1 illustrates that the differences are spatially variable, but the overall mean differences are small, as shown in table 8.1
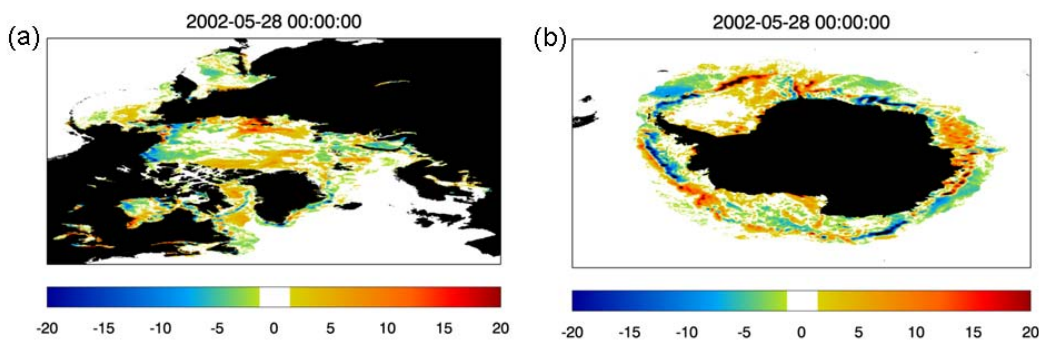

Figure 8.1. Interpolated minus real ice concentration field (%) on 28 May 2002, for (a) Northern Hemisphere and (b) Southern Hemisphere.

This table gives the differences between both the interpolation and persistence methods and the observed (real) ice concentration. We would expect to see some differences between the real and interpolated fields since in reality the ice concentration does not change according to the linear model used and the rate of change is probably dependent on the time of year. However, these differences are smaller than were found for the persistence method (table 8.1), demonstrating that even using a changing ice concentration field based on a linear approximation is an improvement over persisting the ice concentration field from the start of the data gap. Note that the errors of the persisted compared to the real ice concentration field continue to grow with time, whereas the magnitude of the errors remains relatively similar for the interpolation method (table 8.1). There is a slight peak in the error magnitude in the centre of the interpolation period, which would become larger for a longer data gap.

This document is to be used with the ESA SST_cci Version 1 (v1) products.

CCI Phase 1 (SST)
SST CCI Algorithm Theoretical Basis Document v2

SST_CCI-ATBDV2-UOE-001
Issue 1

	Northern Hemisphere RMSE (mean error) of absolute concentration differences, %		Southern Hemisphere RMSE (mean error) of absolute concentration differences, %	
Date	Interp – real	Persist – real	Interp – real	Persist – real
20020527	3.81 (2.22)	4.16 (2.39)	3.97 (2.50)	4.65 (2.80)
20020528	4.53 (2.76)	5.58 (3.32)	5.61 (3.46)	7.55 (4.34)
20020529	4.52 (2.71)	6.44 (3.83)	5.21 (3.27)	9.07 (5.11)
20020530	4.03 (2.20)	7.37 (4.37)	3.44 (2.20)	10.08 (5.48)

Table 8.1 : Ice concentration difference statistics (absolute differences). Persistence method uses file from 20020526. Statistics calculated using gridpoints where ice is present in either file.

Overall, the differences between the real and interpolated fields are small, and as they are of a similar magnitude to the day-to-day variation of the real ice concentration fields for this time period (not shown) the results show the test is successful.

8.4 Conclusions

The method works well and produces good results. It has been used to produce interpolated data for the gaps in the OSI-SAF ice concentration timeseries between 1991 and 2007, which will be used in the CCI reanalysis Level 4 product.

8.5 Assumptions and Limitations

Error information in the sea ice files is passed through to the final OSTIA output files (see section 5.1). However, when the field is interpolated, the error information is set to missing data as no information is available. Status flags are assigned as a separate field to the error information and have been set as 100 for land, 12 for sea and 13 for interpolated ice concentration data, following the OSI-SAF convention for this dataset. For all the interpolated data within a gap, the overall ice extent (where there is any ice above 0%) does not change. This is because there is always ice above 0% where there is ice in either the start or end files. If the minimum is set to 15% for flagging as interpolated ice concentration data, the ice area does change in the files, but it has been set to 0% to keep the OSI-SAF convention.

This method works best for shorter gaps. The greater the difference between the ice fields at the start and end of the gap, the poorer the results.

8.6 Future Enhancements

A few incomplete fields are available which were removed as part of the initial quality control, since complete fields with no missing data are required. These could be used to add a spatial interpolation component to the method by using the partial data available in these fields to inform the interpolation.